ABSTRACT

Title of Dissertation: INVESTIGATION OF MAGNESIUM ION CHARGE STORAGE MECHANISM IN MANGANESE DIOXIDE

JaeHee Song, Doctor of Philosophy, 2016

Dissertation directed by: Professor Sang Bok Lee

Department of Chemistry and Biochemistry

Magnesium (Mg) battery is considered as a promising candidate for the next generation battery technology that could potentially replace the current lithium (Li)-ion batteries due to the following factors. Magnesium possesses a higher volumetric capacity than commercialized Li-ion battery anode materials. Additionally, the low cost and high abundance of Mg compared to Li makes Mg batteries even more attractive. Moreover, unlike metallic Li anodes which have a tendency to develop a dendritic structure on the surface upon the cycling of the battery, Mg metal is known to be free from such a hazardous phenomenon.

Due to these merits of Mg as an anode, the topic of rechargeable Mg batteries has attracted considerable attention among researchers in the last few decades. However, the aforementioned advantages of Mg batteries have not been fully utilized due to the serious kinetic limitation of Mg^{2+} diffusion process in many hosting compounds which is believed to be due to a strong electrostatic interaction between divalent Mg^{2+} ions and hosting matrix. This serious kinetic hindrance is directly related to the lack of cathode materials for Mg battery that provide comparable electrochemical performances to that of Li-based system.

Manganese oxide (MnO_2) is one of the most well studied electrode materials due to its excellent electrochemical properties, including high Li^+ ion capacity and relatively

high operating voltage (i.e., ~ 4 V *vs.* Li/Li^+ for $LiMn_2O_4$ and ~ 3.2 V *vs.* Mg/Mg^{2+}). However, unlike the good electrochemical properties of MnO_2 realized in Li-based systems, rather poor electrochemical performances have been reported in Mg based systems, particularly with low capacity and poor cycling performances. While the origin of the observed poor performances is believed to be due to the aforementioned strong ionic interaction between the Mg^{2+} ions and MnO_2 lattice resulting in a limited diffusion of Mg^{2+} ions in MnO_2, very little has been explored regarding the charge storage mechanism of MnO_2 with divalent Mg^{2+} ions.

This dissertation investigates the charge storage mechanism of MnO_2, focusing on the insertion behaviors of divalent Mg^{2+} ions and exploring the origins of the limited Mg^{2+} insertion behavior in MnO_2. It is found that the limited Mg^{2+} capacity in MnO_2 can be significantly improved by introducing water molecules in the Mg electrolyte system, where the water molecules effectively mitigated the kinetic hindrance of Mg^{2+} insertion process. The combination of nanostructured MnO_2 electrode and water effect provides a synergic effect demonstrating further enhanced Mg^{2+} insertion capability. Furthermore, it is demonstrated in this study that pre-cycling MnO_2 electrodes in water-containing electrolyte activates MnO_2 electrode, after which improved Mg^{2+} capacity is maintained in dry Mg electrolyte. Based on a series of XPS analysis, a conversion mechanism is proposed where magnesiated MnO_2 undergoes a conversion reaction to $Mg(OH)_2$ and MnO_x and $Mn(OH)_y$ species in the presence of water molecules. This conversion process is believed to be the driving force that generates the improved Mg^{2+} capacity in MnO_2 along with the water molecule's charge screening effect. Finally, it is discussed that upon a consecutive cycling of MnO_2 in the water-containing Mg electrolyte, structural water is generated within the MnO_2 lattice, which is thought to be the origin of the observed activation phenomenon. The results provided in this dissertation highlight that the divalency of Mg^{2+} ions result in very different electrochemical behaviors than those of the well-studied monovalent Li^+ ions towards MnO_2.

INVESTIGATION OF MAGNESIUM ION CHARGE STORAGE MECHANISM IN MANGANESE DIOXIDE

by

JaeHee Song

Dissertation submitted to the Faculty of the Graduate School of the
University of Maryland, College Park, in partial fulfillment
of the requirements for the degree of
Doctor of Philosophy
2016

Advisory Committee:

Professor Sang Bok Lee, Chair
Professor Neil Blough
Professor Yuhuang Wang
Professor Liangbing Hu
Professor Kyu Yong Choi

Dedication

To Sun and Jeremy

Acknowledgements

I express my gratitude to my advisor Dr. Sang Bok Lee, one of the best advisors one could possibly have. He has not only provided much advice in research and professional activities, but also consistently accommodated my personal circumstances. His support and encouragement has definitely kept me motivated to bring this dissertation to fruition. My sincere thanks also go to Dr. Malachi Noked for his guidance and encouragement during this research. I am honored to have worked with him, and I truly appreciate his deep insightfulness in science and humility.

I also thank the former and current Lee group members, who have not only inspired me in research but also made my life as a graduate student much enjoyable. I express my special thanks to my dear friend Nikki Schneck, who has made my PhD journey pleasant with her constant encouragement. I thank Dr. Gary Rubloff and his group for the stimulating discussions during joint group meetings, from which I was able to broaden my research to various aspects. I also acknowledge Dr. Karen Gaskell for her tremendous help in XPS analysis.

I thank my parents, Chaehun and Yeonhee, and my parents-in-law Byung and Moon for their unlimited support and prayers. I also thank my brother Jaewon, sisters-in-law, Eunjin and Eunice, brother-in-law Ji-Hoon for their support, and my nephew niece Jayden and Ella who have made me smile during trying times.

My deepest gratitude and love go to my beloved husband Sun and my son Jeremy − the two miracles happened in my life. Sun, you are the one who shaped me to be who I am now and none of this would have been possible without your endless love and support. Jeremy, every single day is filled with incredible joy since you came to this world.

Above all, I thank my God for the gentle guidance, patience and love through Christ he has shown me throughout my journey.

Table of Contents

List of Tables

List of Figures

Chapter 1 Introduction

Portions of this chapter have been published in Song et al., Mapping the Challenges of Magnesium Battery, J. Phys. Chem. Lett. ***2016****, 7, 1736.*

Portable consumer electronic devices make up a significant part of today's technologies and their rapid development would not have been possible without the utilization of lithium ion batteries (LIBs). Since the first commercialization of LIBs in the early 1990s,[2] they have been extensively employed in portable electronic devices and electric vehicles, due to their outperforming energy density, power, and cycle life. Nevertheless, the rapidly growing demand for increased capabilities in both portable electronic devices and electric vehicles requires a new generation of technology that can surpass the current LIB whose performance is foreseen as reaching the limit.

Magnesium (Mg) battery is considered as one of the promising candidates for the next generation of battery technology due to the following factors. Mg, when employed as an anode, possesses higher (by a factor of 5) volumetric capacity (3832 $mAhcm^{-3}$) than commercialized LIB anode materials (777 $mAhcm^{-3}$).[1, 3] Additionally, the low cost and high abundance of Mg compared to Li (300x more abundant than Li) makes Mg batteries even more attractive. Moreover, unlike metallic Li anodes which have a tendency to develop a dendritic structure on the surface upon the cycling of the battery, Mg metal is known to be free from such a hazardous phenomenon.[4, 5]

Due to these merits of Mg as an anode, the topic of rechargeable Mg batteries has attracted considerable attention among researchers in the last few decades.

However, the aforementioned advantages of Mg batteries become useful only when appropriate electrolytes and cathodes are identified and implemented. For example, when coupled with conventional electrolytes that are commonly used in LIB, Mg anodes quickly become electrochemically inactive due to the formation of passivation layer on the metal surface as a result of electrolyte reduction. In addition, the divalency of Mg ion results in very slow insertion kinetics in most potential cathode materials. This slow solid state diffusion of Mg^{2+} ions is the reason that very few cathode compounds have been realized for Mg battery systems.

In an effort to overcome the limitations which exist for the cathodes in Mg battery system, the goal of this dissertation is to investigate the charge storage mechanism of nanostructured manganese oxide focusing on insertion behaviors of Mg^{2+} ions. The following sections of this chapter discuss the background of general electrochemical energy storage systems, including important metrics that are necessary to understand the challenges and limitations of Mg batteries, followed by a discussion of the current state of the art in the research of Mg battery technologies, and an overview of the dissertation.

1.1 Basic Principles of Rechargeable Batteries

A rechargeable (or secondary) battery comprises three main components: an anode (or negative electrode), cathode (or positive electrode), and electrolyte that contains high concentrations of charge carrier ions. Figure 1.1a shows a schematic illustration of a LIB. During the discharge of a LIB, the Li^{+} ions transport through the electrolyte from the anode to cathode; therefore, during this process the cathode and

anode are reduced and oxidized, respectively, generating an electron flow around the external circuit and providing useful power for a device. During the charge process, the lithium ions are extracted from the cathode and move back to the anode upon the applied voltage from an external power source.

The discovery and research of rechargeable lithium-based cells trace back to lithium metal-based battery where metallic lithium serves as an anode. Lithium (Li), when employed as an anode, is particularly appealing since it is the most electropositive and lightest metal providing high energy density.[6, 7] However, despite these attractive features of Li metal as an anode, dendrite growth on the Li surface has led to serious safety concerns.[8] In light of the limitation of Li metal as an anode, the attention has been drawn to "Li-ion" batteries where metallic Li anode was replaced by carbonaceous materials, such as graphite.

Figure 1.1b shows a diagram for a Mg battery. The operating mechanism of a Mg battery is similar to that of an LIB except that the Mg^{2+} ions in Mg batteries go through "deposition/dissolution" process on the surface of Mg instead of "insertion/extraction" mechanism. Therefore, it is important to note the different use of terminology for "metal-ion" battery (e.g., Mg-ion battery) and "metal" battery (e.g., Mg battery) as the anode reduction/oxidation processes of these two battery systems operate in different ways.

The cell operating voltage is another important difference to acknowledge between Li-based battery and Mg battery systems. That is, the operating voltage of Mg batteries is limited compared to that of Li-based batteries since the redox

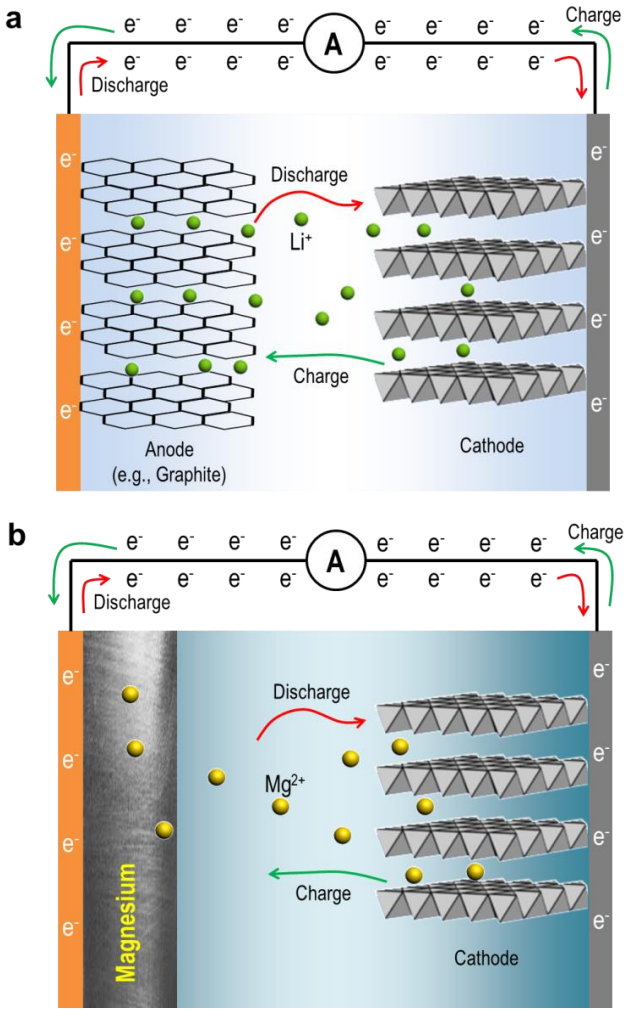

Figure 1.1 Schematic illustration of (a) Li-ion battery where graphite anode and layered type cathode are utilized, (b) Mg battery where metallic Mg anode and layered type cathode are utilzed.

potential of Mg^{2+}/Mg is less negative than Li^{+}/Li by 0.69 V (-2.36 V for Mg^{2+}/Mg and -3.05 V for Li^{+}/Li vs. SHE).[9, 10] This lower operating voltage generally results in lower overall energy density of Mg battery compared to the Li-based batteries. The relation of cell operating voltage and energy density is described in the following section.

1.2 Important Performance Metrics of Battery Systems

1.2.1 Cell Operating Voltage

Voltage (V_{cell}), or electrochemical potential difference between the anode and cathode of an electrochemical energy storage device, is the driving force that generates the movement of electrons from one electrode to the other. Thus, the higher the voltage the higher energy is achieved. The voltage measured between two electrodes is directly related to the corresponding difference in their Fermi energy level (μ) which is the work required to add/remove an electron to/from a body (Eqn. 1.1). Therefore, when two electrodes with different Fermi energy levels are connected in a circuit, the electrons flow from an electrode that possesses higher μ (reductant) to lower μ (oxidant).

$$V_{cell} = \left| \frac{\mu_A^i - \mu_C^i}{F} \right| \qquad \text{(Eqn. 1.1)}$$

Figure 1.2 shows a schematic diagram of the relative electron energies of a battery system where the direct relation between V_{cell} and Fermi energy levels of anode (μ_A) and cathode (μ_C) is illustrated.[11] When considering the operating voltage of a cell, the stability limit of the employed electrolyte also has to be taken into account. The stability of an electrolyte is determined by the energy separation (E_g) of the lowest unoccupied molecular orbital (*LUMO*) and highest occupied molecular orbital (*HOMO*) of the electrolyte, and this stability is often referred to as voltage window of an electrolyte. The voltage window of the electrolyte affects the overall cell operating voltage; if the Fermi energy of an anode (μ_A) lies above the *LUMO* energy level of the

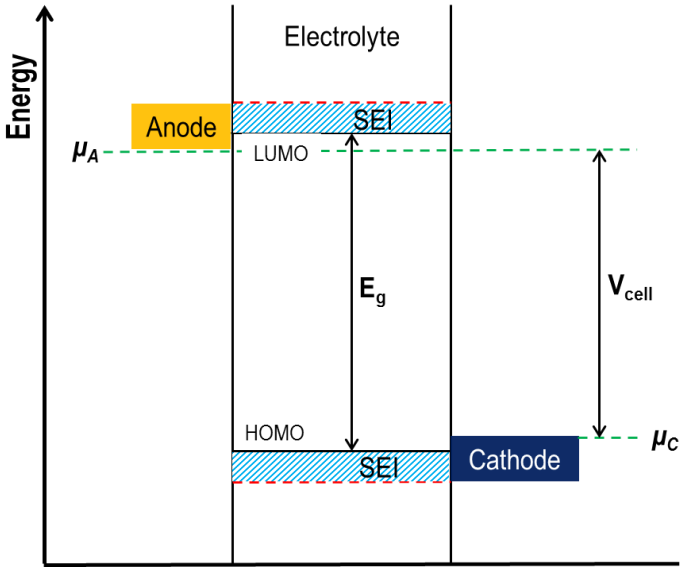

Figure 1.2 Schematic diagram of the relative electron energies of a battery system.

electrolyte, the electrolyte will be reduced at the anode surface. Similarly, if the Fermi energy of a cathode is below the *HOMO* level of an electrolyte, the electrolyte will be oxidized at the cathode surface. Therefore when selecting the electrodes and electrolyte for a battery system, the stable voltage window of an electrolyte should be greater than the difference in the Fermi levels between the anode and cathode as described in the following equation:

$$E_g \geq \mu_A - \mu_C = V_{cell} \qquad \text{(Eqn. 1.2)}$$

The reduction and oxidation of electrolyte species at the anode and cathode surface, respectively, result in the formation of a solid electrolyte interphase (SEI). Since the diffusion of ions is impeded within the SEI layer, its extensive formation is undesired in a battery system. However, in Li-based battery systems a thin layer of SEI layer is often known to be beneficial as further reduction of electrolyte species on the anode surface can be prevented by presence of SEI layer, while an efficient Li^+ ion

transportation is allowed.[12, 13]

1.2.2 Charge/Discharge Capacity

Theoretical specific capacity of an electrode material is defined as the maximum amount of electric charge (Q) that can be stored in the material, which can be calculated based on the Faraday's law as described in the following equation:

$$C_{spec,theoretical} = \frac{nF}{3600 \times M} \qquad \text{(Eqn. 1.3)}$$

where n represents the number of electrons transferred, F is the Faraday constant (96485 C/mol), and M is the molecular weight of the electrode. However, the theoretical specific capacity of an electrode is not always fully realized in a real battery system for several reasons. First, the kinetic limitation of ion transportation in the electrode, especially in the cathode, causes the charge carrier ions to not fully insert/ deinsert to/from the maximum capacity of the electrode.[14] Also, the full capacity cannot be achieved if the voltage, at which the full insertion/deinsertion of the carrier ions takes place, lies beyond the stability limit of the electrolyte.

There are two main techniques for measuring the practical capacity of an electrode: Galvanostatic voltammetry (GV) and cyclic voltammetry (CV). In GV, a controlled current is passed through between two electrodes and the resulting voltage is measured. Figure 1.3a shows a typical discharge GV curve of a battery electrode. Initially, the potential of the discharging electrode will drop rapidly (point A) as charges accumulate at the electrode/electrolyte interface until the electron transfer reaction of the electrode starts to occur. During the electron transfer reaction, the

voltage change is rather slow demonstrating a plateau or gentle slope (point B) which then quickly drops again after the electron transfer reaction is completed (point C). [15]

The practical specific capacity ($C_{spec,\ practical}$) can be determined based on the GV curve according to the following equation:

$$C_{spec,practical} = \frac{i \times t_{cutoff}}{3600 \times W} \ \ mAh / g \qquad \text{(Eqn. 1.4)}$$

where i is the applied current, t_{cutoff} is the time to reach the cut off potential that was set for the testing, and W is the weight of the active material.

On the other hand, in CV, the voltage is changed at a constant rate until it reaches the desired voltage and ramped back down in the opposite direction while the current is being measured (Fig. 1.3b). As the voltage approaches the characteristic reduction potential (E°) of the electrode during the negative voltage scan, the cathodic current begins to increase (point A). Similarly an anodic peak in the current starts to rise as the electrode starts to oxidize (point B). CV of a battery system provides qualitative information about the electrochemical reactions including thermodynamics of redox processes and kinetics of electron transfer reactions by locating and analyzing the current peaks. [16] For example, standard reduction potential or the Nernst potential of a reaction as well as the reversibility of Li^+ or Mg^{2+} insertion process can be evaluated based on the location and size of the current peaks. In addition, the CV measured at different scan rates provide information about the reactions kinetics of ion insertion process where the redox behavior of a kinetically limited reaction will start to decrease at faster scan rates.

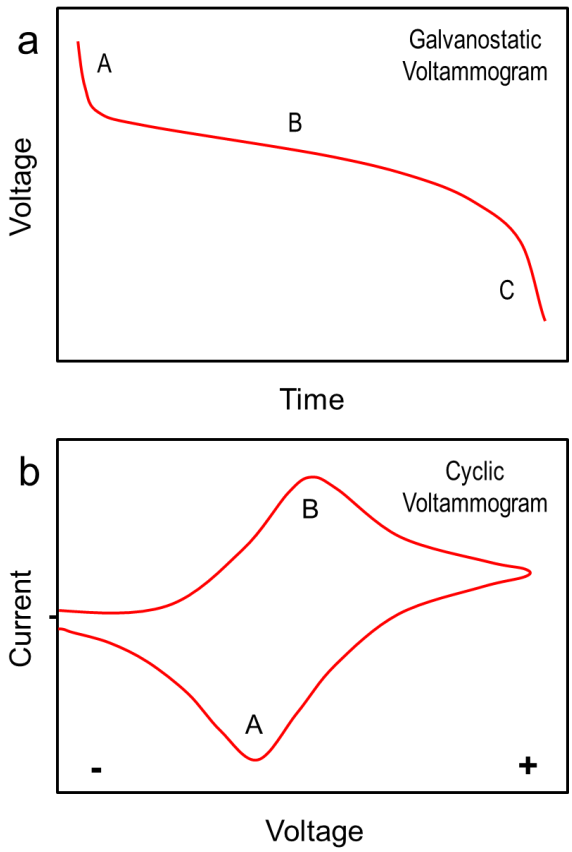

Figure 1.3 (a) Typical galvanostatic discharge curve showing voltage profile in respect to time, (b) cyclic voltammogram measuring current in respect to voltage.

1.2.3 Energy and Power

The energy (E) of a battery describes the amount of work that can be done and is the product of the cell operating voltage and the capacity[17] measured in the units of Joules or Watthour as:

$$E = QV_{cell} \qquad \text{(Eqn. 1.5)}$$

The power (P) of a battery indicates how quickly the stored energy can be retrieved; thus, power describes the rate of energy delivery (in Watt) as described in the following equation:

$$P = \frac{dE}{dt} = \frac{dQ}{dt} V_{cell} = iV_{cell} \qquad \text{(Eqn. 1.6)}$$

It is important to differentiate between the measurement of **specific** and **density** units of a battery system. The term specific indicates the measure of energy or power per unit *weight*, whereas density describes the measure of energy or power per unit *volume*. In a particular case, the one unit measurement is considered to be more important than the other. For example, having a battery that demonstrates high specific energy/power is crucial for applications of electric vehicles since the overall performance of a vehicle largely depends on its weight. On the other hand, for applications in portable electronic devices, such as laptops and smart phones, the size of the devices matters more than the weight; hence, a battery system that provides high energy and power densities is more desirable.

As elucidated previously, Mg as an anode possesses superior volumetric capacity than the graphite anode of the commercialized LIBs. Therefore the development of portable electronic devices in more compact sizes could be realized with the advancement and commercialization of Mg batteries. However, Mg battery research is thought to be in an embryonic stage with their rather low energy and power densities despite the tremendous research efforts devoted in the field. Several crucial challenges for Mg batteries are discussed in the following section.

1.3 Challenges in Mg Batteries

Mg Anode and Electrolyte Compatibility. The greatest challenge for realizing practical Mg batteries is considered to be in the development of electrolyte solutions that allow reversible deposition/dissolution of Mg metal.[18-20] The compatibility

between the Mg anode and an electrolyte system is often evaluated by a good coulombic efficiency (CE) which is defined as the ratio of the charge accumulated during the Mg deposition/dissolution.[9, 21] Poor CE may be the result of incomplete plating or stripping of the Mg, or due to side reactions which consume current without contributing to the useful reaction. Conventional electrolytes that contain organic solvents, such as carbonates, in addition to simpler Mg salts, such as $Mg(ClO_4)_2$, react with the Mg metal surface to create an SEI layer.[1, 22, 23] However, in contrast to Li based battery systems where Li^+ can transport through the SEI layer, SEI layer formed in Mg system permanently passivates Mg^{2+} ions leading to a poor CE, because Mg dissolution cannot occur through the passivating layer. This inherent incompatibility of conventional electrolytes in Mg^{2+} ion systems has led to extensive research focusing on the synthesis and structural studies of new and complex organic electrolytes that are highly stable against reductive decomposition while allowing reversible Mg deposition/dissolution.

Poor Anodic Reaction Stability of Mg Electrolytes. As discussed previously, the electrochemical window of an electrolyte is defined by the voltage domain in which neither the cathodic reduction nor anodic oxidation of the electrolyte takes place. In other words, both the salt and solvent of an electrolyte have to be stable against reduction and oxidation at the strongly reducing anode and strongly oxidizing cathode surfaces, respectively. Non-conventional types of electrolytes that are stable towards reduction at the metal surface (such as Grignard-based electrolytes) have been used for Mg batteries in order to prevent the formation of Mg passivation layer on the anode interface.[1, 24-26] However, a significant drawback of these electrolytes is

their low anodic reaction stability. In many cases, the anodic reaction stability of the electrolyte will become the bottle neck for the utilization of cathode materials whose charge/discharge voltages are higher than the stability limit of the electrolyte.

Chloride has been one of the key components for many Mg electrolytes as the it has shown to provide additional reduction stability of the electrolyte species;[27, 28] however, it also causes serious corrosion on the common current collectors such as stainless steel and aluminum.[29] This means that even though such chloride-containing electrolytes have been reported to exhibit a wide voltage window on an inert substrate such as Pt, the corrosion of less-noble substrates could occur at a lower voltage, making the "practical" voltage window narrower than the ideal case. Therefore, when considering the voltage window of an electrolyte, its stability against the current collector corrosion must be also taken into account. This implies that in many cases of chloride-containing electrolytes, the practical voltage window may be significantly narrower than the values reported with Pt current collectors.

Slow Solid-state Kinetics of Mg^{2+} ion: Lack of Cathode Materials. In order to utilize the charge storage capacity of the bulk of an insertion type cathode, ions must be able to access the entire structure. While there are more than 15 different types of cathode compounds which have shown to provide excellent electrochemical performances in Li-ion battery systems,[7] Mg^{2+} ions demonstrate poor solid-state diffusion in common cathode compounds, resulting in very low capacity and rate performances.[30, 31] Given that Li^{+} and Mg^{2+} have similar ionic sizes, the poor solid-state kinetics of Mg^{2+} is largely attributed to the additional charges that Mg^{2+} carries

compared to monovalent Li^+. Indeed, both computational and experimental studies suggest that the sluggish kinetic of Mg^{2+} originate from 1) the strong ionic interaction between the divalent Mg^{2+} and its surrounding ionic environment (i.e., ionic matrix of host compound and electrolyte species) and 2) high activation barrier for the charge redistribution upon the insertion and deinsertion of Mg^{2+}.[32, 33]

Among the few cathode compounds that have been studied for Mg battery systems, Chevrel phase (e.g., Mo_6T_8 where T = S, Se) exhibits the most reversible Mg^{2+} insertion/extraction reaction with fastest kinetics. Unlike many other cathode candidates, Chevrel phases provide a superior Mg^{2+} insertion/deinsertion capability owing to its unique crystallographic structure that is beneficial for the divalent charge transfer upon the insertion of Mg^{2+}.[10, 34-36] However, the main drawback of Chevrel phase cathode is that it exhibits an average discharge voltage of less than 1.5 V vs. Mg/Mg^{2+}. Therefore, the energy density of a prototype Mg battery utilizing Mo_3S_4 as a cathode is less than half of the commercialized Li-ion batteries and only comparable to Ni-Cd battery systems.[1]

Extensive efforts have been devoted to searching for Mg-ion cathodes with high operating voltage to achieve an energy density that is comparable to Li-ion batteries. Unfortunately, the poor solid-state kinetics of Mg^{2+} is especially drastic in many metal oxide compounds, which typically possess operating voltages greater than 2.5 V vs. Mg/Mg^{2+}.[37, 38] In summary, along with the inhibited Mg^{2+} insertion behaviors in the cathodes, the low anodic reaction stability of many Mg electrolytes as well as their corrosive nature towards oxide materials have made the development

of high voltage Mg cathode particularly challenging.

1.4 Current State of Mg Battery Research

In order to organize and illustrate the current state of Mg battery research in an intuitive way and to better illustrate how the components of a Mg battery system are related to each other, a unique set of radar charts was created and presented in Figure 1.5 to 1.7. The methodology that was used to organize all the previously reported work in a radar chart is explained below.

It is well established that the one of the crucial components for the rechargeable Mg battery is the electrolyte solution. Hence the electrolyte was chosen to be the leading component for the designed radar chart. Each radar chart ranks the electrolyte under six parameters that are either mandatory or reflects a desired breakthrough for a rechargeable Mg battery: a) compatibility with reversible deposition and striping of Mg^{2+} on Mg metal anode, b) anodic reaction stability of the electrolyte, c) stability against current collector corrosion, and d-f) compatibility with three groups of cathodes: d) higher voltage class cathodes (e.g., metal oxides), e) lower voltage class cathodes (e.g., Chevrel phase), and f) high capacity conversion cathodes, such as sulfur.

Figure 1.4 represents a blank radar chart where the metric of each component is quantified with scales of 1 to 5 that are given based on the criteria listed in Table 1.1. Please note that the center of each radar chart indicates that the corresponding component has not been explored yet. Briefly, the degree of compatibility with Mg anode was evaluated by the reported coulombic efficiency of Mg

deposition/dissolution process. For anodic reaction stability and stability against current collector corrosion, ranges of voltage window were used as evaluation standards. The ranges of voltage window were selected based on the demagnesiation voltages of common Mg-ion cathodes (vs. Mg/Mg^{2+}), e.g. 1.5 V for Chevrel phase, 2.7 V for sulfur, and 3.4 V for proposed higher voltage cathodes[6-10]. The compatibility of Mg electrolyte with three groups of Mg cathode has been represented based on the reported cycling stability accompanied with a reversible Mg^{2+} insertion capacity of the cathodes in the selected Mg electrolytes. Figure 1.4b is an example radar chart generated for dichloro-complex organohaloaluminate electrolyte (DCC)[1] which has been shown to exhibit the following electrochemical performances: 100 % CE for Mg deposition/dissolution, less than 2.2 V of anodic reaction stability and stability against current collector corrosion, over 500 stable cycles with low voltage cathodes, and incompatible with high voltage cathode and conversion sulfur cathode.

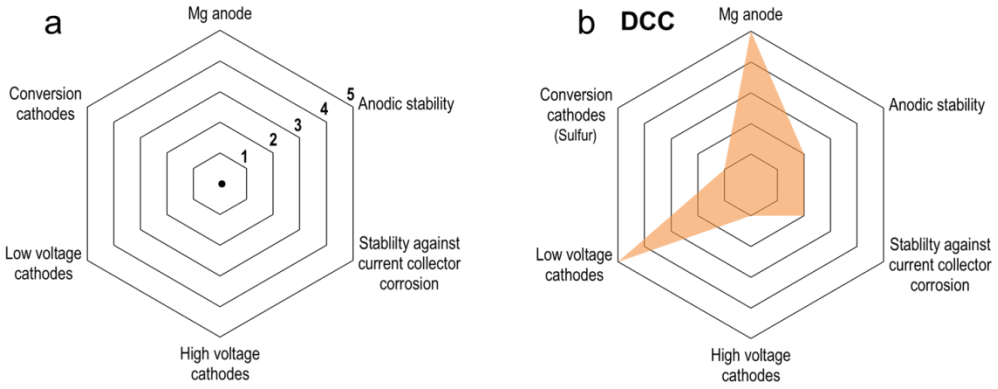

Figure 1.4 a) Blank radar chart with six electrolyte components. Each component is ranked 1 to 5 based on the criteria listed in Table 1.1. The center of the chart represents that the corresponding component has not been explored. (b) An example radar chart of DCC electrolyte that exhibits 100 % CE for Mg deposition/dissolution, 2.2 V of anodic stability and stability against the current collector corrosion, over 500 stable cycles with low voltage cathodes, and incompatible with high voltage and sulfur cathode.[1]

Table 1.1 Criteria for the scales of (a) anodic stability, (b) stability against the current collector corrosion, (c) Mg anode, and (d) cathodes.

a

Scale	Mg anode: Coulombic efficiency
1	Incompatible
2	> 80 %
3	> 90 %
4	> 95 %
5	100 %

b

Scale	Anodic stability: Voltage range (vs. Mg/Mg^{2+})
1	< 1.5 V
2	1.5 V to 2.5 V
3	2.5 V to 3.5 V
4	3.5 V to 4.5 V
5	4.5 V to 5 V

c

Scale	Stability against current collector corrosion: Voltage range (vs. Mg/Mg^{2+})
1	< 1.5 V
2	1.5 V to 2.5 V
3	2.5 V to 3.5 V
4	3.5 V to 4.5 V
5	4.5 V to 5 V

d

Scale	Cathodes: Reversible cycling stability
1	Incompatible
2	< 30 reversible cycles
3	< 100 reversible cycles
4	< 300 reversible cycles
5	< 500 reversible cycles

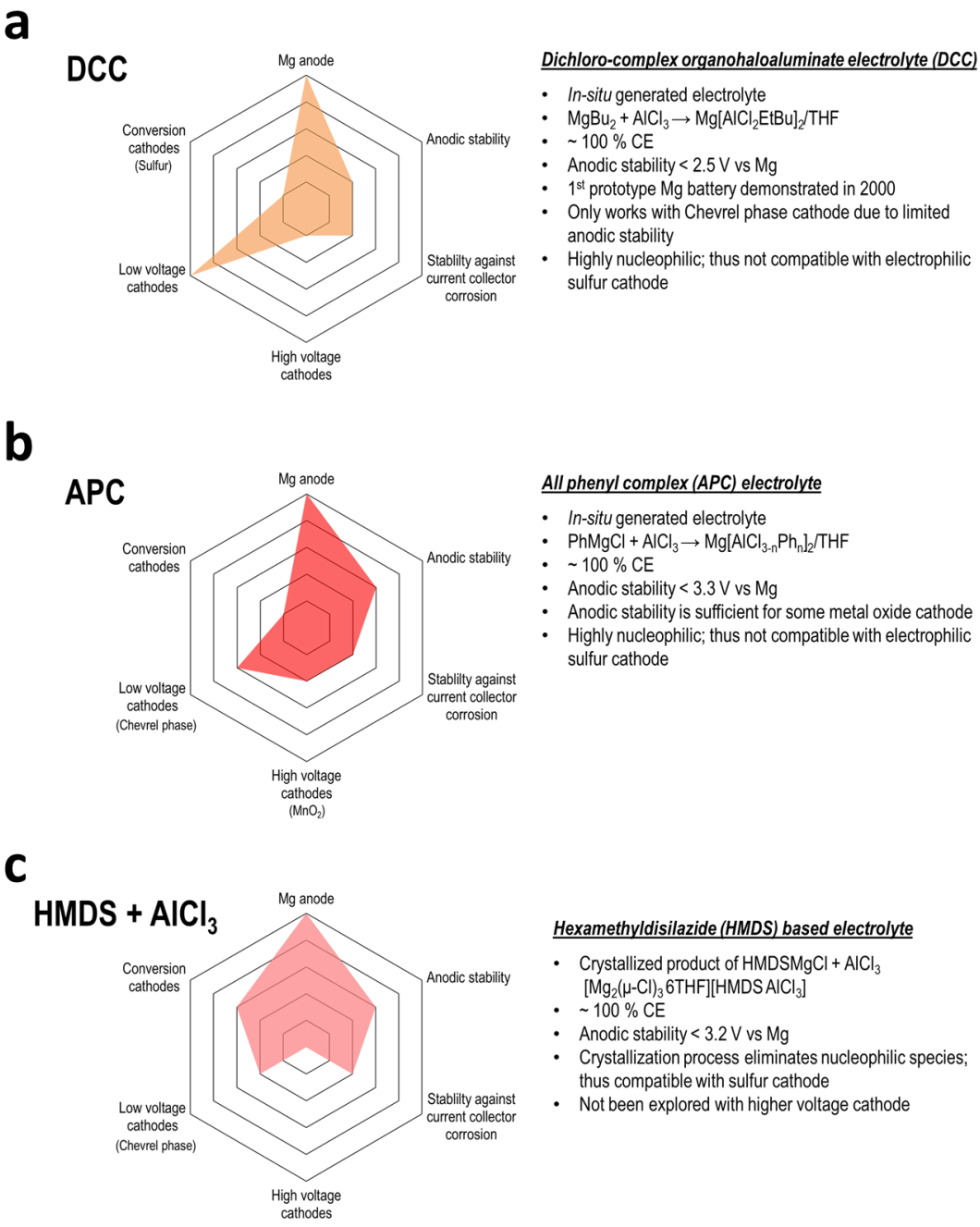

Figure 1.5 Radar charts summarizing specifications of Mg electrolytes in respect to various components of Mg batteries. (a) Dichloro-complex organohaloaluminate (DCC) electrolyte[1], (b) all phenyl-complex eletrolyte (APC)[32, 39-41], and (c) hexamethyldisilaxide (HMDS) based electrolyte[22, 42-46].

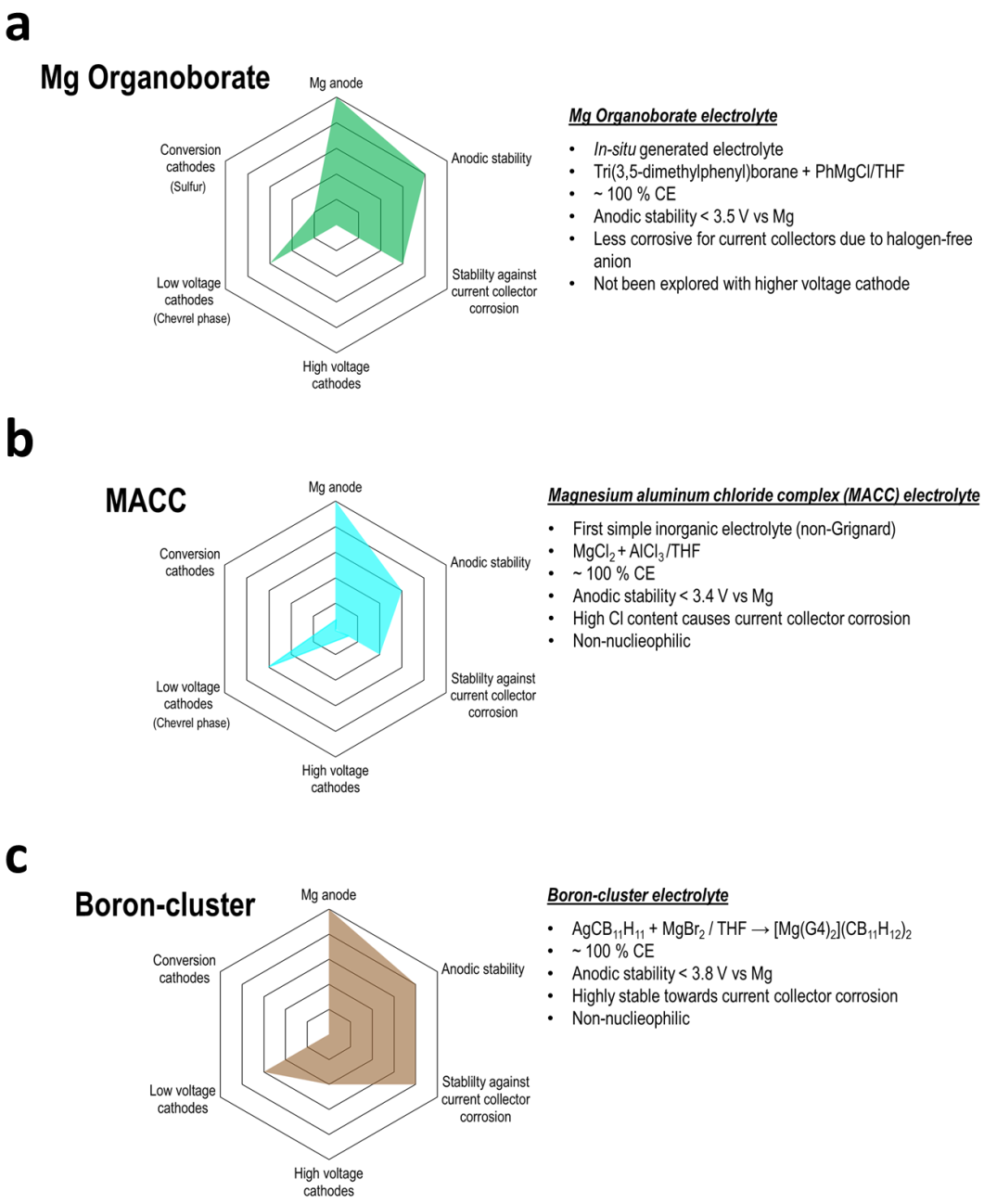

Figure 1.6 Radar charts summarizing specifications of Mg electrolytes in respect to various components of Mg batteries. (a) Magnesium organoborate electrolyte[29, 47, 48], (b) magnesium aluminum chloride complex (MACC) electrolyte[27, 49-51], and (c) Boron-cluster electrolyte[52, 53].

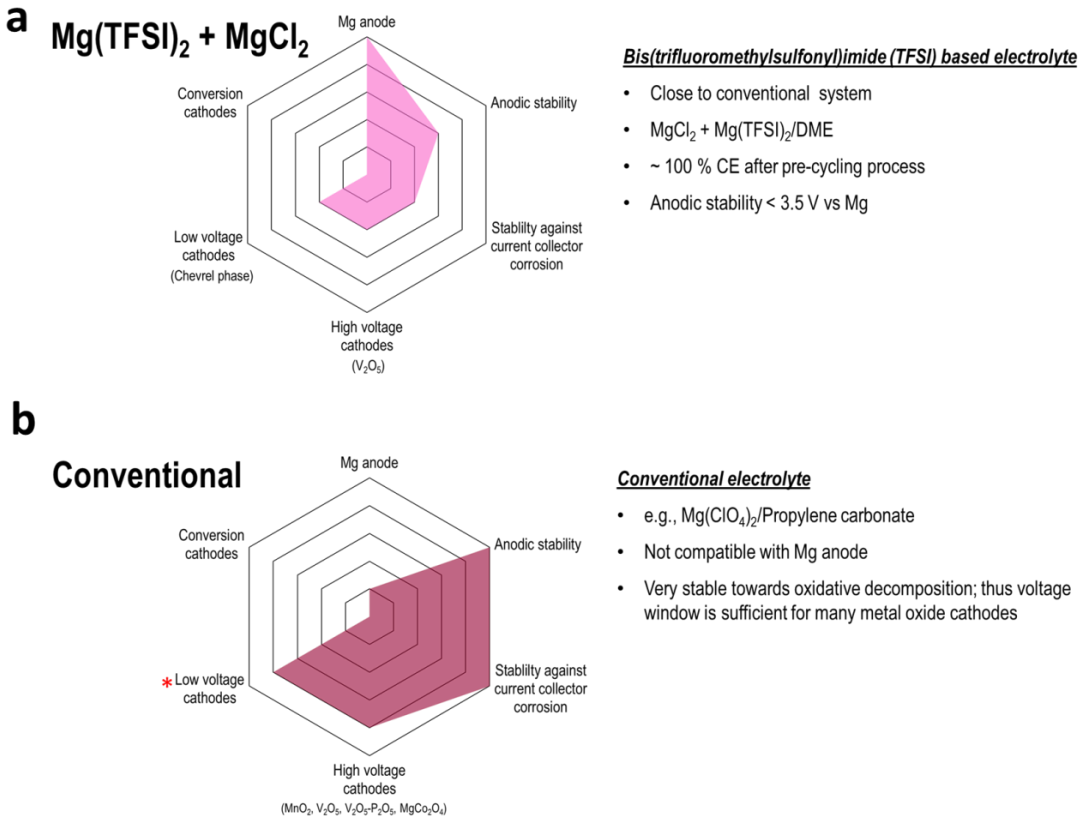

Figure 1.7 Radar charts summarizing specifications of Mg electrolytes in respect to various components of Mg batteries. (a) Bis(trifluoromethylsulfonyl)imide (TFSI) based electrolyte[54, 55] and (b) conventional type electrolytes that are commonly utilized in Li-ion batteries. * experimental data was not provided, but expected to exhibit at least the shown performance.

1.5 Overview of Dissertation

In order to demonstrate a high-voltage Mg battery and be able to provide an energy density that is comparable to that of Li-ion battery, there is need for 1) a high voltage cathode with good Mg^{2+} mobility and 2) an electrolyte which possesses a stable voltage window that can accommodate the cell operating voltage. However, the presented radar charts suggest that there is still a serious limitation in the realized Mg^{2+} insertion capacity with high voltage cathodes even with the electrolytes whose

voltage window is sufficient for higher voltage cathodes (i.e. ≥ 3.2 V vs. Mg/Mg^{2+}).

Manganese oxide (MnO_2) is one of the most well studied electrode materials due to its excellent electrochemical properties including high Li^+ ion capacity and relatively high operating voltage (i.e., ~ 4 V *vs*. Li/Li^+ for $LiMn_2O_4$ and ~ 3.2 V *vs*. Mg/Mg^{2+}).[56-59] However, unlike the good electrochemical properties of MnO_2 realized in Li-based systems, rather poor electrochemical performances have been demonstrated in Mg based systems, particularly with low capacity and poor cycling performances. While the origin of the observed poor performances is believed to be due to the strong ionic interaction between the Mg^{2+} ions and MnO_2 lattice resulting in limited diffusion of Mg^{2+} ions in MnO_2, very little has been explored regarding the charge storage mechanism of MnO_2 is with divalent Mg^{2+} ions.

When searching for promising Mg-ion cathode candidates and evaluating their prospect in Mg battery application, understanding the electrochemical properties and origins of the challenge in a particular electrode system towards Mg^{2+} ions is critical. In this regard, this dissertation presents systematic investigation of the electrochemical behavior and charge storage mechanism of MnO_2 towards Mg^{2+} ions. It is demonstrated herein that the combination of nanostructure and presence of water molecules in Mg electrolyte significantly enhances the electrochemical insertion behavior of Mg^{2+} ions into MnO_2. Further, it is presented that pre-cycling MnO_2 electrode in the water-containing electrolyte activates MnO_2 electrode where enhanced Mg^{2+} insertion behavior is continued to be observed even after removal of water molecules in the electrolyte. Finally, the role of water molecules in the Mg^{2+} insertion process and the activation mechanism for MnO_2 electrode are investigated

by series of XPS analysis. Below are list of brief summaries of the following chapters:

- Chapter 2 introduces general synthesis and characterization methods of MnO_2 and discusses the specific methods that were used in this particular study.
- Chapter 3 discusses crystallographic structures of MnO_2 and a study of charge storage mechanism of MnO_2 in Li^+ based systems.
- Chapter 4 presents a study of Mg^{2+} insertion behavior in nanostructured MnO_2 in the presence of water molecules and observed "activation" phenomenon for enhanced Mg^{2+} insertion through a pre-cycling process.
- Chapter 5 discusses the role of water molecules in Mg^{2+} insertion behavior and mechanistic studies investigated by X-ray photoelectron spectroscopy.
- Chapter 6 summarizes and provides outlooks for possible future work.

Chapter 2 Synthesis and Characterization Techniques of MnO_2

2.1 Nanostructured Materials for Energy Storage Electrodes

The ion insertion/deinsertion process in energy storage electrode materials involves a Faradaic electron transfer reaction and phase transition processes, which initially occur through the nucleation at the electrode/electrolyte interface and then in the bulk of the electrode.[60] The efficiency of the Faradaic reaction and phase transition process strongly depend on the nature of the electrode material, i.e., ion arrangements of the electrode compound, dimension, surface energy, and purity. Therefore, in order to achieve high energy and power from an electrode material, the material has to be properly designed and synthesized in a way that it maximizes the capacity and rate capability of the electrode.

Nanostructured electrodes for energy storage applications have been perhaps the most devoted research area in the past decade owing to the important advantages that nanostructures provide for achieving high energy and power. First, nanostructured electrodes provide short diffusion lengths for inserting ions (e.g., Li^+ and Mg^{2+}) and possess high electrode/electrolyte contact area, where both properties result in enhanced rate capability and power density.[61-63] In addition, compared to bulk electrodes, nanostructured electrodes can better accommodate a possible volume change strain which could occur during the cation insertion/deinsertion process; thus, it is directly related to the high cycling stability of the nanostructured electrodes[61, 64] (Fig. 2.1).

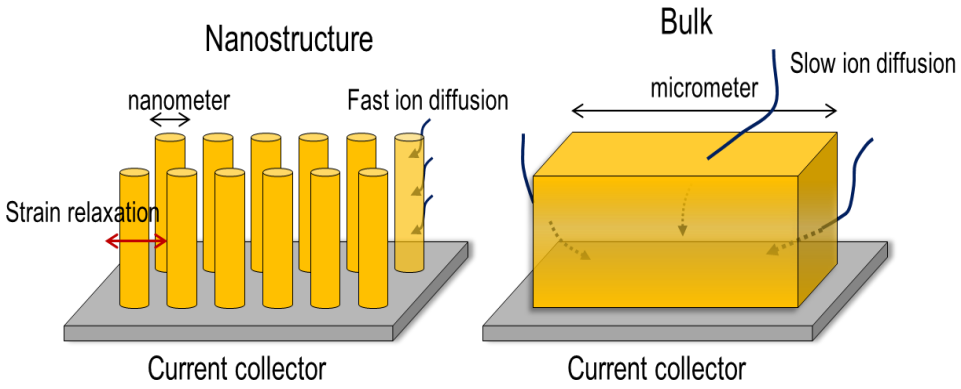

Figure 2.1 Schematic illustration of nanostructured electrode and bulk electrode.

Furthermore, the high surface area of nanostructures not only increases the reaction sites for charge transfer, it also results in increased ion insertion capacity by shifting the thermodynamic state of the electrode.[60] That is, the insertion capacity of an electrode is also affected by how far the thermodynamic state of electrode is located from the equilibrium; an electrode that is far from its thermodynamic equilibrium tends to take in more ions during the insertion process than when it is in the equilibrium state. Therefore, the high surface energy of the nanostructured materials facilitates the ion insertion process.

2.2 Synthesis Techniques of MnO_2

There has been extensive research in demonstrating MnO_2 synthesis for various applications including energy storage. The electrochemical properties of MnO_2 largely depend on its morphology, dimensionality, crystal structure, and size of the material. Therefore, a well-controlled synthesis of MnO_2 is of great significance. This section focuses on the synthesis methods of nanostructured MnO_2 for energy

storage applications.

2.2.1 Powder-based MnO_2 Synthesis Methods

Several different synthesis methods exist for MnO_2 nanoparticles including hydrothermal[65-67], sol-gel[68-70], and precipitation[71-73] methods. The hydrothermal method involves mixing precursor salts followed by a heat treatment, and is one of the most widely used methods to produce well-crystallized MnO_2 nanoparticles. The sol-gel method utilizes cross-linking reagents such as glycerol or polyvinyl acetate, which provide good control to the size of MnO_2 particles. The precipitation method is another typical method for MnO_2 synthesis which is a quick and mild condition method using the simple reaction between MnO_4^- and Mn^{2+}. These methods produce a variety of crystal structures and nanoscale morphologies simply by controlling the synthesis parameters, such as pH, concentrations, counter-cations, and temperature. However, in order to make the MnO_2 particles obtained by these methods into a functional electrode, they first need to be mixed with conductive additives for the

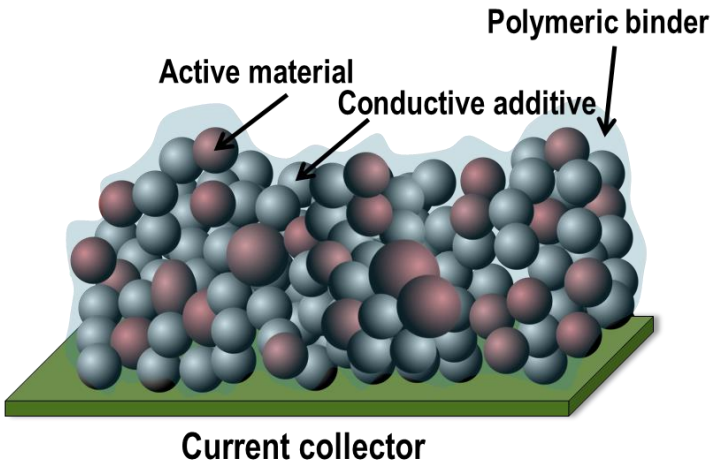

Figure 2.2 Schematic of typical slurry composite electrode.

electrical conductivity and polymeric binder to hold the powders together. This mixture including MnO_2, conductive additives, and polymeric binder – which is referred to as the slurry composite – is then pressed onto the current collector as illustrated in Figure 2.2. The slurry-based electrode is greatly appreciated in many studies due to its simplicity and scalability and has been employed for commercialized batteries. However, the conductive additives and polymeric binders do not provide any additional energy to the system while contributing approximately more than 20 % of the total weight of an electrode. In addition, from the research point of view, the tightly packed and randomly distributed composite electrode often makes the analysis of the active electrode material more difficult and less precise.

2.2.2 Direct Coating Method

To overcome the aforementioned limitations found in the powder and slurry-based electrodes, one logical way to design the electrode would be to directly coat or deposit the active material on the current collector. If the directly coated material is appropriately designed to ensure good contact between the material and current collector, there is no need for the conductive additives and binders to fabricate an electrode.

There are a few coating techniques that have been demonstrated for MnO_2 synthesis, including sol-gel dip coating[74, 75] and electrostatic spray[76] deposition. The sol-gel dip coating process involves dipping the substrate into the sol followed by drying and heating processes, where the material's thickness can be controlled by the viscosity of the sol and the number of repetitions of the dipping process. In the

electrostatic spray deposition method, a high DC voltage is applied across the substrate and a syringe that contains a precursor solution. Upon applied voltage, the precursor solution is atomized generating a spray at the tip of the needle, which is then deposited onto the substrate by the electrostatic force. However, the morphology of the materials obtained by these direct coating methods is largely limited by the morphology of the substrate and lacks in control over the materials dimension.

2.2.3 Electrodeposition of MnO_2

Electrodeposition is another well-established MnO_2 synthesis method that is simple and easy to perform to obtain MnO_2 with controlled dimension, morphology, and mass loading. In general, the electrodeposition process involves an applied electrical field or current that leads to the oxidation or reduction of charged species at the electrode/electrolyte interface, followed by the growth of a metal or alloy on the substrate.[77] Due to the unique nature of the electrodeposition process, where the material is grown only on a conductive surface, the materials can be selectively deposited with desired patterns or structures through simple controlling and modification of the substrate architecture. Synthesizing complex nanostructures through electrodeposition is further aided by the great accessibility of the plating solutions where typically low-viscosity plating solutions can fill the nanoscale voids or pores of complex structures.

In general, the set up for electrodeposition consists of a working electrode at which the deposition takes place, a counter electrode, and a reference electrode in a beaker with plating solution (Fig. 2.3). Depending on the type of reaction taking place

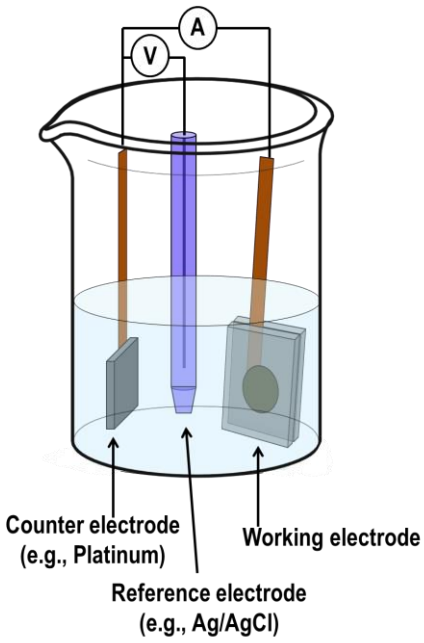

Figure 2.3 Typical set up for three electrodes electrodeposition technique in a beaker.

at the working electrode, the electrodeposition technique for MnO_2 synthesis can be categorized into 1) cathodic and 2) anodic deposition.

The cathodic electrodeposition of MnO_2 involves water electrolysis reaction which occurs upon the reductive potential or current applied to the working electrode generating hydrogen gas and hydroxide ion as shown in the following equation[78-80]:

$$2H_2O(l) + 2e^- \rightarrow H_2(g) + 2OH^-(aq) \qquad \text{(Eqn. 2.1)}$$

Furthermore, the negative polarity of the working electrode attracts Mn^{2+} dissolved in the electrolyte after which it reacts with hydroxide ions generated by water electrolysis and precipitate as $Mn(OH)_2$. MnO_2 is formed by the oxidation of $Mn(OH)_2$, which readily oxidizes in the presence of oxygen:

$$Mn^{2+}(aq) + 2OH^-(aq) \rightarrow Mn(OH)_2(s) \xrightarrow{O_2} MnO_2(s) \qquad \text{(Eqn. 2.2)}$$

The main advantage of utilizing cathodic deposition of MnO_2 is that the hydrogen gas bubbles formed during the electrolysis of water at the surface of working electrode produce MnO_2 with porous morphology that is often beneficial to achieving high capacity and rate capability[79].

During the anodic electrodeposition of MnO_2, Mn^{2+} cations dissolved in the electrolyte solution are oxidized upon the oxidative potential or current applied to the working electrode[81-83], which then react with water and deposit as MnO_2

$$Mn^{2+}(aq) + 2H_2O(l) \rightarrow MnO_2 + 4H^+(aq) + 2e^- \qquad \text{(Eqn. 2.3)}$$

The anodic deposition of MnO_2 has been widely employed, thanks to its simple one-step process, and it is the main MnO_2 synthesis technique that is used in the study presented in this thesis.

2.3 Synthesis of One-Dimensional MnO_2 Nanowire Arrays

A two-dimensional (2D) film structure is the simplest structural form that can be obtained through electrodeposition, where a material is deposited onto a planar substrate. Several thin-film MnO_2 electrodes with a thickness of less than 100 nm have been reported to provide superior specific capacity in Li-ion based system that is close to the theoretical value, as well as great rate capability owing to the short electronic and ionic diffusion path lengths of the thin-film structure[74, 84, 85]. However, in a practical energy storage device, the thinness of the film-based electrode becomes an issue as the low mass loading per unit area results in limited volumetric energy capacity.[86] Increasing the mass loading by growing thicker film comes with longer ionic/electronic diffusion path lengths, thereby resulting in in power loss. There is

always a strict tradeoff between the amount of energy that can be stored and the rate of the energy releasing process in a 2D film-structured electrode.

On the other hand, a well-ordered one-dimensional (1D) nanowire array, where the wires are grown in the direction perpendicular to the current collector, offers more mass loading per unit area compared to the thin-film, while maintaining fast electronic and ionic diffusion characteristics due to a higher surface area and more active sites available for charge transfer reactions.[57, 59, 64]

As discussed previously, electrodeposition of various nanostructures is assisted by using unique substrates by which the growth of the material is guided. The synthesis of a well-ordered and free-standing 1D nanowire array typically involves utilization of porous membrane as a sacrificial template, such as polycarbonate and anodized aluminum oxide (AAO).

AAO is one of the most widely employed hard templates in fabricating 1D nanowires and nanotube structured materials due to its attractive properties including high pore density and great chemical/thermal stability. In the following subsection, detailed structural properties and fabrication process of AAO are discussed.

2.3.1 Anodized Aluminum Oxide

The unique ordered porous structure of AAO is generated by self-ordered electrochemical process during the electrochemical anodization of aluminum (Al) in acidic electrolytes. The pores of AAO, with their density typically ranging from 10^9 to 10^{11} cm^{-2}, are in the form of densely packed hexagonal cells in the direction normal

to the Al surface.[87] A schematic illustration of an AAO structure is presented in Figure 2.4. The characteristic pore parameters, such as pore diameter, cell distance, wall thickness, pore length, and barrier layer thickness, can be controlled by adjusting the anodization conditions (i.e., applied voltage, current, electrolyte, and anodization temperature).

AAO membranes with high degree of pore order can be obtained from an extended period of Al anodization under an appropriate voltage and electrolyte environment where the initially formed random-ordered pores self-organize, forming a regular hole configuration.[88] However, this process requires a long anodization time (up to 160 hours) and generates very thick porous alumina. The two-step anodization method, first developed by Masuda and Satoh in 1996,[89] can produce a thin AAO membrane with a highly ordered pore array in a reduced time period. The two-step anodization process involves the removal of the anodic oxide layer formed during the first anodization. This allows for the generation of a concave and indented texture on

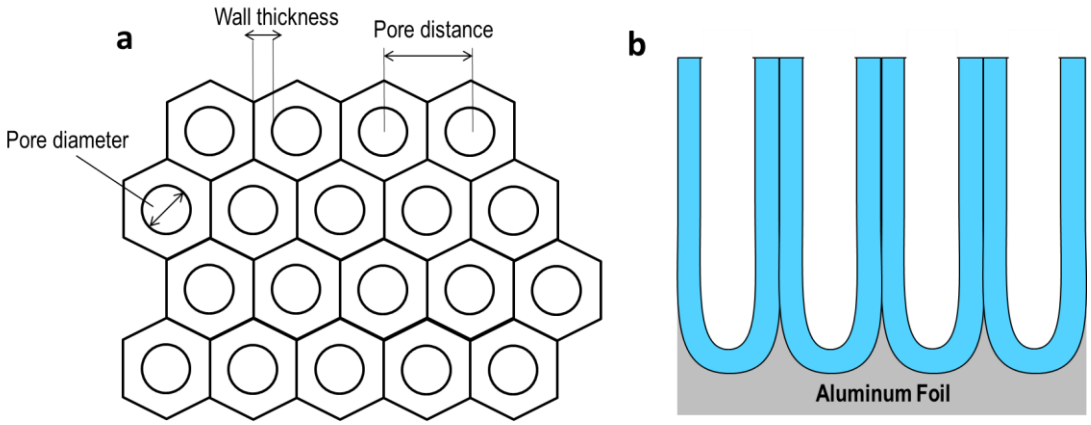

Figure 2.4 Schematic of AAO pores (a) Top view and (b) side view.

the Al surface, which becomes the initiation site for the pore formation. The second anodization on the textured Al surface produces an ordered formation of the pores. More recently, it has been reported that patterning the Al surface prior to the anodization process by employing beam lithography or template can also produce well-ordered pore arrays.[87] After the second anodization process, the remaining Al layer of AAO is removed to form a through-hole membrane. A schematic representation of the two-step anodization process is found in Figure 2.5.

2.3.2 Electrodeposition of Nanostructure with AAO Template

Combined with other coating/deposition techniques, such as sol-gel[75], atomic layer deposition[90, 91], and chemical vapor deposition[92], AAO has been widely applied in fabricating nanowires or nanotube structures. Furthermore, AAO has been coupled with electrodeposition,[93-95] producing various nanostructured materials using a simple experimental setup with easy control over the nanowire/nanotube diameter, length, and density.

In order for an electrically insulating AAO to be utilized as a substrate for electrodeposition, a metal is typically sputtered or evaporated onto one side of the membrane. For example, for the electrodeposition of MnO_2 nanowire utilized in the current study, gold or platinum was vacuum sputtered on one side of the AAO template to serve as a current collector as shown in Figure 2.6. The metal sputtered AAO template is then assembled into a working electrode configuration which involves defining the area (pore side up) for deposition and attaching a strip of copper

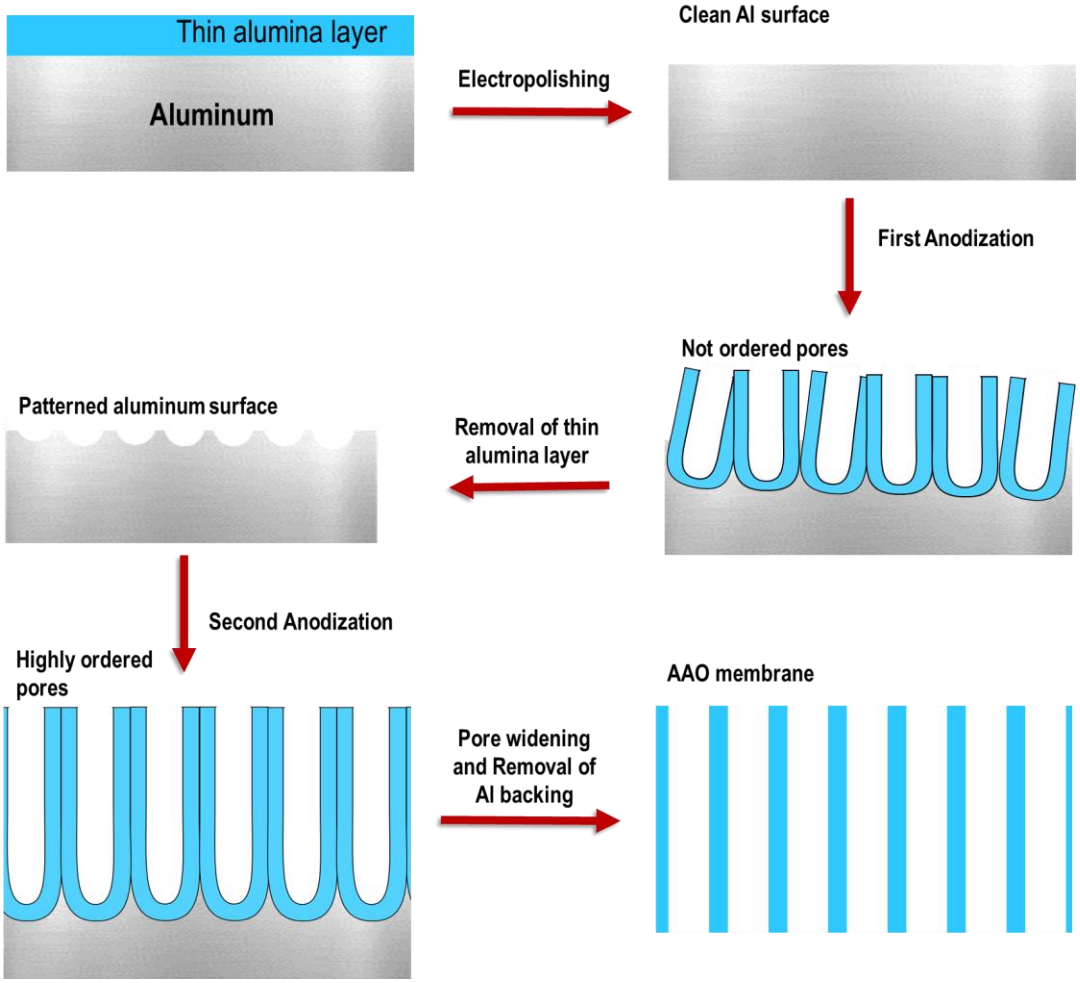

Figure 2.5 Schematic of the two-step anodization process for AAO membrane.

tape on the metal sputtered side for the electrical contact with an external voltage/current source (Figure 2.6). Using the three-electrode set up as described in section 2.2.3, the material is grown inside the pore and a free standing array of nanowires or nanotubes is obtained after the template is removed in acidic (e.g., 3 wt % H_3PO_4) or basic (e.g., 3 M NaOH) solutions.

2.4 Characterization Techniques of MnO_2

The fast development of nanostructured materials in rather complex architectures requires suitable characterization techniques that can probe the material with high degrees of sophistication. The following subsections discuss several widely recognized characterization techniques for nanomaterials that are utilized in the current study for the characterization of MnO_2 nanowire/film.

2.4.1 Electron Microscopy

For observing the morphology of nanostructured materials on a nanometer scale, the optical microscopy technique cannot provide fine details of the structure due to its theoretical limitation determined by the physics of light. On the other hand, electron microscopy uses a beam of energetic electrons in place of light to image the sample specimen where the interaction between the beam of electrons and sample is

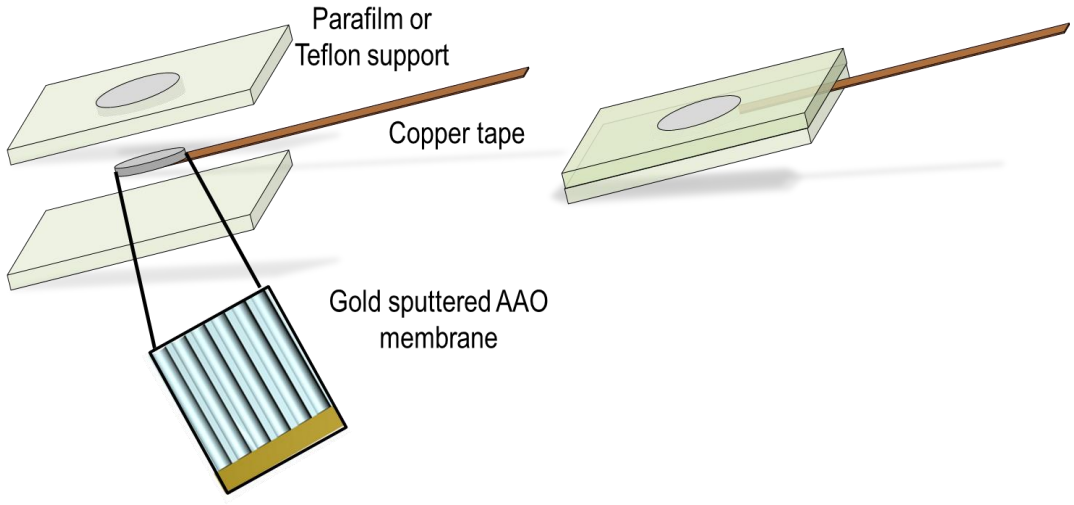

Figure 2.6 Schematic of working electrode configuration for electrodeposition on AAO membrane.

detected and transformed into an image; hence it permits examination of materials on a nanometer scale.[96]

In scanning electron microscopy (SEM), a beam of electrons scans and passes through the sample surface and the emission of electrons (i.e., secondary electrons and back-scattered electrons) occur as a result of the interaction between the electron beam and sample. The emitted electrons are then collected by detectors to generate an image of the sample under test. SEM can generate a very high resolution image of the surface topography of samples of up to 1 nm resolution under an optimum condition.

To prepare an SEM sample of free-standing MnO_2 nanowires grown on a current collector, the sample can be simply attached (with current collector side facing down) to an SEM sample holder using a double-sided conductive tape. It is important to note, however, the nature of SEM operation requires the sample specimen to be conductive. Otherwise, the incident electrons will be accumulated on the sample surface causing a phenomenon known as the charging effect, which will deteriorate the image information. Therefore, when preparing for SEM samples of non-conducting materials, such as AAO or MnO_2, the sample surface needs to be coated with a thin conductive film or connected to carbon tape to bridge the sample to the sample holder and avoid the charging effect. Figure 2.7a shows a SEM image of free-standing MnO_2 nanowire arrays.

In transmission electron microscopy (TEM), the incident beam of electrons interacts and penetrates (or transmits) through a thin sample specimen. The transmitted electrons are transformed into a magnified image and projected onto a

fluorescent screen and charge-coupled device (CCD) camera. Since the transmission of electrons is inversely proportional to the thickness of the sample specimen, the thickness of the sample is normally controlled to be less than 1 μm. In addition, TEM provides very high resolution images, which allows this technique to probe samples as small as a single column of atoms down to 0.2 nm, and examine their atomic orientation, arrangements, and spacing.

For the TEM analysis of MnO_2 nanowires, two different methods were used in the current study to prepare the sample specimen. First, to obtain TEM samples of individual MnO_2 nanowires, the array sample was sonicated in ethanol by which the nanowires were detached from the current collector and dispersed in the solution. The MnO_2 nanowire suspension solution was then dropped onto the TEM grid followed by a drying process. Figure 2.7b shows a typical TEM image of MnO_2 nanowires.

One of the important scientific questions for an electrode is whether its charge storage reaction happens mostly near the surface or throughout the bulk of the material as it determines the governing mechanism of the electrode charge and discharge process. Examination of cation insertion depth within discharged MnO_2 nanowire can be done by observing the radial distribution of the nanowire's cross-section. However, as shown in the Figure 7b, the nanowires lie in the direction perpendicular to the electron beam once they are separated from the current collector. Therefore the cross-section of the nanowires cannot be examined, although the line scan of energy dispersive X-ray spectroscopy (discussed in the following subsection) can provide indirect information of the elemental composition of nanowire in radial

distribution.

In this study, a direct observation of the cross-section of MnO_2 nanowires was enabled by embedding the free-standing MnO_2 nanowire arrays in an epoxy which was then finely sliced using a microtome. This method allows for a direct examination of the cross-section of the nanowire and radial distribution of elements by providing a "top view" of the nanowires. The schematic of the microtome process and a TEM image of microtomed MnO_2 nanowire array are shown in Figure 2.8.

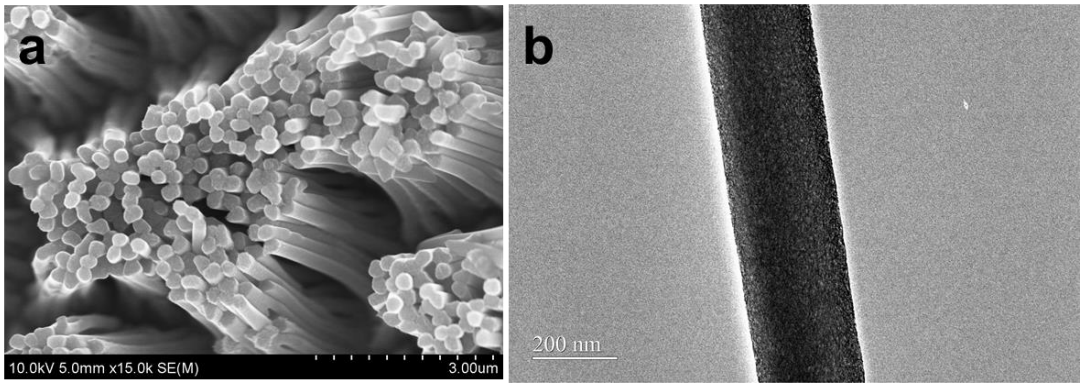

Figure 2.7 (a) SEM and (b) TEM images of as-prepared MnO_2 nanowires.

2.4.2 Energy Dispersive X-ray Spectroscopy (EDS)

In SEM and TEM, X-rays generated by the relaxation of the excited electrons of the sample upon irradiation by the electron beam can be collected by X-ray detectors. The emitted X-rays are measured with respect to their energy. Since each element possesses a unique set of atomic levels, where the emitted X-ray is the characteristic of the element, both qualitative and quantitative elemental analysis can be done through EDS.[96]

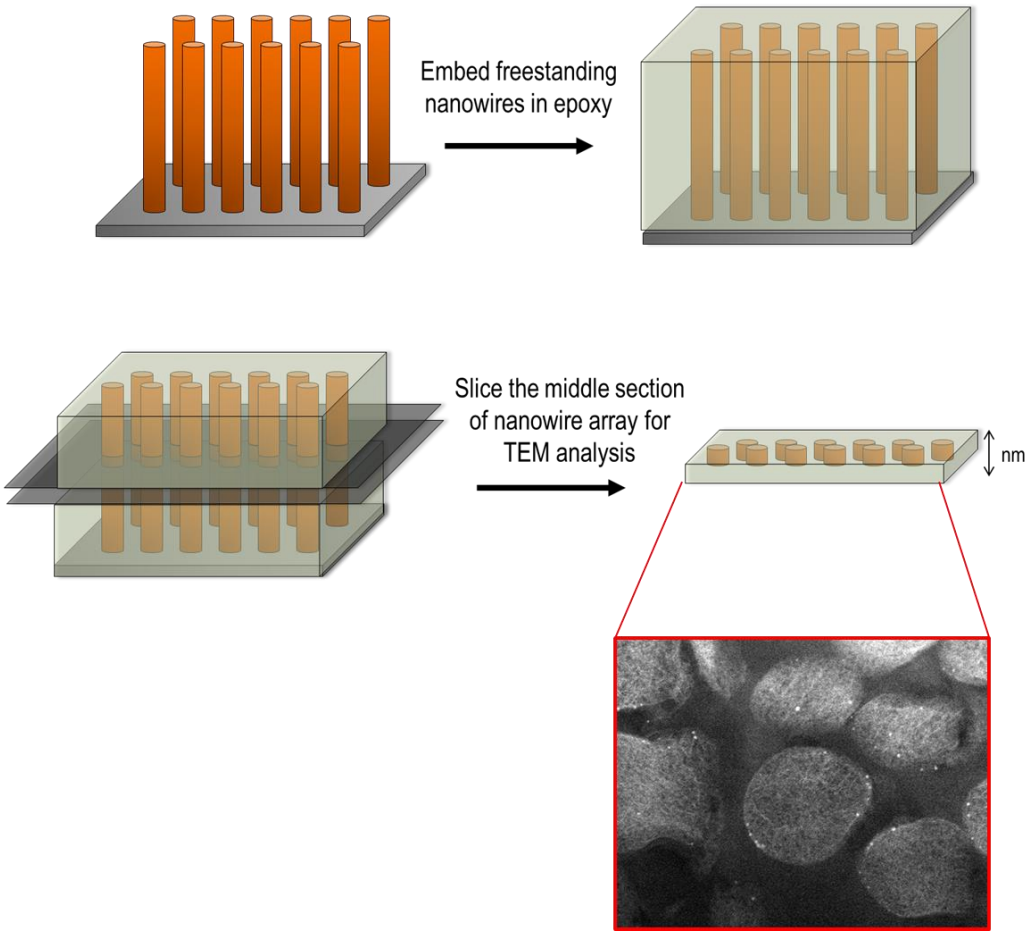

Figure 2.8 Schematic of microtome process for TEM analysis of cross-section of nanowires.

Elemental analysis by EDS can be conducted over certain spots or larger areas of a sample providing individual spectra of the corresponding region. As discussed earlier, the radial distribution of elements can be monitored by EDS modes of elemental mapping or line scanning profiles.

2.4.3 Inductively Coupled Plasma – Atomic Emission Spectroscopy (ICP-AES)

Inductively Coupled Plasma – Atomic Emission Spectroscopy (ICP-AES), is an elemental analysis technique based on the spontaneous emission of photons from

the atoms and ions of the analytes that have been excited by plasma generated by radio frequency.[97] In ICP-AES, samples are typically introduced as liquid; therefore solid materials have to be digested in highly concentrated acid, such as aqua regia (i.e., a mixture of nitric acid and hydrochloric acid) prior to the analysis. The samples are injected directly into the instrument and converted into an aerosol by a nebulizer. As the aerosol meets the high temperature (~10,000 K) of the inductively coupled plasma, it quickly vaporizes and the analytes are liberated as free atoms in the gaseous state. These atomized analytes then undergo further ionization and excitation by plasma followed by the relaxation to the ground state via emission of photons. The elements are identified based on their characteristic energies, recorded as the wavelength of the photons they emit. Finally, the emitted photons are collected and directed to a detector where the intensity of emission is measured.

ICP-AES offers qualitative and quantitative elemental analysis of more than 70 elements including lithium. Lithium, due to its low atomic number, is not readily detected in many other elemental analysis techniques including EDS. The superior detection limits of ICP-AES technique allows quantification of many elements down to parts per billion (ppb) range. Therefore, the current study has utilized ICP-AES method to analyze the MnO_2 electrode during the discharging/charging process.

In general, the ICP-AES samples of MnO_2 nanowires (or film) were prepared by dissolving the nanowire array in aqua regia, followed by dilution to a known volume. The calibration curve for each element of interest was generated by a set of standard samples and was used to determine the concentrations of the sample

elements. Figure 2.9 shows a typical calibration curve obtained for Mn measured at a wavelength of 257.61nm.

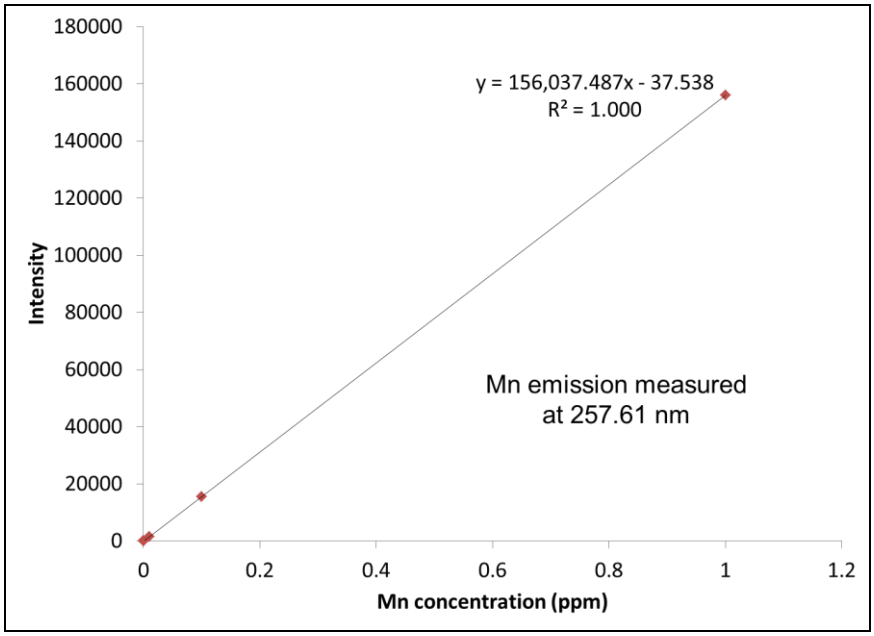

Figure 2.9 Calibration curve generated for Mn at a wavelength of 257.61 nm.

2.4.4 X-ray Photoelectron Spectroscopy (XPS)

In order to determine more detailed information about a material's elemental composition, and the bonding and oxidation states of these elements, X-ray photoelectron spectroscopy can be used. In X-ray Photoelectron Spectroscopy (XPS), a sample is exposed to an X-ray source which typically consists of aluminum or magnesium target that emits a constant energy in the X-ray range upon the bombardment with an electron beam.[98] As one of the photons in the X-ray beam of known energy displaces electrons in the sample, the kinetic energy of these emitted electrons (or photoelectrons) are measured by an electron spectrometer. The binding

energy of an electron is then calculated by subtracting the measured kinetic energy of photoelectrons from the energy of photons in the X-ray. Since every electron in an atom has its own characteristic binding energy, XPS can provide information regarding the atomic composition of a sample. Qualitative information can also be obtained since the intensity of the measured electrons at a certain binding energy depends on the amount of corresponding atoms in a sample. Moreover, the variation in valence electrons, types of bond they form, and attached functional groups can influence the binding energy, resulting in a position shift of the maximum, from which the valence state and structure of the compound can be obtained. For example, when one of the valence electrons is removed, thus oxidized, the effective charge sensed for the core electron is increased, yielding higher binding energy. This makes XPS an excellent tool for obtaining detailed characterization of the oxidation states in energy storage electrodes. For example, the magnitude of Mn 3s peak separation (ΔE) between the two split peaks, which is caused by the coupling of non-ionized 3s electrons with electrons in 3d valence shell, is often used to determine the oxidation state of Mn; lower valence state of Mn shows greater ΔE than higher valence state (e.g., Mn^{2+} ~ 6.0 eV Mn^{4+} ~ 4.7 eV).[84, 99]

Although Mn 3s peaks provide useful information for the valence state of Mn, Mn 2p spectra were used in this study for investigating Mg^{2+} insertion in MnO_2, as the Mg 2s (89.05 eV) and Mn 3s (83.59 to 90.32 eV) peaks overlap, which cannot not be resolved even with a careful deconvolution. However, compared to Mn 3s, the information provided by Mn 2p is not very reliable due to very small shifts between the different valence states that are often less than the resolution of the detector. Thus,

Mn 2p spectra were used only as a supporting set of data providing approximation of the Mn valence state changes during the electrochemical reactions of MnO_2.

O 1s XPS spectra can consists of many peaks resulting from metal oxide, hydroxide, metal carbonates, and oxygens bound to organic (e.g, organic C-O and C=O) and inorganic components (e.g., O-F_x).[100] The interpretation of O 1s spectra is not very straightforward especially when a compound is composed of multiple oxygens bound to different functional groups generating broad peaks with multiple overlapping components. Therefore, a careful peak fitting with appropriate constraints and comparison of information obtained from O 1s to its related region (e.g, C 1s) have to be imposed when analyzing O 1s spectra. Figure 2.10 shows a typical XPS spectrum of an as-prepared MnO_2 film for Mn 2p and O 1s regions. It is important to note that if the samples are insulating, there could be a peak shift by the sample charging effect. Therefore all XPS spectra obtained in this research for MnO_2 were calibrated based on a known energy value of C 1s, C-C peak at 284.8 eV prior to the analysis.

XPS is a surface-sensitive technique which means that it can only collect information from the near surface of a sample (< 10 nm) since the photoelectrons ejected from a depth greater than 10 nm will lose most of its energy before it can escape from the sample and reach the detector.[98] For energy storage applications, the highly surface-sensitive nature of XPS provides detailed surface chemistries of electrode materials, such as the composition of newly formed electrode/electrolyte interphase.

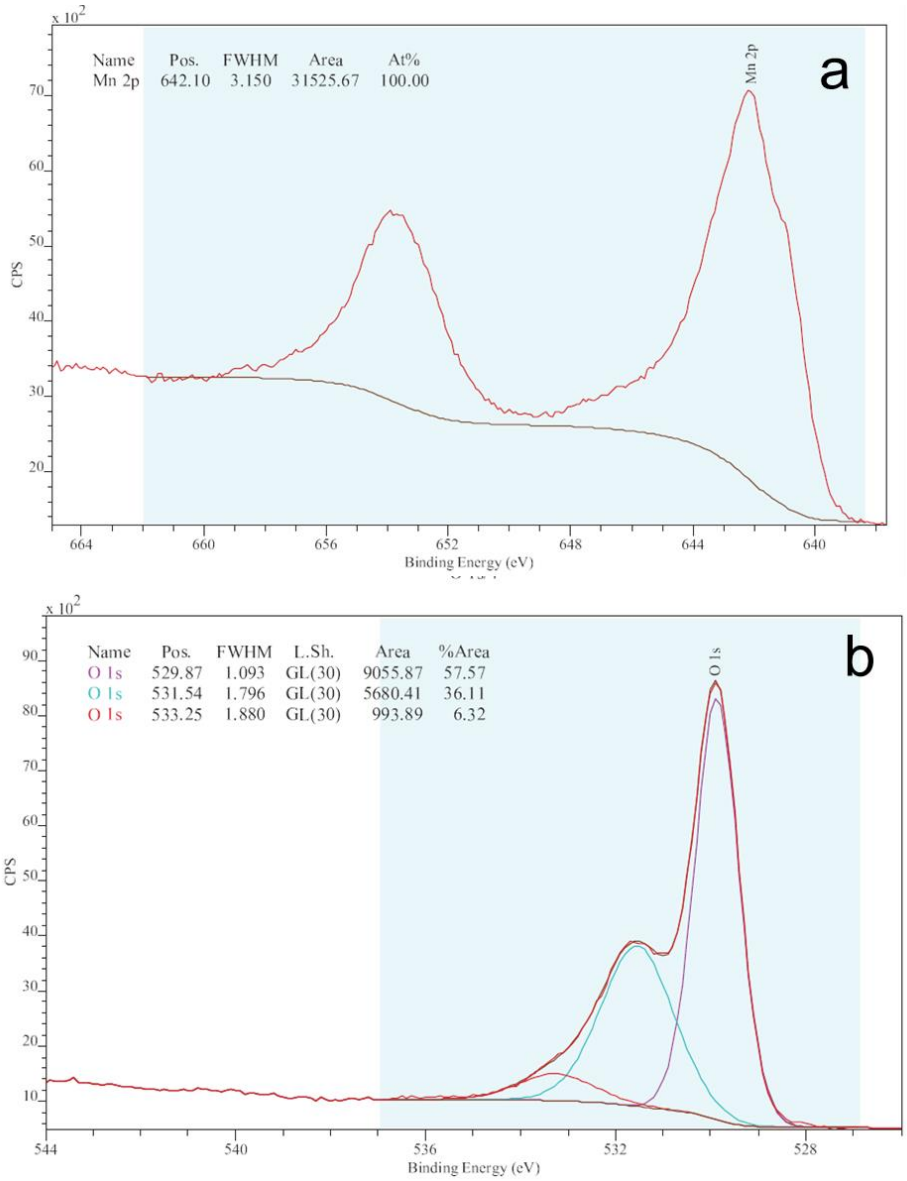

Figure 2.10 XPS spectra of as-prepared MnO_2 film (a) Mn2p region and (b) O1s region. The spectra were calibrated to 284.8 eV prior to analysis. The evolution of shoulder peak at 641 eV is used to estimate the Mn valence state change during the discharge/charge of MnO2 electrodes. The three peaks in O 1s region at 530 eV, 531 eV, and 533 eV are attributed to oxygen component in Mn bound oxide, MnOOH, and structural water, respectively.

To prepare samples of MnO_2 for XPS analysis, both film and nanowire structured MnO_2 were used. The MnO_2 electrode was attached to a double-sided copper tape on an XPS sample holder. Since the surface of discharged and charged

MnO_2 samples can undergo surface reactions upon the exposure to air generating contamination, the air exposure time was minimized by delivering the samples to the XPS chamber immediately after the electrochemical testing. Otherwise the samples were stored in argon atmosphere prior the analysis.

However, while XPS provides detailed chemistries of a material's surface, the composition and chemical state of the bulk portion of the material cannot be confirmed by XPS spectra. In addition, for this particular study, the overlapping of Mg 2p and Mn 3s regions in XPS spectra makes the evaluation of Mn valence state very difficult. For these reasons, Raman spectroscopy was used to complement the data obtained by XPS.

2.4.5 Raman Spectroscopy

Raman spectroscopy is based on the inelastic scattering (or Raman scattering) of a monochromatic light, typically generated from a laser.[97] When a beam of light excites electrons to a higher energy level that corresponds to the frequency of the incident light, most of excited electrons will relax back to its original vibrational state emitting the same frequency of the light source. However, about 0.001 % of the laser light will interact with a sample, generating photons whose energy is shifted either up (Anti-Stokes) or down (Stokes) in comparison to the original incident light frequency. The shift in the frequency provides information about vibrational modes of molecules. Since the vibration information is characteristic to the nature of chemical bond and molecular symmetries, structural information including the phases of materials can be obtained.

Raman spectroscopy was used in the current research to study the structural variation of MnO_2 upon the charge and discharge and to supplement the XPS analysis.

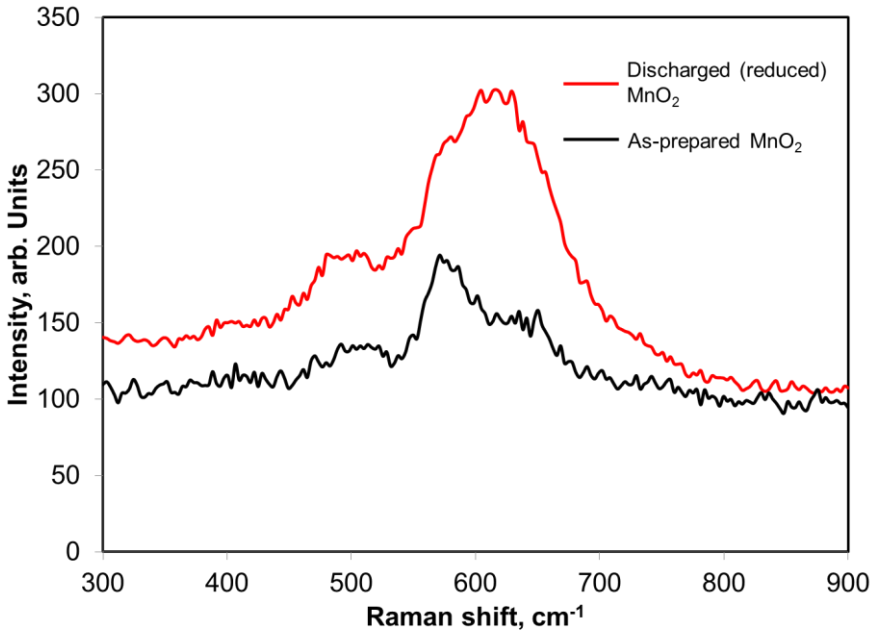

Figure 2.11 Raman spectra of as-prepared (black) and reduced (red) MnO_2. The two distinct peaks at 577 and 635 cm^{-1} in as prepared MnO_2 correspond to the Mn-O stretching in basal plane of MnO_2 and the symmetric stretching vibration of Mn-O in MnO_6 groups, respectively. Upon discharge, the two peaks are diminished and a broad peak centered at 604 cm^{-1} was appeared which is attributed to the reduction of Mn^{4+} to a lower oxidation state upon the insertion of Mg^{2+}.

Specifically, as discussed in the previous subsection, the overlapping of Mg 1s and Mn 3s XPS peaks make the determination of Mn valence state very challenging by XPS analysis. In this regards, Raman vibrational modes of MnO_2 at various charge state was analyzed to indirectly probe the oxidation and reduction behavior of MnO_2 during electrochemical reactions.[101] Additionally, since Raman spectroscopy can analyze the bulk portion of a material, it provides additional information that the

surface limited XPS analysis could not offer.

Figure 2.11 shows the Raman spectra of as-prepared MnO_2 and electrochemically reduced MnO_2, where the peak shift and peak broadening are observed in reduced MnO_2 compared to the as-prepared MnO_2.

2.5 Conclusions

A well-ordered, binder and conductive additive-free MnO_2 nanowire electrode can be prepared by electrodeposition method utilizing AAO membrane as a template. The unique 1D free-standing structure of MnO_2 nanowires not only is beneficial for the electrochemical performance of the material facilitating the ion diffusion process, but also allows precise analysis of the MnO_2 electrodes at various charge state. Various characterization techniques enable probing and monitoring of the materials with high degrees of sophistication.

Chapter 3 Manganese Dioxide as an Electrode Material for Energy Storage

Portions of this chapter have been published in Song et al., "The reversible anomalous high lithium capacity of MnO_2 nanowires", Chem. Commun. ***2014****, 50, 7352, part of which was initiated by Dr. Jonathon Duay and included in his dissertation.*[102] *Further studies were performed and new results have been generated as part of this dissertation. My contribution in particular is in the elemental analysis, electrochemical testing, pH studies, and ex-situ Raman spectroscopy studies.*

The history of manganese dioxide (MnO_2) as an electrode material for electrochemical energy storage traces back to the 1950s when a primary alkaline battery consisting of zinc anode and MnO_2 cathode was first introduced and commercialized.[103] Since then MnO_2 has been further exploited as rechargeable secondary energy storage systems, such as Li-ion battery[103-106] and supercapacitor[57, 59, 64, 71, 107] applications. Both MnO_2 and its lithiated counterpart $LiMnO_2$ were found to offer not only high energy and power density but also significant cost and safety advantages when compared to the other transition metal-oxide based electrodes (e.g., cobalt oxides and nickel oxides). In the following sections, various crystallographic structures of MnO_2 and their charge storage behaviors in Li^+ ion system are discussed.

3.1 Crystal Structures of MnO_2

The basic structural framework of MnO_2 consists of MnO_6 octahedra that are interlinked by sharing its vertices and edges.[108, 109] Depending on how the MnO_6 octahedral "building blocks" are piled up, MnO_2 can exist in several different

crystallographic forms, namely α, β, γ and δ-MnO_2 as illustrated in Figure 3.1. In α and β type- MnO_2, the edge- and corner-sharing MnO_6 octahedral units form 1D channels of (2×2) and (1×1) tunnel structures, respectively, whereas γ-MnO_2 forms the spinel 3D tunnel structure. In δ-MnO_2, sheets of MnO_6 octahedra form a layered structure with defined interlayer distance. Because the charge storage process of MnO_2 involves the diffusion of charge carrier ions through the open spaces within the structure, the electrochemical behavior of MnO_2 can vary significantly among the different crystal structures with their unique tunnel sizes or interlayer distances.[110]

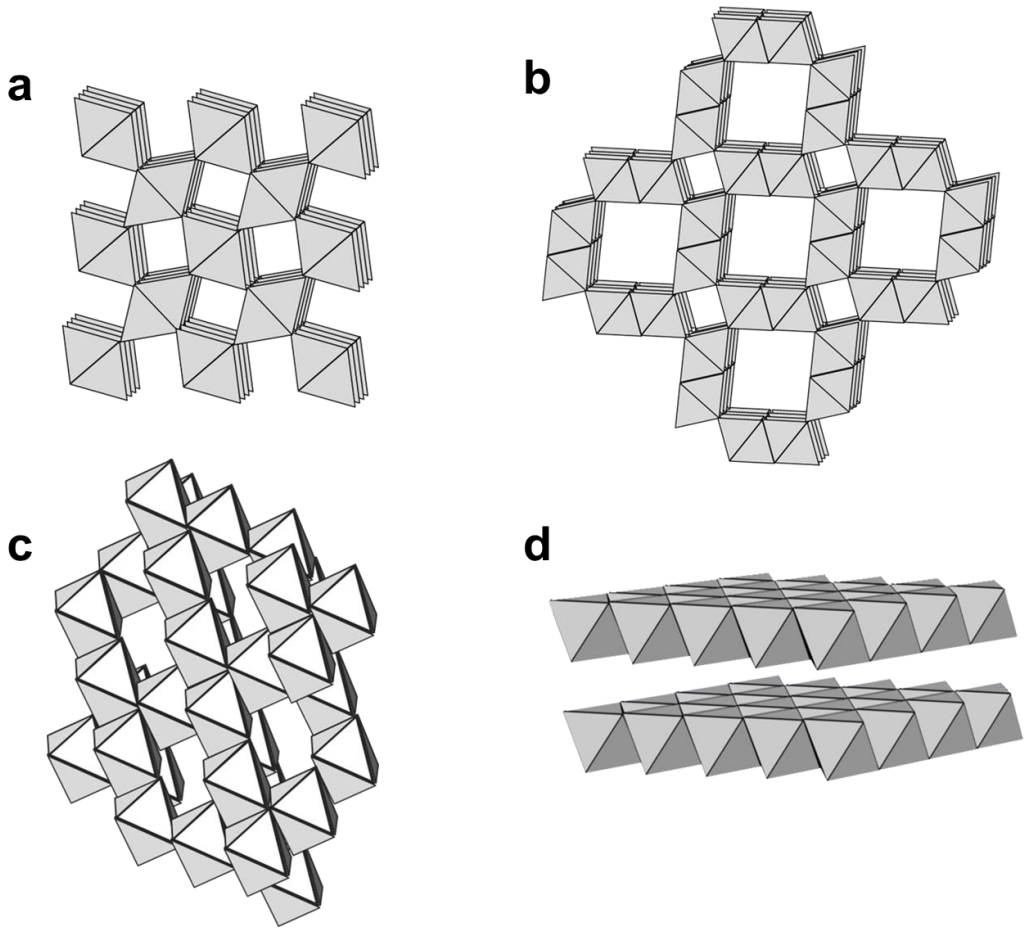

Figure 3.1 Different MnO_2 crystal structures: (a) β-MnO_2 (1×1) tunnel structure, (b) α-MnO_2 (2×2) tunnel structure, (c) γ-MnO_2 (3D tunnel), and (d) δ-MnO_2 (layered).

For example, the narrow 1D channels of β-MnO_2 often makes the diffusion of ions more difficult than the other structures. It has been reported that highly crystallized β-MnO_2 can accommodate only 0.2 Li^+ ions per formula unit at room temperature, indicating that the majority of the reaction takes place only at the surface due to the limited diffusion capability through the structure.[110] On the other hand, the two-dimensional interstitial space between the layers of δ-MnO_2 facilitates the ion transport, delivering superior Li^+ ion capacity that is close to the theoretical capacity of MnO_2 (i.e., 308 $mAhg^{-1}$ for 1 Li^+ incorporation per formula unit). As a result, spinel MnO_2 is the phase most often found in commercial lithium ion batteries.

3.2 Amorphous MnO_2

In general, nanocrystalline or amorphous phase compounds lacks long range atomic order that is found in crystalline structures. The long range order of the highly crystallized compounds could be beneficial for ion diffusion process, where the possible collisions with host atoms can be minimized with their defined channels.[60] However, the lack of flexibility of the rigid crystal framework towards a possible lattice expansion could cause irreversible structural deformation upon the insertion of ions, negatively affecting the cycling stability.[60, 111, 112] In amorphous compounds, on the other hand, the loosely packed atomic arrangement provides an open lattice space as well as better accommodation of strain that could result from lattice expansion. Therefore, amorphous structures can allow more freedom in the ion diffusion process.[111, 112] Furthermore, the amorphous structures generally offer more interfaces and grain boundaries due to their smaller grain size by which higher capacities can be

achieved. As a result, amorphous structures are commonly found in energy storage applications, and merit further investigation.

Due to the aforementioned merits of amorphous compounds, investigating the electrochemical properties of MnO_2 in amorphous phase has been the subject of extensive research. Xu et al. first introduced high lithium capacity in amorphous MnO_2 synthesized by sol-gel method where the micro-particles of MnO_2 exhibited initial discharge capacity of 436 $mAhg^{-1}$.[111] However, due to the limited ion diffusion kinetics in the large particles, relatively low rate capabilities were observed for the amorphous MnO_2 electrodes.

As discussed in Chapter 2, nanostructured electrodes offer significantly enhanced rate capability owing to their short ionic diffusion path lengths compared to their bulk counterpart, which would help overcome the rate limitation observed in amorphous MnO_2. The following section discusses how an amorphous nanowire array of MnO_2 demonstrates abnormally high lithium capacity as well as structural reversibility.

3.3 Charge Storage Mechanism of MnO_2 in Li^+ ion Based System: Anomalous and Reversible Lithium Insertion Capacity in Amorphous MnO_2 Nanowires

It is crucial to develop and demonstrate an electrode material system that could provide excellent electrochemical performance; however, a goal which must be grounded in is an understanding of the charge storage mechanism. In that context, the charge storage mechanism of MnO_2 has been widely studied both in pseudocapacitor

and battery applications.

One of the widely accepted mechanisms for the charge storage behavior of MnO_2 in an aqueous electrolyte is based on the insertion or deinsertion of protons (H^+) or Li^+ upon reduction or oxidation, respectively, where a redox reaction from Mn^{4+} to Mn^{3+} is involved to balance the charge:[113]

$$MnO_2 + xH^+ + yC^+ + (x+y)e^- \leftrightarrow MnOOH_xC_y \qquad \text{(Eqn. 3.1)}$$

Although these suggested mechanisms are most widely received as the MnO_2 charge storage process in an aqueous electrolyte, there has been much argument as to whether the mechanism is dominated by the insertion of protons or the insertion of electrolyte cations. For example, Xu et al.[114] studied the effects of protons by controlling the pH value of electrolytes. They observed a constant capacitance between pH values of 4 and 7, and even lower capacitance when pH was decreased to 3 from which the authors concluded that the MnO_2 charge storage process does not involve proton insertion. On the other hand, electrochemical quartz crystal microbalance (EQCM) studies by Kuo et al. have shown that H_3O^+ plays the predominant role in the charge storage of MnO_2 based on the measurement of mass change resulting from the insertion of cations during the discharging process where it was observed that the mass change mostly corresponds to the weight of H_3O^+. [115] These conflicting observations require more direct measurements to further understand the behavior of MnO_2.

To provide clear answer to the ambiguity of the charge storage mechanism of MnO_2 involving Li^+ ions both in aqueous and organic electrolytes, a systematic

elemental analysis of MnO_2 electrodes at various charged state in both aqueous and organic electrolytes was demonstrated and presented herein. For the elemental analysis, ICP-AES was utilized to quantify the amount of inserted and adsorbed Li^+ into MnO_2 electrodes during the charge and discharge process. ICP-AES was chosen as a mean for the elemental analysis because of its high selectivity and sensitivity with detection limits in μg/L (ppb) range.

A well-ordered nanowire array of MnO_2 electrochemically grown in AAO template was used for the study. It is worth emphasizing that an extra precision in elemental analysis can be achieved through the unique configuration of our MnO_2 nanowire array grown directly on the current collector via electrodeposition, in comparison to the composite electrode where conductive additives and polymeric binder can interfere with the analysis.

3.3.1 Experimental

Synthesis of MnO_2 Nanowire Arrays

A commercial AAO template (Whatman™ Anodisck™ Filter Membranes) was used to synthesize freestanding MnO_2 nanowire arrays. A thin gold layer (~300 nm) was sputtered on the branched side of AAO by using a Denton Desk III system as the current collector. A working electrode was assembled by attaching a copper tape on the gold sputtered side of AAO which was then sealed between the layers of Parafilm or Teflon with a defined surface window of 0.32 cm^2 (pore side open) as shown in Figure 2.6. The working electrode was then placed in a solution of 0.1 M manganese acetate and soaked until the pores are filled with the solution. Using a

three-electrode set up (counter electrode: Pt foil and reference electrode: Ag/AgCl), MnO_2 was electrodeposited by applying a constant potential of 0.6 V vs. Ag/AgCl until 150 mC of charge was passed. The electrode was then placed in 3 M of sodium hydroxide solution to remove the AAO and obtain freestanding MnO_2 nanowires.

Electrochemical Measurements

0.1 M of $LiClO_4$ in water and 0.1 M of $LiClO_4$ in acetonitrile were prepared for the investigation of charge storage behavior of MnO_2 in aqueous and organic electrolytes, respectively. The freestanding MnO_2 nanowires were washed and soaked with the electrolyte to be tested in prior to the cycling. The electrode was electrochemically charged and discharged using both galvanostatic (GV) and holding potential techniques. For GV, a constant current density of 1 A/g was applied between 0 to 1 V vs. Ag/AgCl. For holding potential experiments, the electrode was held at a constant potential for 15 minutes. The cycled electrodes were thoroughly washed with the testing solvents prior to ICP-AES analysis.

ICP-AES

The magnitude of Li^+ insertion into an amorphous MnO_2 nanowire array was monitored using a PerkinElmer ICP-Optima 4300. The wavelengths selected for Li and Mn detection were 670.8 nm and 257.6 nm, respectively. Standard solutions were prepared by the dilution of commercial standards (purchased from Sigma Aldrich) to generate calibration curves. The thoroughly washed MnO_2 electrodes at various charged states were dissolved in aqua regia (3:1 HCl: HNO_3) and diluted to a known volume before introduction into the spectrometer.

Raman Spectroscopy

Raman measurements were performed on electrodes held at different potentials in 0.1 M of $LiClO_4$ in acetonitrile. A Horiba Jobin-Yvon LabRAM HR-VIS micro Raman system was used to characterize these manganese oxide materials. The green line (514.5 nm) of an argon laser is utilized to excite the sample using a spot size of ~1 μm^2. The spectrum is taken between the Raman shifts of 300 and 900 cm^{-1}.

3.3.2 Results and Discussion

The electrodeposited MnO_2 in AAO template resulted in an array of well-ordered freestanding MnO_2 nanowires (~ 4.5 μm in length and 200 nm in diameter) as shown in the SEM and TEM images (Fig. 3.2a and 3.2b). The high-resolution TEM image in Figure 3.2c shows low crystallinity of the as-prepared MnO_2 with very small crystal domains that is consistent with a mostly amorphous phase.

MnO_2 electrodes were Galvanosatically tested in an aqueous electrolyte. The

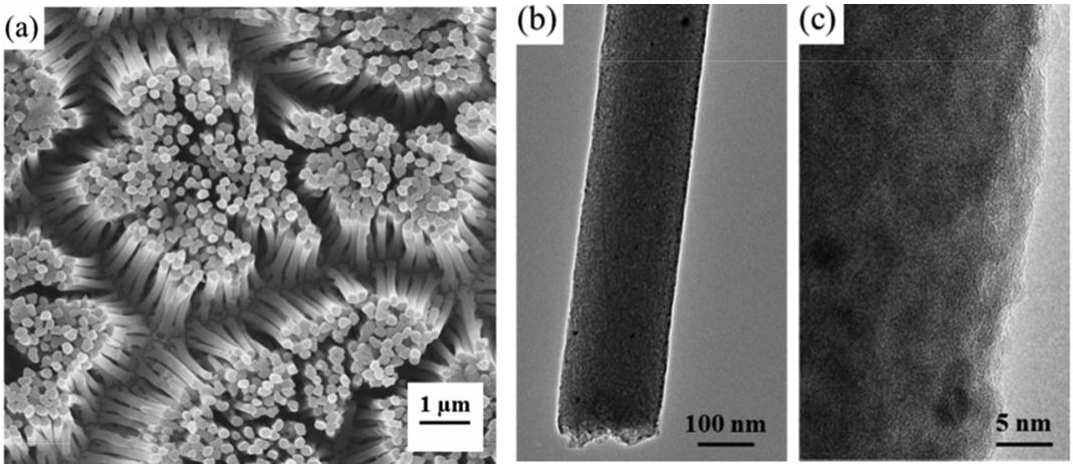

Figure 3.2 (a) SEM image of MnO_2 nanowire array, (b) TEM image of MnO_2 nanowire, and (C) high-resolution TEM image revealing low crystallinity of as-prepared MnO_2

measured and calculated amount of Li with respect to Mn (Li:Mn ratio) of MnO_2 electrodes at different charged states are shown in Figure 3.3a. It was found that as MnO_2 is discharged (below 0.2 V vs. Ag/AgCl), there exists a discrepancy between the Li:Mn ratio monitored by the elemental analysis (blue square) and that of the calculated values determined by the charge passed during discharging (black square). The additional amount of charge causing the observed discrepancy can be attributed to the contribution of proton insertion, indicating that both Li^+ ions and protons play role in the charge storage process of MnO_2 in aqueous electrolytes.

The contribution of proton insertion in an aqueous electrolyte was further supported by pH studies, where a lower amount of charge was observed at higher pH

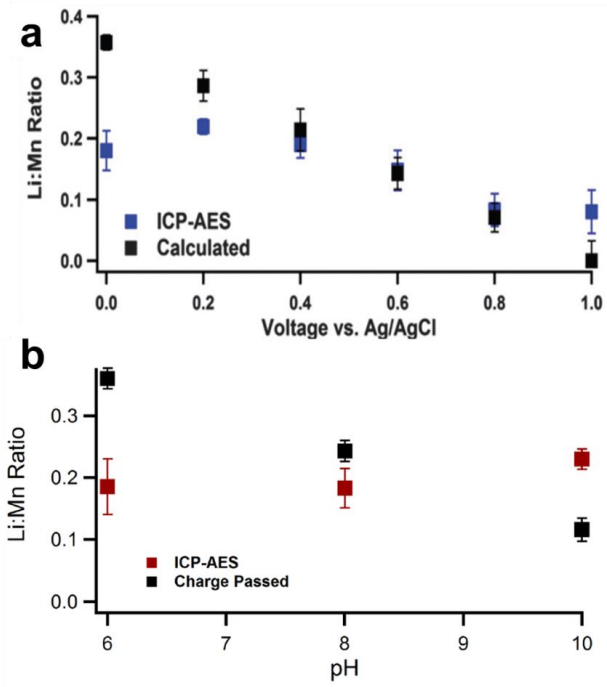

Figure 3.3 (a) Li:Mn ratios determined by ICP-AES and calculated based on the total amount of charge passed during the electrochemical discharge measured in aqueous electrolytes of (a) 0.1 M $LiClO_4$ in water (b) $LiClO_4$ in water at three different pH controlled by LiOH (the total Li concentration was adjusted to be constant at 0.1 M).

with statistically no change in lithium insertion, thus indicating that decreasing the proton concentration results in a lower capacitance (Fig 3.3b).

In an organic electrolyte system, the Li:Mn ratio obtained by the elemental analysis (Fi. 3.4) matches well with the calculated value, where it was found that more than 1.5 mol of Li per Mn can be incorporated upon the discharge corresponding to a capacity of 463 $mAhg^{-1}$. This value exceeds the traditionally accepted theoretical capacity of MnO_2 (308 $mAhg^{-1}$) for the reduction of Mn^{4+} to Mn^{3+} with incorporation of 1 mol of Li per Mn. These results indicate a fairly significant difference in the mechanism of charge storage in MnO_2 in the absence of protons when compared to the aqueous systems, highlighting the importance of both electrode and electrolyte on charge storage reactions.

Further, the lithium insertion process was found to be reversible where most of the inserted Li^+ ions were retracted upon charging with no significant structural deformation observed in the time scale of the experiment as can be seen from the

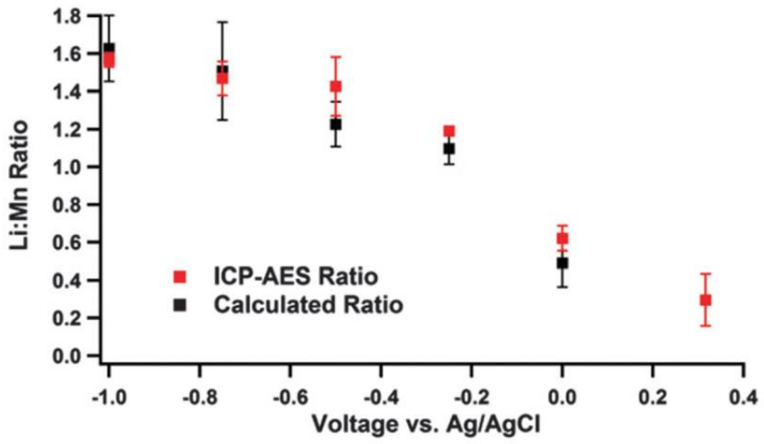

Figure 3.4 Li:Mn ratios determined by ICP-AES and calculated based on the total amount of charge passed during the electrochemical discharge measured in organic electrolytes (0.1 M $LiClO_4$ in acetonitrile).

TEM image (Fig. 3.5a). The structural variation and reversibility during the charge and discharge process were studied by Raman spectra (Fig. 3.5b) of MnO_2 nanowire electrode at different charge states. In Figure 3.5b, the Raman peak at 575 cm^{-1} responsible for Mn–O stretching in the basal plane is suppressed and shifts to higher wavenumbers upon lithiation. This shift corresponds to the reduction of Mn^{4+} to lower oxidation states causing shorter Mn–O bond lengths and thus higher frequency bond stretches.[58] However, this peak shifts back and re-intensifies after delithiation, thus showing great structural reversibility. This confirms the observations by TEM which suggest that this reaction is highly reversible, despite the unusually high degree of lithium insertion. The observed high lithium capacity and reversibility is largely attributed to the amorphous nature of as-prepared MnO_2 and its nanostructure, where Mn could reversibly undergo further reduction from Mn^{4+} to Mn^{2+}, increasing the reversible capacity beyond the theoretical one electron per unit cell capability (Mn^{4+} to Mn^{3+}).

3.4 Conclusions

A solid understanding of the charge storage mechanism and the electrochemical properties of an electrode material is a critical step to identifying the challenges and overcoming any existing limitations. A systematic investigation of an amorphous and nanostructured MnO_2 electrode indicates that its charge storage mechanism in lithium containing aqueous electrolyte involves both the lithium insertion and proton insertion. In addition, a reversible and anomalous lithium capacity was observed in organic electrolyte system where more than one lithium

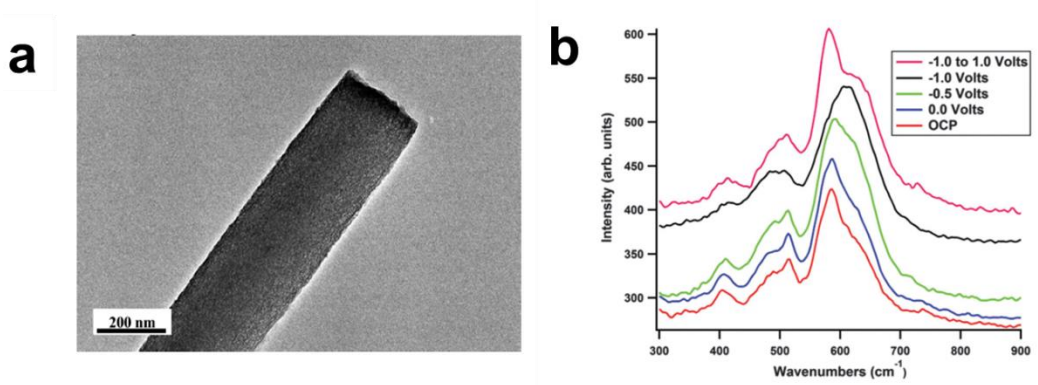

Figure 3.5 (a) TEM image of MnO_2 nanowire after discharging at -1.0 V vs. Ag/AgCl, (b) Raman spectra of MnO_2 nanowire arrays at various charged state in 0.1 M $LiClO_4$ in acetonitrile.

insertion per formula unit was promoted owing to the amorphous nature and high surface area of nanowire structured MnO_2.

However, unlike the observed high Li^+ ion capacity in MnO_2, the reported Mg^{2+} insertion capacity in MnO_2 has been significantly less than that of Li^+ capacity at a similar rate. While the stronger electrostatic interaction that the divalent Mg^{2+} ions bring in to the system is believed to be the main factor for the poor insertion kinetics of Mg^{2+}, the following chapters present studies which investigate the origin of the poor Mg^{2+} insertion kinetics and discuss how the kinetic limitation can be overcome to achieve high Mg^{2+} ion capacity in MnO_2.

Chapter 4 Activation of MnO_2 Cathode by Water-Stimulated Mg^{2+} Insertion for Magnesium Ion Battery

Portions of this chapter have been published in Song et al., "Activation of MnO_2 Cathode by Water-stimulated Mg^{2+} Insertion for Magnesium Ion Battery", Phys. Chem. Phys. Chem. ***2015****, 17, 5256.*

4.1 Introduction

As discussed in the previous chapters, one of the major challenges for Mg batteries comes from the slow solid-state kinetics of Mg^{2+} ions in most of the common transition metal compound cathode materials. This sluggish kinetics of Mg^{2+} compared to Li^+ is mostly attributed to the stronger electrostatic interaction between the divalent Mg^{2+} ions and the host material, which often results in low or even no Mg^{2+} insertion in many cathodes.[31, 33] The electrostatic interaction that Mg^{2+} ions may experience includes repulsion between the charges of Mg^{2+} ions and positive charges within the transition metal compounds. Additionally, it is possible that surface adsorbed Mg^{2+} ions lead to surface charge inversion, creating a positively charged surface, which may push away further access of Mg^{2+} ions to the surface of the host material from the bulk electrolyte.[116]

In the search for a suitable cathode with a reasonable Mg^{2+} ion mobility, two main strategies have been utilized previously. The first is to use nanostructures to facilitate the Mg^{2+} insertion/deinsertion and overcome the kinetic barrier by reducing the ionic diffusion path within the cathode

material.[117-119] The second strategy, which was demonstrated in layer structured V_2O_5, is to introduce a small amount of strong dipole molecules, such as water, into the organic electrolytes where the water molecules presumably "shield" the charges of divalent Mg^{2+} ions and reduce the electrostatic interaction between the concentrated charges.[37, 120]

Various cathode materials have been screened and studied for Mg^{2+} insertion, including Chevrel phases (e.g. Mo_6S_8)[1, 34, 35, 121-123], V_2O_5,[124-127] TiS_2,[117] and WSe_2.[119] In separate research efforts, manganese dioxide (MnO_2) has been tested as a possible candidate for a Mg battery cathode material.[128-132]

MnO_2 has recently received much attention as one of the strong candidates for Mg^{2+} hosting compound for an Mg battery application. Successful demonstration of MnO_2 for Mg^{2+} hosting compound will provide high operating voltage (~ 3.2 V vs. Mg) compared to the well-studied Chevrel phase Mg cathode whose operating voltage is less than 1.5 V vs. Mg. Therefore, an Mg battery with MnO_2 cathode will be able to increase the energy density of the device by more than a factor of two with a similar capacity than that with Chevrel phase cathodes. Furthermore, the combination of Mg and MnO_2, both of which are low cost materials and relatively safer to the environment, satisfies the requirements for a next generation battery technology.

However, unlike its great electrochemical performances in Li^+ ion environment, MnO_2 has exhibited rather poor Mg^{2+} ion capacity and reversibility, which is mostly attributed to the aforementioned strong ionic interaction between

Mg^{2+} ions and MnO_2 during the insertion process. For example, Kumagai et *al*. first examined Mg^{2+} ion insertion in Todorokite-MnO_2 (3×3 tunnel structure) where only one discharge cycle with 85 $mAhg^{-1}$ that corresponds to 0.3 Mg^{2+} per Mn was achieved at a very low current density.[133] This is contrary to the demonstrated capacity of 220 $mAhg^{-1}$ and over 20 stable cycles in Li^+ electrolytes in the same study with the same electrode system. Rasul et *al*, investigated various crystallographic structures of MnO_2 (α-, β-, and δ-MnO_2) and studied their effect on the Mg^{2+} insertion capacity. However, very poor electrochemical behaviors were observed in all structures, where nearly 100 % of its initial capacity disappeared after 20 cycles with poor Mg^{2+} insertion kinetics.[130-132]

In this study, a combination of the two aforementioned strategies is utilized for the investigation of Mg battery cathode materials by synthesizing a nanostructured MnO_2 cathode and testing the performance of this material in conventional electrolytes containing water as a minor additive. The electrochemical insertion/deinsertion behaviors of Mg^{2+} ions into/from MnO_2 nanowire electrodes are demonstrated and the potential of MnO_2 as a host material for the Mg-ion is explored.

It is demonstrated in this study that the insertion/deinsertion of Mg^{2+} ions into MnO_2 is greatly enhanced by the presence of water molecules in the conventional electrolyte whereas no significant Mg^{2+} insertion/deinsertion activities were observed in a dry magnesium electrolyte. We also show that utilizing both water molecules in the electrolyte and nanostructured MnO_2 results in a synergic effect on Mg^{2+} insertion/deinsertion into MnO_2, delivering improved Mg^{2+} insertion capacity and

enhanced cyclability. Furthermore, it is demonstrated that a sufficient electrochemical reaction in the water-containing electrolyte stimulates the insertion of Mg^{2+} ions in MnO_2, such that improved Mg^{2+} insertion/deinsertion capacities are observed even when the water molecules are no longer present in the electrolyte.

4.2 Experiment

4.2.1 Synthesis of Free Standing MnO_2 Nanowire/Film Electrode

In order to prepare the working electrode for MnO_2 electrodeposition, 300 nm thick gold was sputtered on the branched side of an anodized aluminum oxide (AAO) membrane as a current collector using a Denton Desk III sputter coater. A strip of copper tape was attached to the gold side of the membrane for electrical contact. Then the AAO piece with copper tape was sandwiched between layers of Parafilm which had a 0.32 cm^2 hole on one side. For the nanowire MnO_2 synthesis, the side of AAO without the gold layer was exposed to the electrolyte, while the film structured MnO_2 the gold side of AAO was exposed. This Parafilm sandwiched composite was then heated carefully for a good seal to make the working electrode for MnO_2 deposition. The MnO_2 electrode was synthesized by anodic electrodeposition in a 100 mM manganese acetate solution using Ag/AgCl and platinum as reference and counter electrodes, respectively. A constant voltage of 0.6 V vs. Ag/AgCl was applied to the working electrode until the total accumulated charge has reached 150 mC. This composite was then placed in a 3 M of sodium hydroxide solution for 15 minutes to dissolve AAO membrane which resulted in a free standing and vertically aligned MnO_2 nanowire (or planar film; ~2 μm thickness) electrode with a gold current

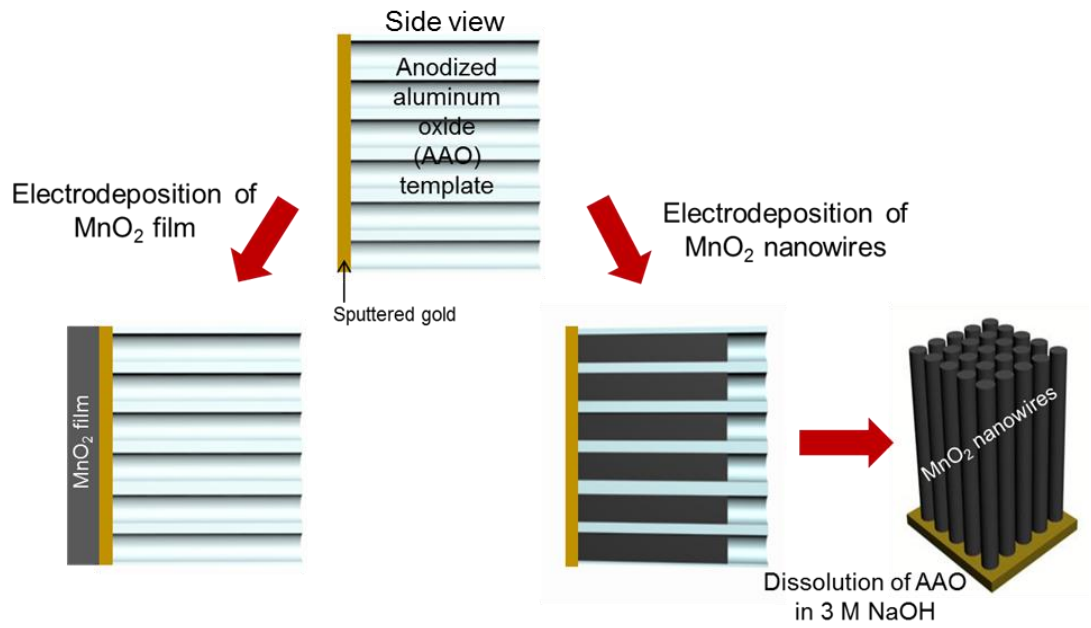

Figure 4.1 Schematic of electrodeposition of MnO_2 process. AAO template was used as substrate/template for both film and nanowire structured MnO_2.

collector. A schematic of the MnO_2 synthesis process is shown in Figure 4.1.

4.2.2 Inductively Coupled Plasma-Atomic Emission Spectroscopy (ICP-AES)

For an ICP-AES analysis, electrodes were completely dissolved in a 3:1 HCl: HNO_3 solution. A PerkinElmer ICP-optima 4300 was used. Standard solutions (Mn and Mg traceable to the National Institute of Standards and Technology) were prepared and analyzed to generate the calibration curves.

4.2.3 Raman Spectroscopy

Raman measurements were performed on MnO_2 electrodes which were stopped at various potentials during cyclic voltammogram measurements in 0.1 M $Mg(ClO_4)_2 \cdot 6H_2O$ / PC using Horiba Jobin-Yvon LabRAM HR-VIS microRaman

system. The green line (514.5 nm) of an argon laser and a spot size of ≈1 μm^2 were utilized (measured between 300 and 900 cm^{-1}).

4.2.4 X-ray Photoelectron Spectroscopy (XPS)

An XPS analysis was performed by using a Kratos AXIS 165 spectrometer. All peaks were calibrated to the hydrocarbon peak at 284.8 eV. Then the curves were fitted using CasaXPS software.

4.2.5 Electrochemical Measurement

MnO_2 electrodes were thoroughly washed with DI water and pure propylene carbonate for several times before an electrochemical analysis. Most electrochemical measurements were done using three electrodes set up (Ag/AgCl reference electrode and platinum foil as counter electrolyte) unless otherwise stated.

4.2.6 Electrolyte Preparation

The amount of water in the electrolyte was adjusted by tuning the concentration of hexahydrated magnesium perchlorate salt in propylene carbonate (PC). The list of electrolytes with different H_2O to Mg^{2+} ratios is shown in Table 4.1. The water concentration of each electrolyte was measured by Metrohm Karl-Fisher 899 Coulometer, which demonstrated that the water amounts adjusted by hydrated salt are very close to the expected values.

4.2.7 Electrochemical Quartz Crystal Microbalance Measurement

QCM200 (Stanford Research Systems) and 5 MHz quartz crystal with 1 inch diameter were utilized for the *in situ* measurement of the MnO_2 mass change during

the electrochemical reaction. Clean quartz crystal was first calibrated using a Cu plating/stripping calibration method[134] as well as MnO_2 film deposition. 50 mC of MnO_2 was deposited on the gold surface of quartz crystal (5.067 cm^2) to obtain a thin and uniform MnO_2 film. Then the MnO_2 deposited quartz crystal electrodes were transferred to Mg electrolytes where CV and frequency change were measured simultaneously.

4.3 Results and Discussion

4.3.1 Synthesis and Characterization of Free- Standing MnO_2 Nanowires

MnO_2 nanowire electrodes were synthesized via anodic electrochemical deposition, where MnO_2 was directly grown into the cylindrical nanopore arrays of an anodized aluminum oxide (AAO) membrane using sputtered gold as a current collector. Scanning electron microscope (SEM) and transmission electron microscope (TEM) images of the as-prepared nanowire array are shown in Figure 4.2. The cathode is composed of free-standing MnO_2 nanowires with diameters of ~200 nm and lengths of ~4.5 μm. A high-resolution TEM image (Fig. 4.2d) reveals the highly porous and amorphous nature of these MnO_2 nanowires. A Raman spectroscopy spectrum (Fig. 4.3) shows two distinct peaks at 577 and 635 cm^{-1} corresponding to the Mn-O stretching in basal plane of MnO_2 and the symmetric stretching vibration of Mn-O in MnO_6 groups, respectively.[59, 101] However, XRD shows no crystalline peak indicating a pseudo-amorphous nature of the MnO_2 nanowires possibly because of very small crystalline domains.[59]

Table 4.1 List of electrolytes used in this work. Water concentration was confirmed by Karl-

Fisher Coulometer.

Electrolyte	**H_2O/Mg^{2+} Ratio**
i) 0.1 M Mg^{2+} / no water (i.e. 0.1 M $Mg(ClO_4)_2$ Anhydrous)	**0** (= 0/0.1)
ii) 0.5 M Mg^{2+} / 0.6 M H_2O (i.e. 0.1 M $Mg(ClO_4)_2 \cdot 6H_2O$ + 0.4 M $Mg(ClO_4)_2$ Anhydrous)	**1.2** (= 0.6/0.5)
iii) 0.2 M Mg^{2+} / 0.6 M H_2O (i.e. 0.1 M $Mg(ClO_4)_2 \cdot 6H_2O$ + 0.1 M $Mg(ClO_4)_2$ Anhydrous)	**3** (= 0.6/0.2)
iv) 0.1 M Mg^{2+} / 0.6 M H_2O (i.e. 0.1 M $Mg(ClO_4)_2 \cdot 6H_2O$)	**6** (= 0.6/0.1)
v) 0.1 M Mg^{2+} / 1.2 M H_2O (i.e. 0.1 M $Mg(ClO_4)_2 \cdot 6H_2O$ + 0.6 M H_2O)	**12** (= 1.2/0.1)

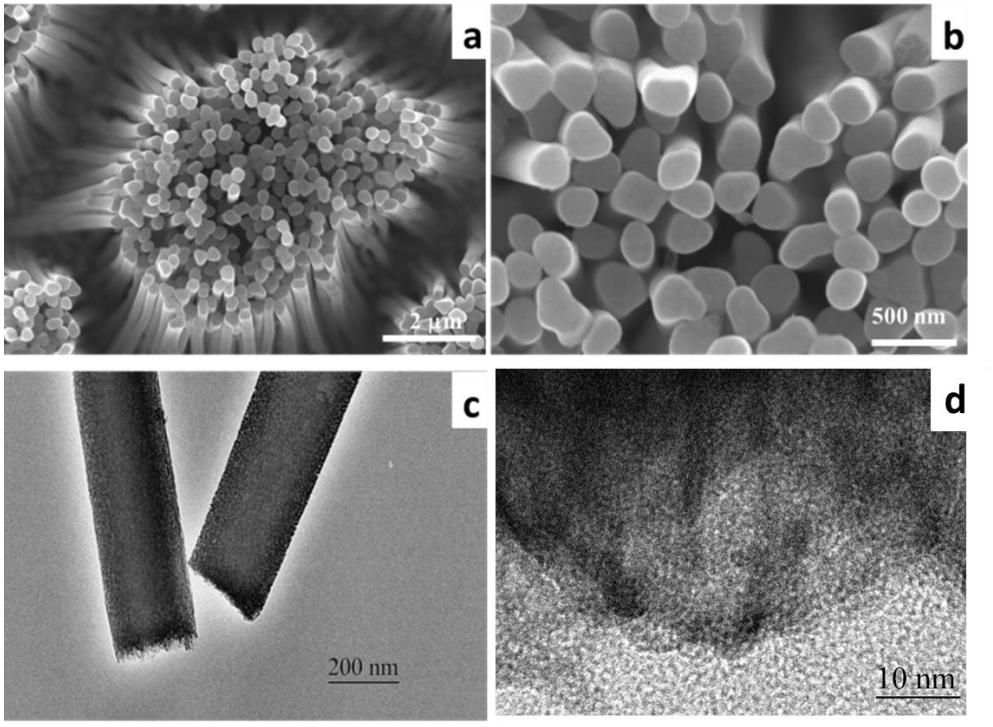

Figure 4.2 a) & b) SEM, c) TEM image and d) high-resolution TEM image of as-prepared of MnO_2 nanowire electrode.

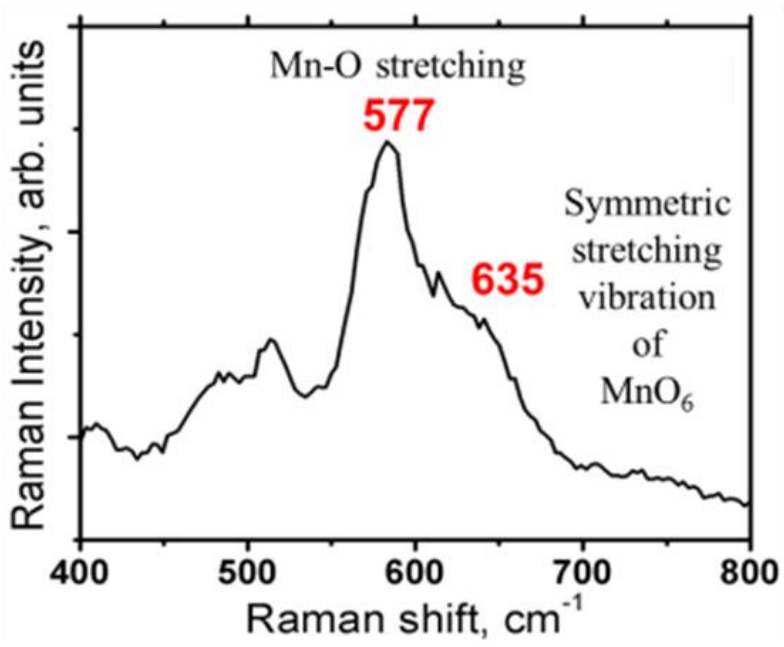

Figure 4.3 Raman spectrum of as-prepared MnO_2 nanowire electrode

4.3.2 Improved Mg^{2+} Insertion/Deinsertion Capacities in Water-containing Electrolytes

The cyclic voltammetry (CV) response of the MnO_2 in Mg^{2+} electrolyte was tested in a three-electrode system using a platinum foil as the counter electrode and a saturated Ag/AgCl as the reference electrode. In order to assess the shielding of Mg^{2+} ions by water molecules and its effect on the insertion/deinsertion behavior of Mg^{2+} into the hosting MnO_2 nanowire cathode, the ratio between H_2O molecules and Mg^{2+} in propylene carbonate (PC) was tuned as follows: i) 0.1 M anhydrous $Mg(ClO_4)_2$, ii) 0.1 M $Mg(ClO_4)_2 \cdot 6H_2O$ + 0.4 M anhydrous $Mg(ClO_4)_2$, iii) 0.1 M $Mg(ClO_4)_2 \cdot 6H_2O$ + 0.1 M anhydrous $Mg(ClO_4)_2$, and iv) 0.1 M $Mg(ClO_4)_2 \cdot 6H_2O$. The list of electrolytes and water to Mg^{2+} concentration ratio are shown in Table 4.1. Note that for the electrolytes i) to iv), the ratio between H_2O molecules and Mg^{2+} was controlled by adjusting the concentrations of $Mg(ClO_4)_2$ while maintaining the absolute amount of water constant. The CV curves of the MnO_2 nanowire in these electrolytes are shown in Figure 4.4a. As clearly demonstrated, the presence of water molecule has a determinant effect on the cathodic and anodic currents in the voltammograms. In electrolyte containing no water, no redox peaks are observed, and the capacity calculated from this curve is low, implying that there is negligible Mg^{2+} insertion in the absence of water in the electrolyte. This also indicates that the structrual water molecules which could possibly exist in the electrodeposited MnO_2 (as-prepared) do not affect the insertion behavior of Mg^{2+} ions. As the ratio between water molecules and Mg^{2+} ions in the electrolyte was increased, two redox peaks at around 0.1 V and 0.9 V vs. Ag/AgCl are observed. Interestingly, when the ratio of H_2O to Mg^{2+} is

increased to 3:1, a further increase in the redox peak intensity and the capacity are obtained. This suggests that an increased ratio of water molecules to Mg^{2+} ions in the electrolyte will have a significant positive effect even with decreased $Mg(ClO_4)_2$ concentration in the electrolyte. The highest capacity and redox peak intensity were observed in the CV curve measured in electrolyte with $6H_2O/Mg^{2+}$ ratio among the electrolytes of i) to iv). These observations from the CV that increasing the $Mg(ClO_4)_2$ concentration does not result in higher Mg^{2+} insertion degree, but it is the ratio between water and Mg^{2+} ion that plays a significant factor in the insertion/deinsertion behaviors of Mg^{2+} ions.

In order to directly measure the amount of inserted Mg^{2+} ions into the cathode, ICP-AES was used. The amount of inserted Mg with respect to Mn (Mg/Mn) in the MnO_2 nanowire electrodes was determined after the electrodes were discharged at a constant potential of -0.4 V vs. Ag/AgCl for 15 minutes in the electrolytes with various H_2O/Mg^{2+} ratios. As it is clearly demonstrated in Figure 4.4b, the Mg fraction highly depends on the H_2O/Mg^{2+} ratio, which further supports the observed trend in CV curves. Note that in the electrolyte with $6H_2O/Mg^{2+}$ ratio, the Mg fraction value (Mg/Mn=0.69) exceeds 0.5, which is an expected value for the reduction of one Mn^{4+} to Mn^{3+}. Thus, we suggest that part of Mn^{3+} was further reduced to Mn^{2+} by the excess 0.19 of Mg/Mn. As the H_2O/Mg^{2+} ratio is further increased to 12, the inserted amount of Mg^{2+} ions is decreased, implying the electrolyte with $6H_2O/Mg^{2+}$ ratio is close to the optimum condition for Mg^{2+} insertion into MnO_2 nanowire electrode.

The Mg/Mn ratio values determined by ICP-AES are in a very good agreement with the calculated value of Mg amount based on the total charge passed during the electrochemical reaction (Fig. 4.4b). These results support that the full amount of Mg detected by ICP-AES can be considered as electrochemically inserted

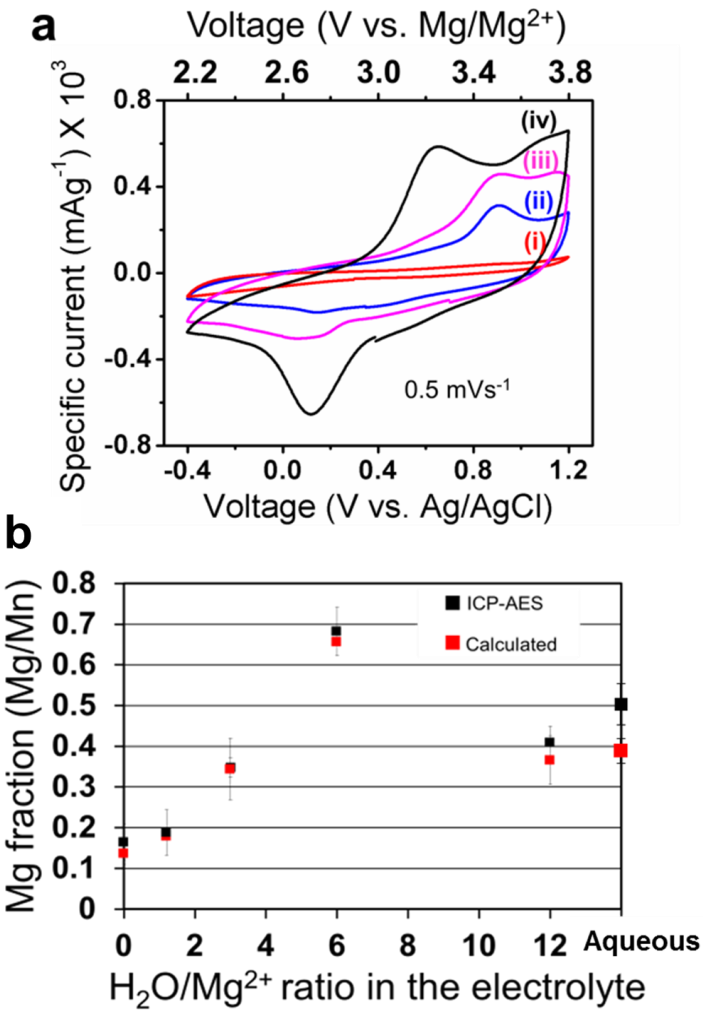

Figure 4.4 (a) Cyclic voltammograms of MnO_2 nanowire electrodes in electrolytes with various water to Mg^{2+} ion ratios. i) 0.1 M anhydrous $Mg(ClO_4)_2$, ii) 0.1 M $Mg(ClO_4)_2 \cdot 6H_2O$ + 0.4 M anhydrous $Mg(ClO_4)_2$, iii) 0.1 M $Mg(ClO_4)_2 \cdot 6H_2O$ + 0.1 M anhydrous $Mg(ClO_4)_2$, and iv) 0.1 M $Mg(ClO_4)_2 \cdot 6H_2O$. Scan rate of 0.5 mVs^{-1} was used. (b) ICP-AES Mg:Mn ratios of MnO_2 nanowire electrodes discharged at -0.4 V vs. Ag/AgCl for 15 minutes in electrolytes with various H_2O/Mg^{2+} ratios and expected Mg:Mn ratios which were calculated based on the total accumulated charges. Error bars indicate 95% confidence intervals.

Mg^{2+} ions. It was shown in Chapter 3 that the cation insertion mechanism into MnO_2 nanowire electrode in aqueous lithium electrolyte is mainly governed by the proton insertion rather than lithium ion insertion.[135] However, the observed agreement of ICP-AES determined Mg/Mn values with the calculated Mg/Mn values based on the total charge passed during the electrochemical reaction indicates that there is a negligible contribution from proton insertions in Mg electrolyte system. In a complete aqueous Mg electrolyte, similar degree of Mg fraction to that of 12 H_2O/Mg^{2+} ratio is observed (Fig. 4.4b). However, in the complete aqueous electrolyte, there is an increased discrepancy between the ICP-AES determined and calculated Mg fraction values (Δ~0.1). The additional Mg detected by ICP-AES measurement is believed to be due to side reactions involving water molecules (e.g., precipitated $Mg(OH)_2$) that could have occurred during the discharge process. The CV measured in aqueous $Mg(ClO_4)_2$ electrolyte shows

Ex situ Raman spectra of MnO_2 nanowire electrodes cycled in 0.1 M $Mg(ClO_4)_2 \cdot 6H_2O$/PC (Fig. 4.5a) were collected to further monitor the structural changes upon the Mg^{2+} insertion/deinsertion process. After a cathodic potential sweep to -0.4 V, the peaks at 575 cm^{-1} and 635 cm^{-1} diminished and a broad peak centered at 604 cm^{-1} was appeared. We attribute the band broadening along with the peak shift to the reduction of Mn^{4+} to a lower oxidation state upon the insertion of Mg^{2+}.[58] The two peaks at 575 cm^{-1} and 635 cm^{-1} reappeared after the anodic potential sweep to 1.2 V and diminished again during the cathode sweep to 0 V, thereby showing good structural reversibility.

X-ray photoelectron spectroscopy (Fig. 4.5b) also confirms the reversibility of

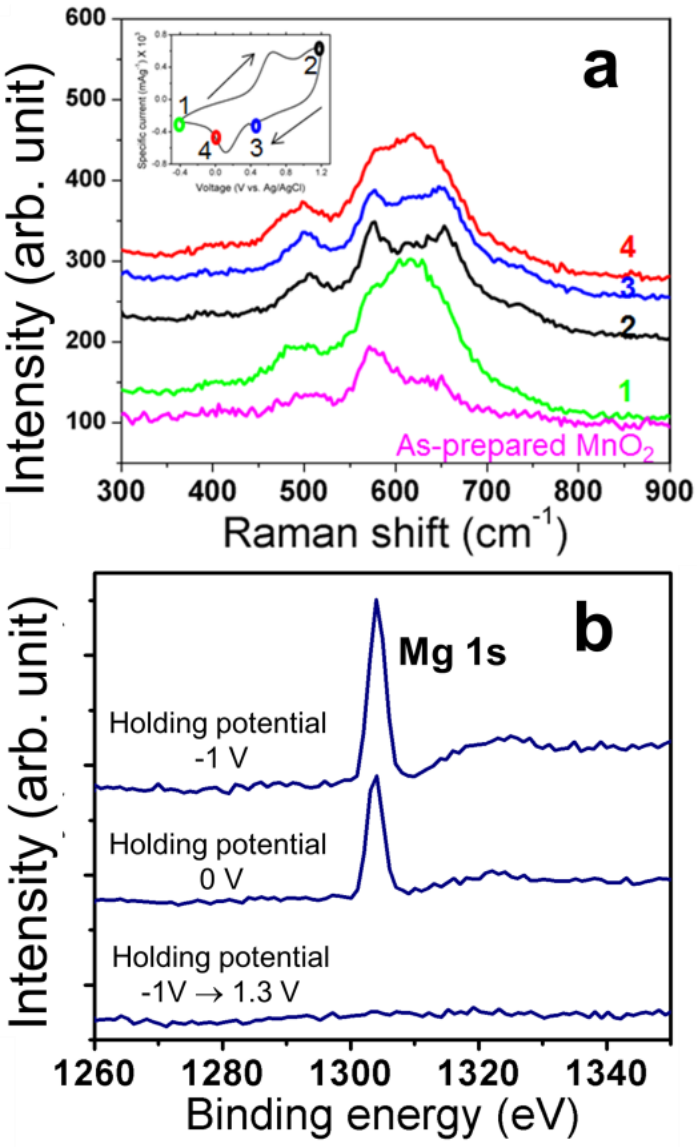

Figure 4.5 (a) *Ex-situ* Raman spectra of MnO_2 nanowire electrodes cycled in 0.1 M $Mg(ClO_4)_2 \cdot 6H_2O$/PC. (b) Mg 1s XPS spectra for MnO_2 nanowire electrode held at constant potentials for 15 minutes. All peaks were calibrated to the hydrocarbon peak at 284.8 eV.

Mg insertion process in the MnO_2 nanowire electrode where the Mg 1s peak completely disappeared after the electrode was recharged. The good

reversibility of the Mg^{2+} insertion process in the MnO_2 nanowire electrode is believed to be due to the water shielding effect which reduces the electrostatic interactions between the ions and host material[11] and enables the Mg^{2+} insertion/extraction to occur freely and reversibly. A concurrent possible explanation for the positive effect of the water molecule in Mg^{2+} insertion/deinsertion is that the presence of water impedes ion pairing between Mg^{2+} ions and counter anions[136] by forming a water solvation shell, as the interaction between the paired species can hinder the insertion/deinsertion of Mg^{2+}. Additionally, the charge transfer process in water-containing electrolyte is expected to be more efficient than in pure organic electrolyte as less desolvation energy is required for Mg^{2+} ions in an aqueous environment.[137]

In order to eliminate a possible parasitic water decomposition reaction due to the relatively large electrochemical window used in our study (i.e., -0.4 V to 1.2 V vs. Ag/AgCl), the amount of water in the electrolyte that was consumed during the electrochemical reaction was monitored using a Karl-Fisher coulometer. As shown in Figure 4.6, there were no significant changes in the water amount in the electrolyte before and after the electrochemical reaction implying that there were negligible water oxidation/reduction reactions.

4.3.3 Nanostructured vs Planar MnO_2 Electrodes

Along with the presence of water molecules in the electrolyte, the size and nanostructure of the MnO_2 cathode were found to have a significant role in

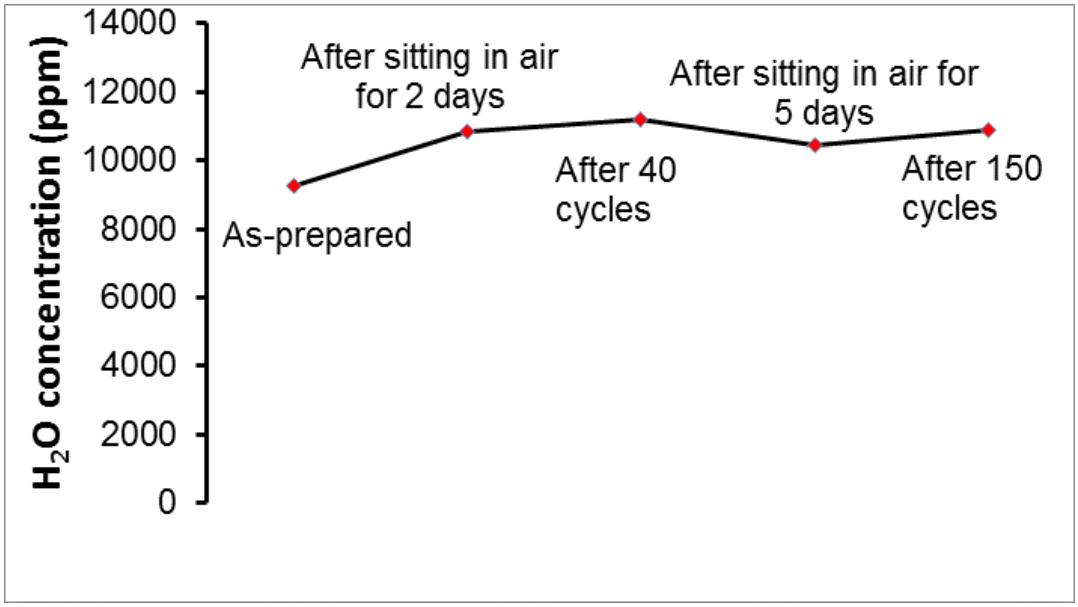

Figure 4.6 Concentration of water of 0.1 M $Mg(ClO_4)_2 \cdot 6H_2O$/PC at various states measured by Karl-Fisher Coulometer.

facilitating the Mg^{2+} insertion/deinsertion capabilities of the cathode. Figure 4.7 shows SEM images of a planar film of MnO_2 with a thickness of ~2 μm (Fig. 4.7a) and compares the cyclic voltammograms of MnO_2 nanowire and film electrodes measured in 0.1 M $Mg(ClO_4)_2 \cdot 6H_2O$/PC (Fig. 4.7b). As obtained, the MnO_2 film electrode did not exhibit considerable capacity compared to the MnO_2 nanowire electrode. The observation that the film electrode did not show significant degree of redox reaction even in water-containing electrolyte implies that the combination of water-containing electrolyte and the nano-sized electrode has a synergic effect on the Mg^{2+} insertion performances. The ICP-AES results also confirm that there is a significantly lower degree of Mg^{2+} insertion in the MnO_2 film electrode (Mg/Mn = 0.18) than in nanowire MnO_2 (Mg/Mn = 0.69). The short ionic diffusion path length accompanied by the high aspect ratio of the MnO_2 nanowire electrode resulted in

improved Mg^{2+} insertion/adsorption capabilities.[138]

The insertion of Mg^{2+} ions into MnO_2 nanowire was more closely examined by TEM analysis. Figure 4.8a shows TEM EDS elemental mapping images of Mg and Mn of a discharged MnO_2 nanowire electrode (held at -0.4 V vs. Ag/AgCl). The presence of Mg is clearly observed in the nanowire, whereas in the MnO_2 (Figure

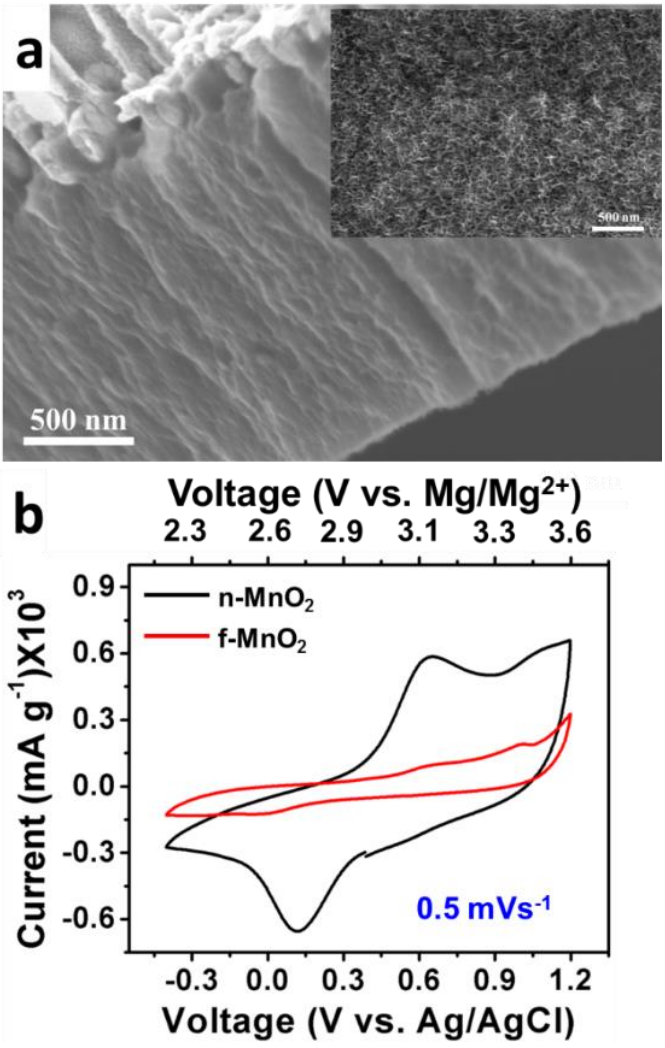

Figure 4.7 (a) SEM image (side view) of film structured MnO_2 deposited on the gold sputtered side of AAO membrane. Inset: SEM image (top view) of film structured MnO_2 surface. (b) CVs of MnO_2 nanowire electrode (n-MnO_2) and film structured MnO_2 electrode (f-MnO_2) measured in 0.1 M $Mg(ClO_4)_2 \cdot 6H_2O$/PC at a scan rate of 0.5 mVs^{-1}.

4.8b) held at 1.2 V followed by discharging at -0.4 V, almost all of the Mg^{2+} ions have been removed, further confirming the great reversibility of Mg^{2+} insertion/deinsertion process of this system.

In the discharged MnO_2, an amorphous layer is observed on its surface, which could be the result of a structural change or possible volume expansion of MnO_2 upon the insertion of Mg^{2+} ions. Another plausible explanation for the observed surface morphology change is the formation of a new phase material upon the Mg^{2+} insertion. To investigate the origin of the observed amorphous layer and higher concentration of Mg at the surface, a detailed study of MnO_2 surface chemistry during the Mg^{2+} insertion process was conducted and is discussed in Chapter 5. The distribution of magnesium within the discharged MnO_2 was further analyzed as shown in Figure 4.8c. The Mn line scan analysis trend was regarded as a uniform distribution by

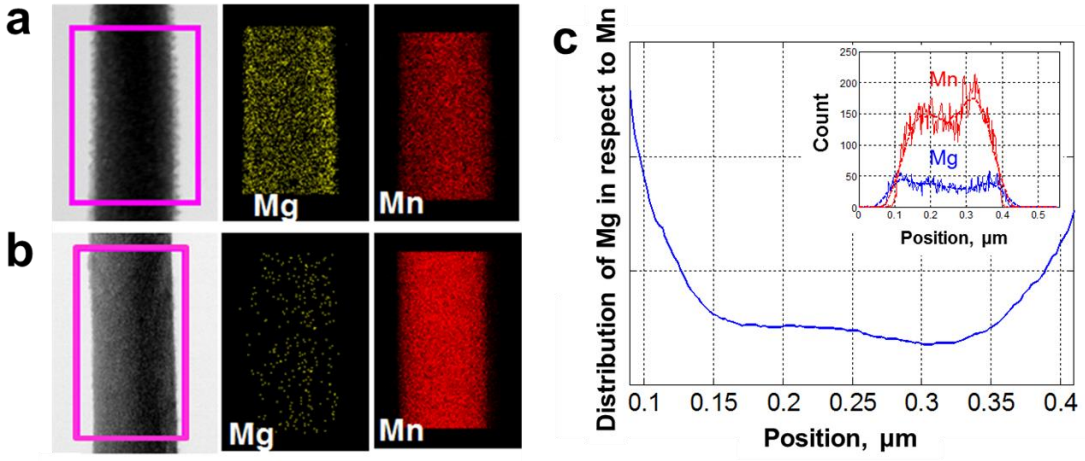

Figure 4.8 TEM EDS analysis of MnO_2 nanowire. Elemental mapping of Mg and Mn for MnO_2 nanowire (a) after discharged at -0.4 V (vs. Ag/AgCl) and (b) after recharged at 1.2 V (vs. Ag/AgCl) by holding potential experiment in the electrolyte with 6 H_2O/Mg^{2+} ratio. (c) TEM elemental line scan results (inset) and analysis result representing the aspect of Mg distribution within the discharged MnO_2 nanowire (a).

which the relative distribution of Mg with respect to Mn was analyzed. It shows that Mg is more concentrated near the surface/edge of MnO_2 nanowire rather than at the center, which implies that Mg^{2+} ions are first inserted into the outer shell of the MnO_2 when chronoamperometric measurement is applied, hence it is more concentrated near the surface/edge of MnO_2 nanowire rather than the center.

The distribution of Mg^{2+} ions inside of the discharged MnO_2 nanowires was examined by analyzing the cross section of a discharged MnO_2 nanowire electrode (middle section) prepared by microtome (Figure 4.9a). Figure 4.9b shows Mg elemental mapping analysis measured by electron energy loss spectroscopy (EELS). As demonstrated, distribution of Mg throughout the MnO_2 nanowire is observed, which proves that the Mg^{2+} insertion takes place not only at the surface of MnO_2 but also Mg^{2+} ions were able to diffuse into the bulk of the nanowire. The highly porous nature of our MnO_2 nanowire as shown in Figure 4.9c along with the small diameter

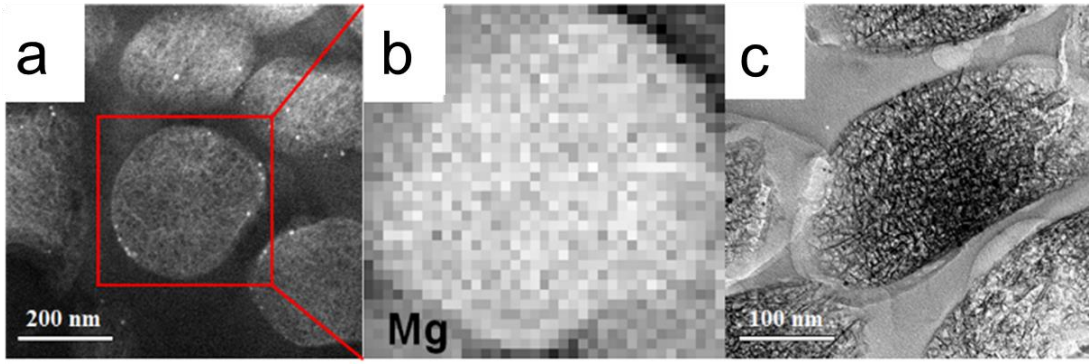

Figure 4.9 (a) TEM image of discharged MnO_2 nanowire cross-section (top view). Microtome was used to slice the free-standing MnO_2 nanowire array and prepare TEM samples. (b) Elemental Mg mapping image of microtomed MnO_2 nanowire cross-section (squared area in (a)) analyzed by EELS. (c) TEM image of thin slice of MnO_2 nanowire (cross-section) showing highly porous nature of electrodeposited MnO_2 nanowire.

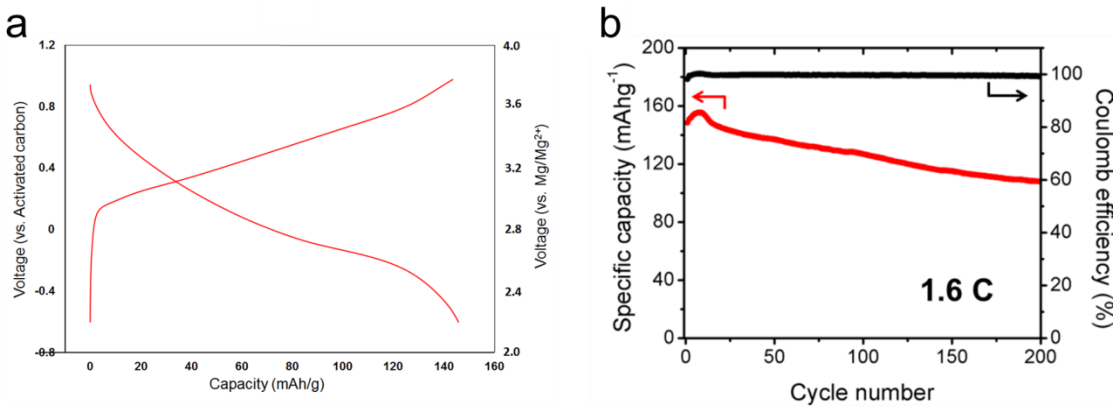

Figure 4.10 a) Galvanostatic charge and discharge curve and b) Cycling performance of MnO_2 nanowire electrode in 0.1 M $Mg(ClO_4)_2 \cdot 6H_2O$/PC electrolyte at a 1.6 C rate. Activated carbon electrode was used as both reference and counter electrode.

of the MnO_2 nanowire are believed to be the significant factors for this the bulk insertion of Mg^{2+} ions within the nanowire. However, relative concentration of Mg at near the surface is expected to be higher than that of at the inside of nanowire as shown in Figure 4.8c, although it is not very definitive from the presented EELS elemental mapping data shown in Fig. 4.9b.

The galvanostatic charge and discharge performance of MnO_2 nanowire electrodes were measured in 0.1 M $Mg(ClO_4)_2 \cdot 6H_2O$/PC using an activated carbon cloth as the reference and counter electrode (Fig. 4.10a). The mass loading of the activated carbon electrode was adjusted so that its total surface area is high enough to compensate for the charges of Mg^{2+} insertion/deinsertion reaction in MnO_2 electrode. Figure 4.10b displays the cycling performance of a MnO_2 nanowire electrode measured at a 1.6 C rate (1C=616 mAg^{-1}) where an initial capacity of ~ 160 $mAhg^{-1}$ was observed (i.e. Mg/Mn = 0.19). The specific capacity remained fairly stable and

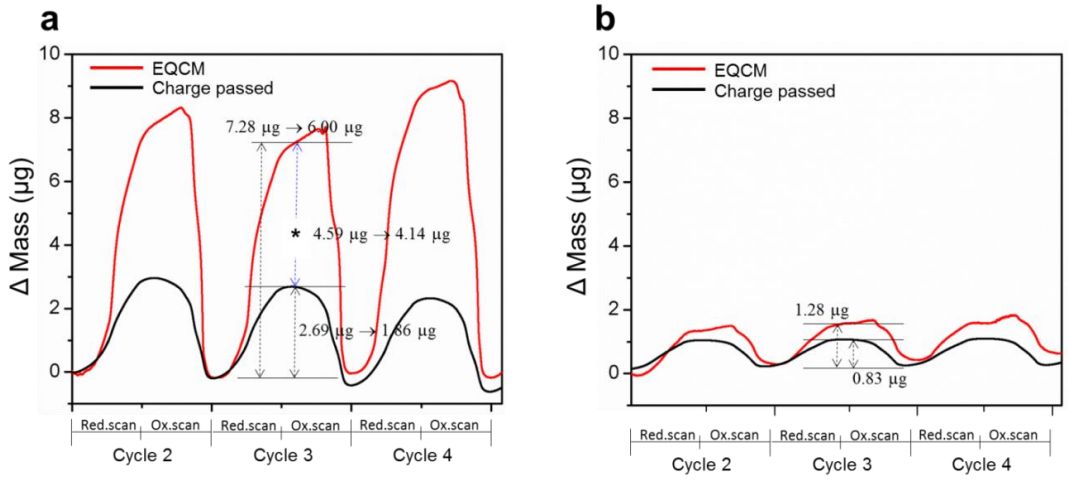

Figure 4.11 Change in mass of MnO_2 electrode measured by EQCM and amount of charge passed during CV scan in a) 0.1 M $Mg(ClO_4)_2 \cdot 6H_2O$/PC and b) 0.1 M $Mg(ClO_4)_2$/PC.

retained 67% of its initial value after 200 cycles.

We believe that the improved cycling stability compared to other MnO_2 systems is not only due the nanostructured electrode but also due to the presence of water molecules in the electrolyte. The presence of water may facilitate some pseudocapacitive charge storage behavior at high current densities where primarily fast and reversible surface reactions are contributing to the capacity.

4.3.4 Water Effect on Mg^{2+} Insertion/Deinsertion: "Activation" of MnO_2 in Water Containing Electrolyte

In order to further investigate the role of water molecules for the observed Mg^{2+} insertion/deinsertion capacity, an electrochemical quartz crystal microbalance (EQCM) was utilized to examine whether the Mg^{2+} ions co-insert along with the water molecules or completely desolvate from the hydration shell before the insertion.

Figure 4.11 shows the mass change of a thin film MnO_2 electrode during the CV scan in water containing (Fig. 4.11a) and dry (Fig. 4.11b) Mg electrolytes determined by EQCM measurement and calculated from the amount of charge passed during CV scans. In general, reversible increases and decreases in masses during the reductive scan (insertion of Mg^{2+}) and oxidative scan (deinsertion of Mg^{2+}), respectively, were observed. Sauerbrey equation was used to calculate the mass change based on the frequency change of the quartz crystal electrode:[139]

$$\Delta f = -C_f \cdot \Delta m \qquad \text{(Eqn. 4.1)}$$

where Δf is the observed frequency change in Hz, Δm is the change in mass per unit area in g/cm^2, and C_f is the sensitivity factor for the crystal in $Hz\mu g^{-1}cm^2$. Prior to any measurement, the EQCM was calibrated for C_f value using Cu plating/stripping technique in 10 mM of $CuSO_4$ and 1 M of H_2SO_4 solution. The mass change based on the amount of charge passed was calculated according to Faraday's law.

Assuming that the mass change calculated by the amount of charge passed during CV scan is solely coming from the Mg^{2+} insertion/deinsertion, the difference in mass change values between EQCM and the amount of charge (marked as *) was regarded as the mass change by the incorporation of the water molecules into MnO_2. However, it should be noted that the difference in mass change values (*) was also observed in a dry Mg electrolyte condition (< 1000 ppm) as it can be seen from Figure 4.11b. Therefore, the mass change values observed for the dry Mg electrolyte were regarded as background signals which may have resulted due to the surface-adsorbed Mg^{2+}

species without water incorporation and other possible non-water related ion-pairing interaction at the electrode surface. The mass change due to water incorporation (*) and the mass change due to the Mg^{2+} insertion were determined to be 4.14 μg and 1.86 μg, respectively. After converting these masses into moles of H_2O and Mg, it was determined that about 3 equivalent moles of water molecule per 1 mole of Mg^{2+} are estimated to co-exist in MnO_2 after the reductive scan in the water containing Mg electrolyte. Since it is possible that these components contributing to the background may behave differently in the wet condition than in dry condition, the presented water incorporation amount is provided as an approximation value.

These results agree with that from Novak et al.'s V_2O_5 study where it was proposed that the water molecules are co-inserted into the layered structure of V_2O_5 with Mg^{2+} ions and expelled upon the reoxidation.[37] However, in their study the enhanced Mg^{2+} insertion capacity was no longer observed as the V_2O_5 electrode was transferred to the dry Mg electrolyte after cycling in water containing Mg electrolyte. This implies that the V_2O_5 system always requires enough water molecules present in the electrolyte environment to solvate Mg^{2+} ions and have continuous Mg^{2+} insertion/deinsertion activities. Thus, Novak *et al.* concluded that the water molecules play their role by allowing Mg^{2+} ions to overcome the ionic interactions present in the electrolyte and electrode and that the solvation shell of water molecules is essential for their V_2O_5 system in order to exhibit enhanced Mg^{2+} insertion/deinsertion capacity. On the other hand, in the case of MnO_2, it was revealed that the improved Mg^{2+} insertion/deinsertion behavior was continuously observed in dry Mg electrolyte

after substantial cycling in water containing Mg electrolyte (Fig. 4.12). We refer to this finding as "activation" of the MnO_2. Figure 4.12 compares CV curves of MnO_2 nanowire electrodes cycled in dry Mg electrolyte before and after substantial cycling in water containing Mg electrolyte. The "activated" MnO_2 electrode that was cycled in dry Mg electrolyte demonstrated clear redox peaks, regardless of whether the activation cycles were stopped after being discharged (Fig. 4.12a) or being charged (Fig. 4.12b). Note that the electrode stopped at the discharged state after cycling in water containing Mg electrolyte is expected to contain Mg^{2+} ions and water molecules that are remained in MnO_2, while the electrode stopped at the charged state contains no or negligible amount of Mg^{2+} ions and water molecules. In contrast to CV curves measured in dry Mg electrolyte without prior cycling in wet Mg electrolyte (Fig. 4.13), both activated electrodes show distinct redox peaks indicating good Mg^{2+} insertion/deinsertion capacities. However, the CV curves for the activated electrodes that were started as discharged (Fig. 4.12a) and charged (Fig. 4.12b) MnO_2 states show different trends in their redox behavior.

The CV curve of MnO_2 electrode, whose "activation" process was stopped at the discharged state, resembles the observed CV curve in the water-containing electrolyte. This implies that the water molecules that remained inside of the discharged MnO_2 continue to play a role in cycling similar to their role in water containing electrolyte. On the other hand, the CV of MnO_2 electrode that was stopped at the charged state during the "activation" process and has a negligible amount of water present in the system, shows clean and distinct anodic and cathodic peaks at around 0.8 V and 0.2 V vs. Ag/AgCl. These peaks are shifted from the expected peak

positions slightly. Based on these observations, we believe that the water effect does not only work through resolving the ionic interaction issue (i.e., electrostatic interaction and ionic pairing) but that the water also stimulates to alter some properties of MnO_2 electrode to provide enhanced Mg^{2+} insertion/deinsertion capacity. Indeed, high-resolution TEM (HRTEM) analysis of MnO_2 electrode after

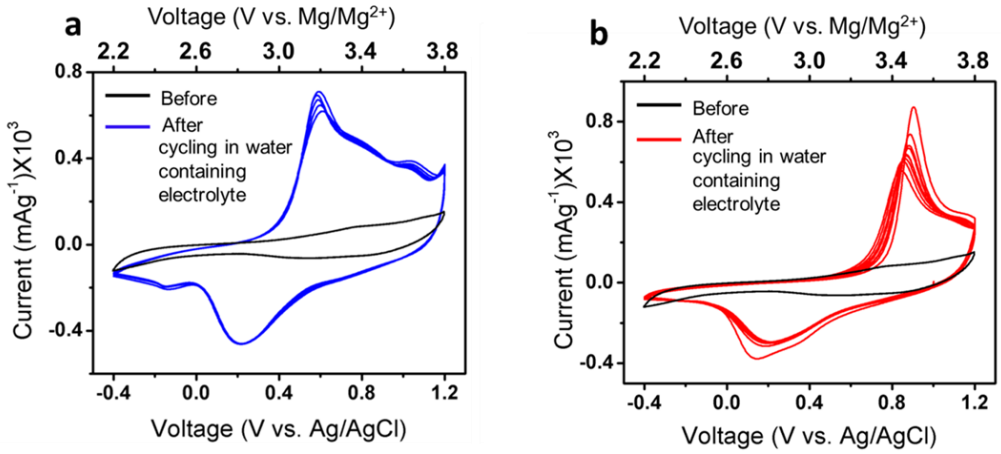

Figure 4.12 a) CV of MnO2 nanowire electrode measured in 0.1 M $Mg(ClO_4)_2$/PC electrolyte before and after cycling in 0.1 M $Mg(ClO_4)_2 \cdot 6H_2O$/PC. Measurement after cycling 0.1 M $Mg(ClO_4)_2 \cdot 6H_2O$/PC was started at discharged state and b) charged state.

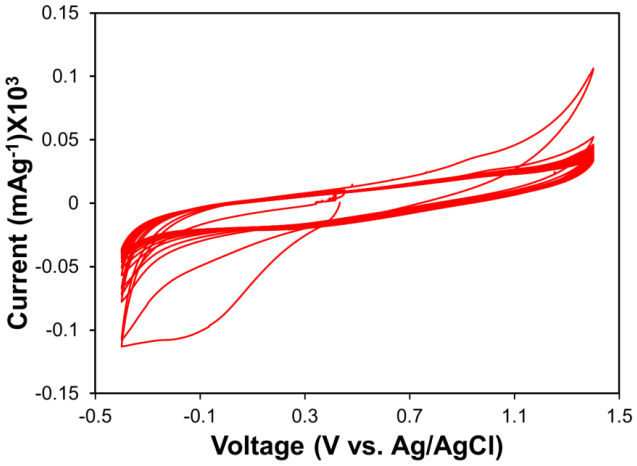

Figure 4.13 CV of MnO2 nanowire electrode measured in 0.1 M $Mg(ClO_4)_2$/PC for 23 cycles at a scan rate of 0.5 mVs^{-1}.

cycling in water containing Mg electrolyte (Fig. 4.14) shows that there is evidence of several newly formed crystal domains (~ 6 nm). However, due to the relatively weak crystallinity of the observed polycrystalline MnO_2, the exact crystal phase of MnO_2 electrode after cycling in water containing electrolyte is not definitive. We believe that there is slight structure reorientation upon substantial cycling in water containing

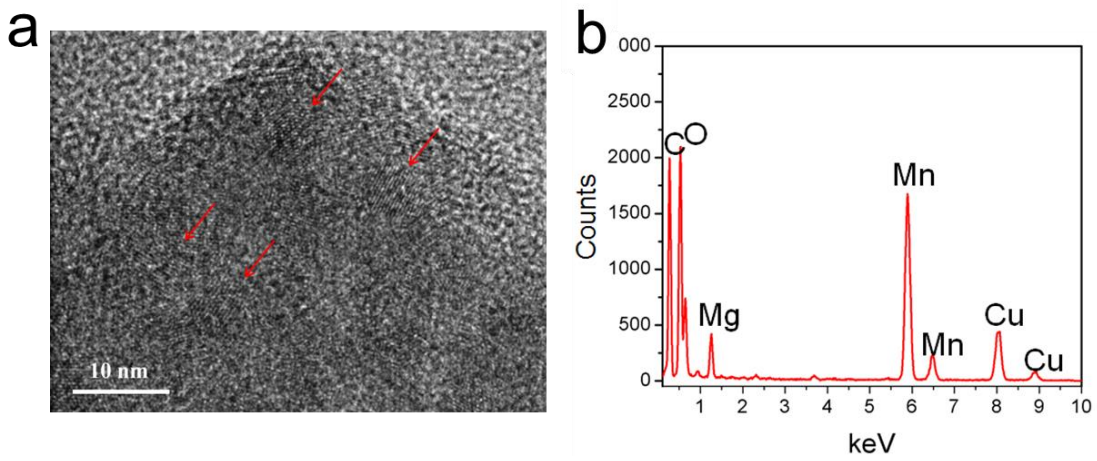

Figure 4.14 (a) High resolution TEM image of MnO_2 nanowire electrode in discharged state after cycling in 0.1 M $Mg(ClO_4)_2 \cdot 6H_2O$/PC for 10 cycles. Crystal domains with ~ 6 nm sizes are indicated by red arrows and (b) corresponding EDS analysis showed that there is no electrolyte residue remained.

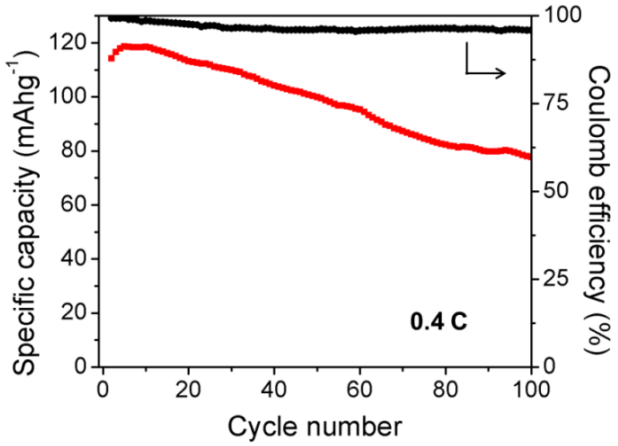

Figure 4.15 Cycling performance of MnO_2 nanowire electrode measured in 0.1 M $Mg(ClO_4)_2$/PC at a 0.4 C rate.

electrolyte which could have resulted in the observed "activation" phenomena.

Figure 4.15 shows the cycling performance of MnO_2 nanowire electrode measured in dry Mg electrolyte after cycling in water containing Mg electrolyte using activated carbon cloth as reference and counter electrode. It shows that the initial specific capacity (~ 120 $mAhg^{-1}$) is less even at slower rate (0.4 C) compared to that of the water containing electrolyte (Fig. 4.10). Nonetheless, the presented cycling stability of MnO_2 nanowire electrode (~ 70 % after 100 cycles) is outstanding compared to the previously reported MnO_2-Mg systems.

4.4 Conclusions

We have shown an improved insertion/deinsertion capability of Mg^{2+} into MnO_2 nanowire electrodes in a water-containing electrolyte. Both electrochemical and elemental analysis results revealed that the ratio between water molecules and Mg^{2+} ions in the electrolyte is a crucial factor in the Mg^{2+} insertion into MnO_2. We have demonstrated a synergic effect of water shielding and electrodes with well-defined nanostructure on the Mg^{2+} insertion performance into MnO_2. Furthermore, we have found that the MnO_2 can be "activated" as a cathode material for Mg^{2+} by pre-cycling in water containing electrolyte. The schematic of the major findings of the presented study is illustrated in Figure 4.16. We showed that the activation contributes to the structural change of MnO_2 nanowire electrode upon cycling thereby facilitating Mg^{2+} insertion/deinsertion capacities even in the absence of water molecules.

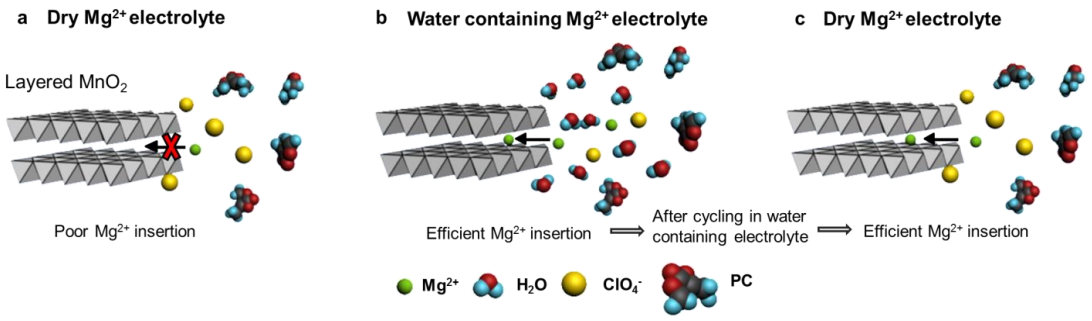

Figure 4.16 Schematic of Mg^{2+} insertion process in layered MnO_2 cathode. (a) Mg^{2+} insertion process in dry Mg^{2+} electrolyte ($Mg(ClO_4)_2$/propylene carbonate). (b) Mg^{2+} insertion process in water containing Mg^{2+} electrolyte ($Mg(ClO_4)_2 \cdot 6H_2O$/propylene carbonate). (c) Mg^{2+} insertion process in dry Mg^{2+} electrolyte ($Mg(ClO_4)_2$/propylene carbonate) after cycling in water containing electrolyte (b).

Chapter 5 Investigation of Water Stimulated Mg^{2+} Insertion Mechanism in MnO_2

5.1 Introduction

In the previous chapter, a positive effect of water molecules on the insertion behaviors of Mg^{2+} ions into MnO_2 was discussed where the water solvation shell was presumed to mitigate the ionic interaction between the divalent Mg^{2+} ions and their surrounding ionic environments. In addition, it was presented in the study that the consecutive electrochemical cycling of MnO_2 in the water-containing Mg electrolyte resulted in the "activation" of MnO_2 after which MnO_2 continued to show good Mg^{2+} insertion capability even after the removal of water molecules from the electrolyte system.

The positive effect of water molecules for Mg^{2+} insertion behavior has been further reported by a few recent follow-on studies. For example, Nam et *al.* reported a similar phenomenon where it was shown that the structural water molecules in MnO_2 play a significant role in the Mg^{2+} insertion process.[76, 140] Their study has demonstrated that the cycling in aqueous Mg electrolyte induces a phase transformation of a spinel-Mn_3O_4 to a crystal water-containing birnissite-MnO_2, activating MnO_2 for an improved Mg^{2+} insertion capacity. STEM analysis confirmed the presence of crystal water content within the MnO_2 lattice that underwent consecutive cycling in aqueous electrolyte. In addition, Sun et *al*. have recently reported the different Mg^{2+} insertion behaviors between MnO_2 in aqueous and organic electrolyte where the similar water effect was observed in the aqueous

electrolyte.[141] In both studies, the role of water molecules was mainly attributed to its charge screening behavior mitigating the electrostatic interaction between Mg^{2+} and MnO_2 lattice.

In regards to the charge storage mechanism of many hosting compounds including MnO_2, it has been commonly assumed until very recently that Mg^{2+} ions would follow a similar insertion path to that of Li^+ ions via insertion/deinsertion of Mg^{2+} as shown in the following equation:

$$x\mathrm{Mg}^{2+} + \mathrm{MnO}_2 + 2x\mathrm{e}^- \leftrightarrow \mathrm{Mg}_x MnO_2 \qquad \text{(Eqn. 5.1)}$$

However, a few recent studies suggest that Mg^{2+} ions may have a different electrochemical mechanism than that of Li^+ ions in organic electrolyte system. Recently, Arthur et *al*. have suggested that MnO_2 undergoes a conversion process in organic Mg electrolyte system rather than the insertion of Mg^{2+} based on comprehensive experimental data and DFT calculations.[142] It was found in that study that an amorphous layer or shell composed of mixed (Mn, Mg)O is formed on the surface of crystalline K-αMnO_2 upon the first discharge while the core remains as pristine MnO_2. The authors have concluded that the origin of this amorphous layer is the product of MnO_2 conversion reaction upon the discharge, which predominantly occurs at the surface of MnO_2. Further DFT calculation study has revealed that the conversion reaction is more favored than the insertion of Mg^{2+} in MnO_2 due to the high thermodynamic stability of MgO.[143] Based upon this conclusion, the authors have suggested that the formation of amorphous layer could be one of the possible causes for the observed poor cycling stability of MnO_2 with Mg^{2+}, along with a

possible dissolution of Mn and overcharging behavior (i.e., electrolyte oxidation).

To gain better understating of our previous work presented in Chapter 4 and encouraged by the abovementioned follow-on studies, a systematic analysis of MnO_2 thin film electrodes is conducted in this study to determine the charge storage mechanism of MnO_2 and to investigate how the water molecules are involved during the Mg^{2+} insertion and observed activation process. The surface analysis of MnO_2 thin film electrodes by X-ray photoelectron spectroscopy (XPS) reveals that the charge storage process of Mg^{2+} in MnO_2 in the water-containing electrolyte is not just simple insertion/deinsertion mechanism, but rather involves formation of magnesium hydroxide ($Mg(OH)_2$) on the surface of MnO_2 upon discharge. We propose herein that the formation of $Mg(OH)_2$ during the discharge process could be the significant driving force for the observed improvement for Mg^{2+} insertion in the presence of water molecules (Eqn. 5.2), which could occur predominantly or partially during the discharge process accompanied with Mg^{2+} insertion. Initial results suggest that the consecutive cycling in the water-containing electrolyte could result in a gradual increase in structural water molecules within the MnO_2 lattice, which we believe to be one of the possible origins of the observed activation phenomenon along with the structural transformation that was discussed in Chapter 4.

5.2 Experiment

5.2.1 Synthesis of Thin Film MnO_2 Electrode

Thin film MnO_2 electrode was prepared by electrodeposition method. First, 300 nm think platinum (Pt) was sputtered on the branched side of an AAO template

as a current collector using a Denton Desk III sputter coater. A strip of copper tape was then attached to the Pt sputtered side of the membrane. The AAO piece with copper tape attached was sealed between the layers for Parafilm, where a 0.32 cm^2 hole was created to define the working electrode area. Using a three-electrode set up, MnO_2 was electrodeposited in 100 mM manganese acetate solution with a constant voltage of 0.6 V vs. Ag/AgCl until 15 mC charge was accumulated. The as-prepared MnO_2 working electrode was carefully dried and was soaked in the electrolyte solution in which the electrode is tested prior to testing.

5.2.2 Electrochemical Measurement

The water-containing electrolyte and dry electrolytes were prepared by dissolving 0.1 M of hexahydrated magnesium perchlorate ($Mg(ClO_4)_2 \cdot 6H_2O$) and anhydrous magnesium perchlorate($Mg(ClO_4)_2$), respectively, in PC. Electrolytes were purged with argon gas prior to using. A three-electrode beaker cell was used with a thin film MnO_2 working electrode, Pt foil counter electrode, and Ag/AgCl reference electrode. The MnO_2 samples at various charged state were electrochemically tested first with CV technique followed by a constant potential method (i.e., chronoamperometric) until a negligible current is observed, which indicates that the electrode is near to fully charged or discharged state.

For the study of activation phenomenon, two types of activated MnO_2 electrodes were prepared: a) pre-cycled MnO_2 in the water-containing electrolyte whose electrochemical cycling was stopped when it was at the discharged state (AD-MnO_2), and b) pre-cycled MnO_2 in the water-containing electrolyte whose

electrochemical cycling was stopped when it was at the charged state (AC-MnO_2). The pre-cycling of MnO_2 electrodes was done by running 10 cycles of CV in 0.1 M of $Mg(ClO_4)_2 \cdot 6H_2O$ /PC. The activated electrodes were washed thoroughly and transferred to a dry $Mg(ClO_4)_2$/PC for further electrochemical testing. For XPS analysis of the activated electrode, both AD-MnO_2 and AC-MnO_2 electrodes were discharged in dry electrolyte after 3 runs of CV cycles.

5.2.3 X-ray Photoelectron Spectroscopy (XPS)

XPS analysis was performed by using a Kratos AXIS 165 spectrometer. All peaks were calibrated to the hydrocarbon peak at 284.8 eV. The curves were fitted using CasaXPS software. Spectra were processed using Gaussian-Lorentzian functions and a Shirley-type background.

5.3 Results and Discussion

5.3.1 Synthesis and Characterization of MnO_2

A thin film structured MnO_2 used in this study due to the highly surface limited nature of XPS technique. To prepare the electrode, MnO_2 was electrochemically deposited to ensure a good contact between the active material and current collector. AAO was used as a substrate for the electrochemical test, where the branched side was sputtered with Pt to provide an electrical conductivity. Instead of electrodepositing MnO_2 from the pore side, by which one-dimensional nanowire structures are typically grown, the Pt sputtered side of AAO was utilized for the synthesis of thin film MnO_2. This particular type of substrate with nanoscale

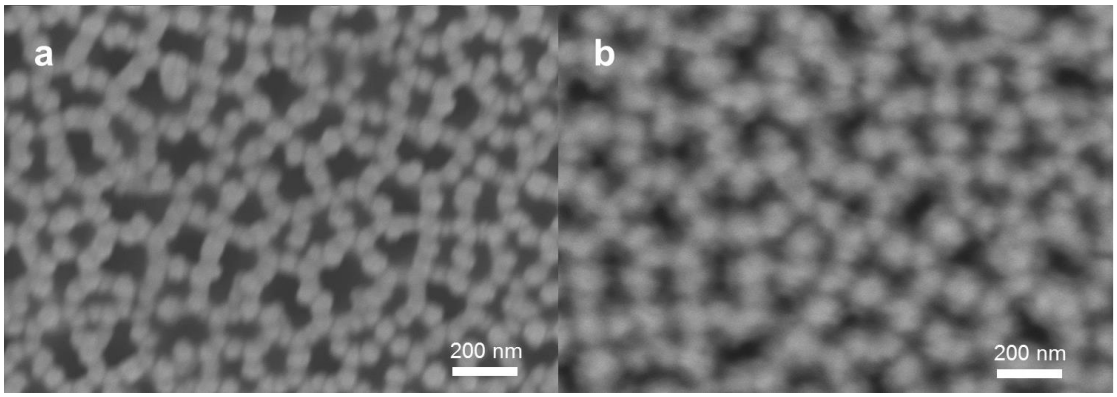

Figure 5.1 SEM images of (a) Pt sputtered AAO surface (branched side), and (b) Pt sputtered AAO surface after electrodeposition of MnO_2. The poor image quality of b) is an indicative of successful MnO_2 deposition.

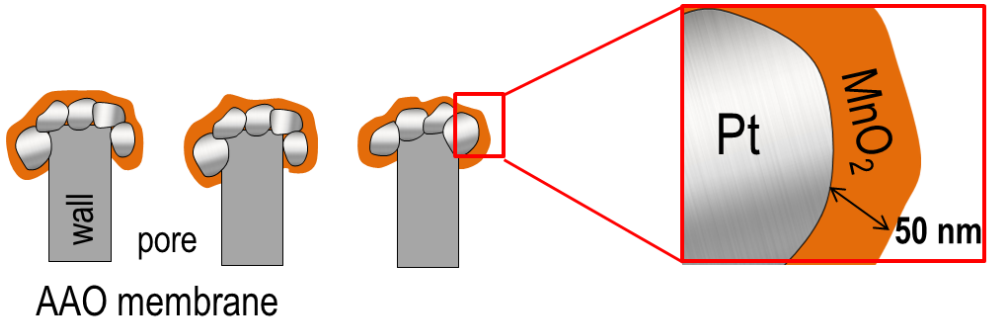

Figure 5.2 Schematic illustration of cross-sectional view of the electrodeposited MnO_2 thin film on Pt sputtered AAO template. The nanograin sized Pt on AAO surface provides the best adhesion between the current collector and MnO_2 with minimum material loss.

roughness provided the best adhesion between the electrodeposited MnO_2 and substrate without any significant material loss during the prolonged electrochemical tests and better electrochemical signal with higher surface area. The surface of Pt sputtered side of AAO is shown in Figure 5.1a. It can be seen that the Pt was deposited on the AAO surface in the form of nanosized grains (< 50 nm) where the pores of AAO remained open after the sputtering. The SEM image of Pt surface after

the MnO_2 electrodeposition in Figure 5.1b shows an increased charging effect generating a poor quality image, as well as reduced pore size. This indicates a successful deposition of thin film MnO_2. The thickness of MnO_2 is estimated to be approximately 50 nm based on the pore size change after the deposition. The electrodeposited MnO_2 film on the Pt sputtered AAO is illustrated in Figure 5.2.

5.3.2 Charge Storage Mechanism of MnO_2 in the Water-Containing Mg Electrolyte

Figure 5.3 shows CV curves of thin film MnO_2 electrodes cycled in the water-containing and dry $Mg(ClO_4)_2$/PC electrolyte at a scan rate of 0.5 mVs^{-1}. It is observed that the Mg^{2+} ion capacity of thin film MnO_2 electrode in the water-containing electrolyte is significantly greater than that of measured in the dry electrolyte, which confirms that the positive effect of water molecules for Mg^{2+} insertion process is also observed in the thin film structured MnO_2 electrode. Two peaks at 0.25 V and 0.1 V vs. Ag/AgCl are observed during the cathodic scan, which we assign as indicatives for the reduction of Mn^{4+} to Mn^{3+} and Mn^{3+} to Mn^{2+}, respectively, while the two peaks at 0.7 V and 1.1 V vs. Ag/AgCl during the anodic scan are attributed for Mn oxidation from Mn^{2+} to Mn^{3+} and Mn^{3+} to Mn^{4+}, respectively.[144] However, the exact valence states of Mn during the discharge and charge process which will support the observed CV trend were not able to be determined in the current study.

A series of *ex-situ* XPS measurements for charged and discharged MnO_2 electrodes was conducted to examine the evolution of chemical speciation on the

electrode surface upon the discharging and charging process of MnO_2. Table 5.1 summarizes the atomic composition of detected chemical species determined by XPS analysis for the various charged state of MnO_2 electrodes.

The reversibility of the Mg^{2+} insertion process in the water-containing electrolyte was examined by analyzing the atomic composition of Mg obtained by XPS survey spectra in the discharged and charged MnO_2 electrodes (Table 5.1). It shows that ~ 95 % of the Mg detected in the surface of the discharged (10.5 %) MnO_2 is retracted upon the charging (0.6 %) revealing highly reversible charge and discharge process of MnO_2 thin film electrode with Mg^{2+} ions.

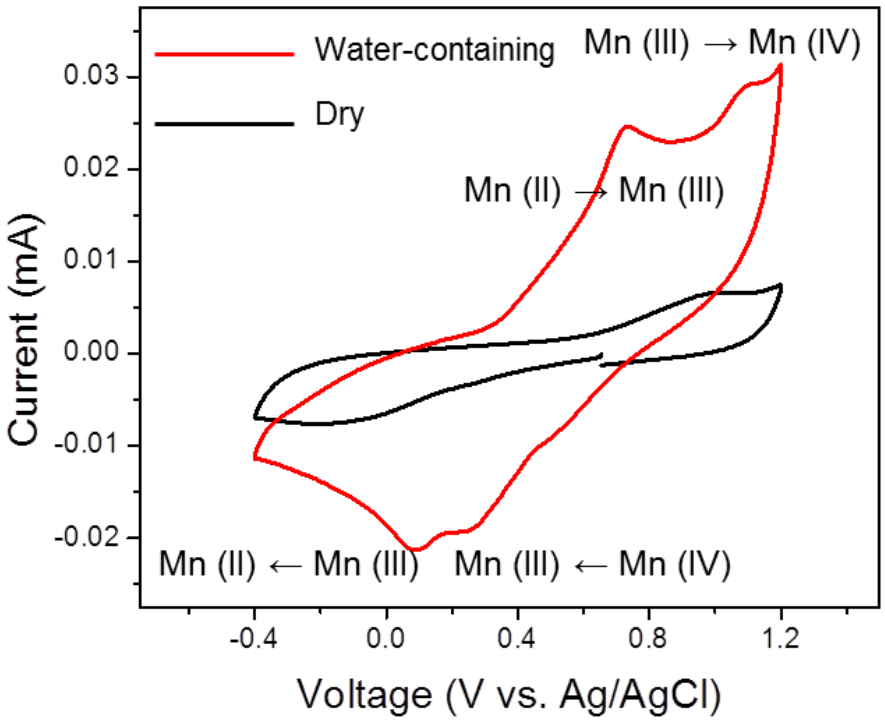

Figure 5.3 CV of thin film MnO_2 electrodes measured in the water-containing (red) and dry (black) $Mg(ClO_4)_2$ in PC at a scan rate of 0.5 mVs^{-1}.

As discussed in section 2.4.4, the Mg 2s and Mn 3s XPS spectra overlap significantly and determining the Mn valence state using Mn 3s peak separation is not possible. Therefore, Mn 2p spectra regions were used in this study to estimate the change in the Mn valence state. The Mn $2p_{3/2}$ spectrum of discharged (i.e., Mg^{2+} inserted) MnO_2 electrode (Fig. 5.4) shows the evolution of a shoulder peak at 641 eV compared to that of charged MnO_2. This shoulder peak in Mn 2p region is believed to be indicative of the reduction of Mn to a lower valence state[145, 146]. However, the exact valence state of Mn in the MnO_2 electrodes cannot be determined with Mn 2p region as the peak shift between different valence states of Mn (~ 0.1 eV)[147] is often less than the resolution of the detector. Raman spectroscopy data shown in Figure 4.6 of the discharged MnO_2 further support that Mn undergoes a reduction reaction upon the discharge.[59, 135] Coupling this information with the atomic percentages increase of Mg in the discharged spectra, it is clearly indicated that the reduction of Mn is accompanied with content increase of Mg^{2+}.

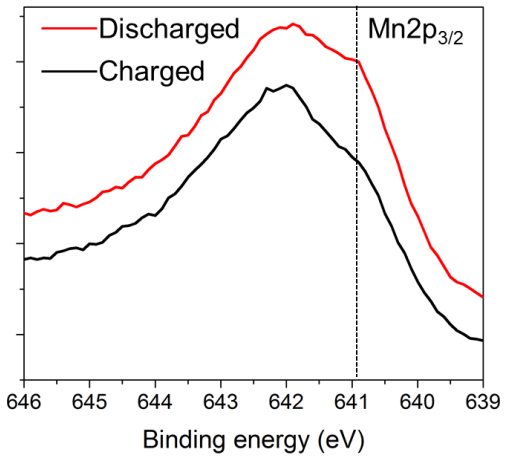

Figure 5.4 $Mn2p_{3/2}$ XPS spectra of discharged (red) and charged MnO_2 (black) electrodes in the water-containing electrolyte.

Figure 5.5 shows O 1s XPS spectra of MnO_2 electrodes. In general the peak fitting of O 1s spectra of MnO_2 electrodes resulted in three peaks with binding energies of 530 eV, 531.8 eV, and 533.3 eV. In the O 1s spectrum of the pristine MnO_2 electrode (Fig. 5.5a), a lower binding energy peak at 530 eV is observed which is responsible for the metal bound oxide component (O_2^-) of MnO_2.[99] The higher binding energy peak located at 531.8 eV is generally attributed to hydroxide (-OH) and carbonyl group (-C=O).[100, 148] In pristine MnO_2, the 531.8 eV peak is believed to be result of the possible manganese oxyhydroxide (MnOOH) formed on the surface of MnO_2 that could exist on the surface of electrodeposited MnO_2 and naturally occurring forms of carbon species by CO_2 absorption. The peak at 533.3 eV is responsible for the surface adsorbed or structural water molecules and carbon species with C-O bond.[140] Table 5.1 contains the detailed atomic composition of the components in peak fitted O 1s and C 1s spectra of MnO_2 electrodes. Note that for the discharged MnO_2 electrode that is responsible for the shown Mn 2p spectrum in Figure 5.4, its discharge process was controlled such that the electrode does not undergo a full discharge; under excessive discharge of MnO_2 in the water-containing electrolyte, the XPS signal for Mn species is significantly screened due to the formation of $Mg(OH)_2$ layer (will be discussed in detail below).

Upon the discharge of MnO_2 in the water-containing electrolyte, the peak for OH and C=O (531.8 eV) significantly increases with respect to the oxide content (~530 eV) and the oxide component is no longer observed. While the significant increase in the peak intensity at 531.8 eV could be result of electrochemically reduced carbonaceous species of propylene carbonate at the electrode surface, the C 1s

spectrum of the discharged MnO_2 electrode (Figure 5.6) reveals that the increase in the composition of C=O species remains relatively unchanged after discharge; hence the large increase in the peak at 531.8 eV with respect to the peak responsible for oxide species (530 eV) is mostly attributed to the formation of a hydroxide species in a form of thick surface layer that is greater than (or at least comparable to) the penetration depth of XPS (~10 nm), such that the oxide component presumed to exist underneath of the hydroxide layer was only minimally detected.

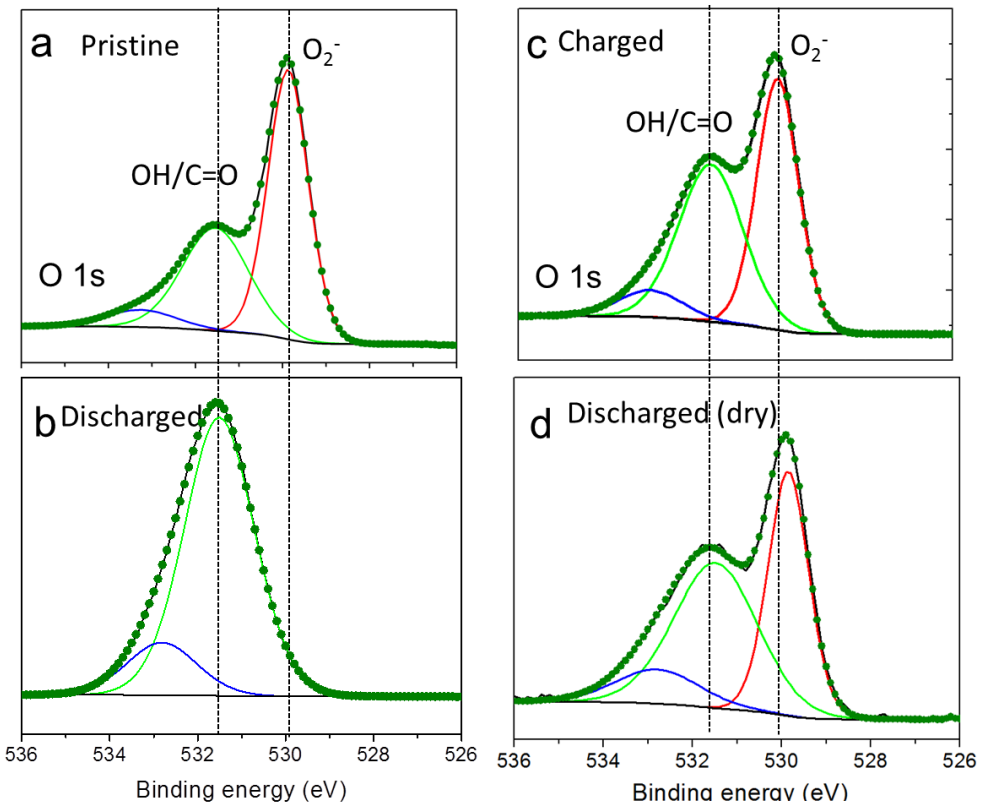

Figure 5.5 O 1s XPS spectra of (a) pristine, (b) discharged MnO_2 in water-containing electrolyte, (c) charged MnO_2 in the water-containing electrolyte, and (d) discharged MnO_2 in the dry electrolyte.

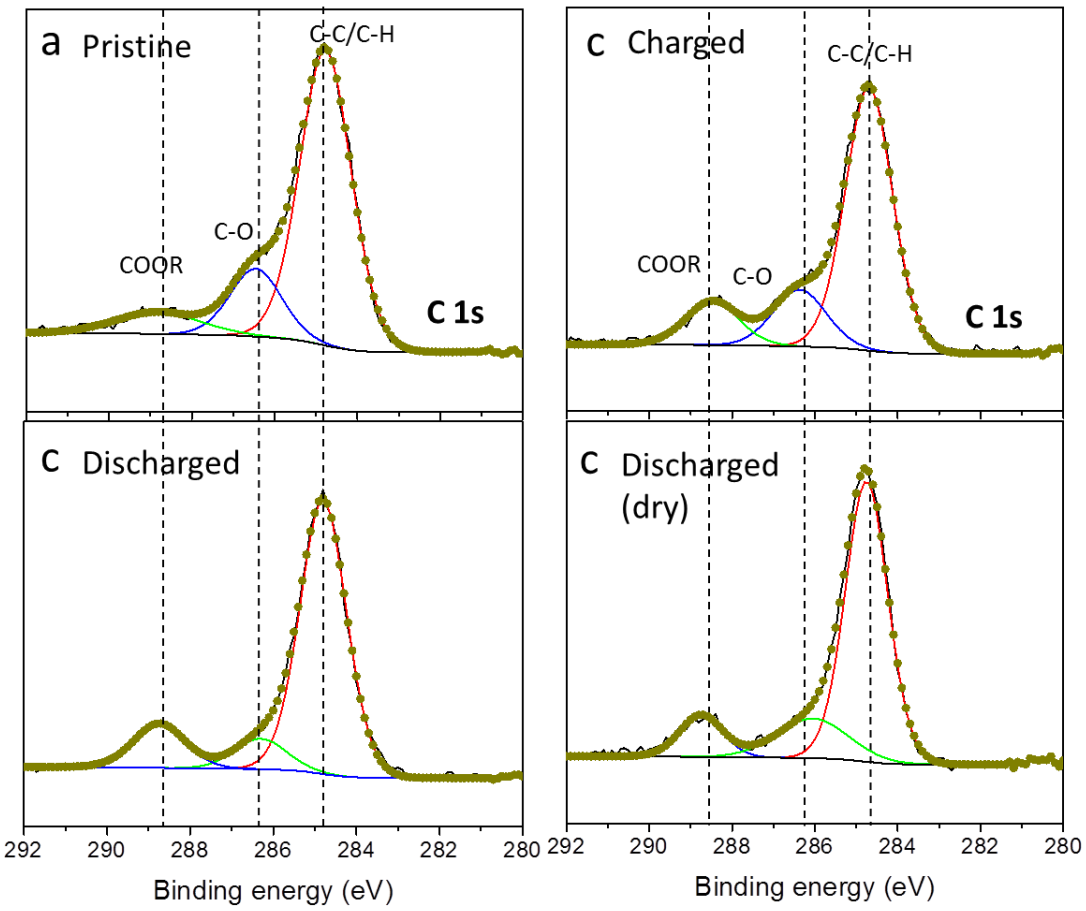

Figure 5.6 C 1s XPS spectra of (a) pristine, (b) discharged MnO_2 in water-containing electrolyte, (c) charged MnO_2 in the water-containing electrolyte, and (d) discharged MnO_2 in the dry electrolyte.

While the observed hydroxide layer can be identified to be both $Mg(OH)_2$ or $Mn(OH)_2$, it is important to note that the atomic composition of Mn is significantly reduced proportional to the amount of hydroxide species (Table 5.1). This strongly implies that the detected hydroxide species is less likely to be MnOOH or $Mn(OH)_2$; thus we conclude that the observed hydroxide component is identified to be $Mg(OH)_2$ that was formed on top of the Mn oxide component.

In the charged MnO_2 electrode, the hydroxide component decreases and Mn and oxide compositions are restored, indicating a reversible behavior of the $Mg(OH)_2$ formation. The reversibility is further supported by the observed decrease in the atomic composition of Mg after the charging.

The formation of $Mg(OH)_2$ was apparent only when there is excess amount of water contents in the electrolyte system. Figure 5.5d shows the O 1s XPS spectrum of MnO_2 electrode discharged in dry electrolyte. While there is also slight increase in the observed OH composition with respect to the oxide component, the degree of hydroxide formation of the discharged MnO_2 electrode in the dry electrolyte is significantly less than that of discharged MnO_2 in the water-containing electrolyte (Fig. 5.5b). We believe that the hydroxide formation in the dry system will be even less if the water content had been carefully controlled. On the other hand, in a complete aqueous environment, an extensive formation of $Mg(OH)_2$ was observed similar to that of water-containing electrolyte which further suggests the correlation between the presence of water molecules and $Mg(OH)_2$ formation.

In the presence of water molecules, one of the possible explanations for the

Table 5.1 Atomic composition and peak fitted data results determined by XPS for MnO_2 electrodes in various charged states

	Composition %							Peak ratio	
	Mg	Mn	OH	O_2^-	C-C/C-H	COOR	C-O	OH/O_2^-	COOR/C-C
Pristine	-	23.4	36.1	57.5	72.6	11.2	16.1	0.6	0.2
Discharged	10.5	1.7	84.1	-	65.7	24.8	9.4	-	0.4
Charged	0.6	21.7	16.3	58.7	79.6	14.1	6.2	0.3	0.2
Discharged in dry	7.1	15.9	40.7	46.2	71.5	13.6	14.7	0.9	0.2
Discharged in Aqueous	10.3	1.6	82.3	1.1	60.8	24.8	14.2	74.8	0.4
Charged in Aqueous	1.4	21.3	49.6	47.6	82.7	12.6	4.6	1.0	0.2
Discharged (Activated in charged state)	13.4	7.8	44.6	22.2	64.9	22.5	12.6	2.0	0.3
Discharged (Activated in discharged state)	15.1	4.3	59.8	10.6	75.2	14.4	10.3	5.6	0.2

observed $Mg(OH)_2$ formation is that it is the reaction product of a precipitation reaction combined with electrolysis of water at the electrode surface as $Mg^{2+} + 2\,(OH)^- \rightarrow Mg(OH)_2$. To examine the possible contribution of the precipitated $Mg(OH)_2$, a clean surface of Pt electrode was prepared at which the precipitation reaction was enforced by applying a reductive potential of -1.0 V vs. Ag/AgCl in $Mg(ClO_4)_2 \cdot 6H_2O$/PC, followed by reoxidation at 1.2 V vs. Ag/AgCl. The Mg 1s (Fig. 5.7a and b) and O 1s (Fig. 5.7c and d) XPS spectra of the Pt electrodes reveal irreversible formation of $Mg(OH)_2$ where the intensity of Mg 1s peaks remain the same between the two reduced and reoxidized Pt surfaces, which contradicts to the observed reversibility of $Mg(OH)_2$ formation in MnO_2 electrodes. Therefore, the possible contribution of precipitated $Mg(OH)_2$ is determined to be not significant in the observed $Mg(OH)_2$ formation on the discharged MnO_2 electrodes. However, as discussed in Chapter 4, it should be noted that in a complete aqueous system, there could be higher degree of side reactions involving water molecules, including the precipitation of $Mg(OH)_2$, than that of the water-containing electrolyte which is supported by the slightly decreased reversibility observed in the aqueous electrolyte (Table 5.1). That is, in aqueous electrolyte, 86 % of Mg in the discharged MnO_2 is retracted after recharge, whereas 95 % of Mg is retracted after recharge in the water-containing electrolyte.

The observed reversible formation of $Mg(OH)_2$ during the charge and discharge processes of MnO_2 suggests that the charge storage mechanism of MnO_2 in the presence of water molecules may involve more than a simple insertion process that was described in Eqn. 5.1. We believe that the formation of $Mg(OH)_2$ is the

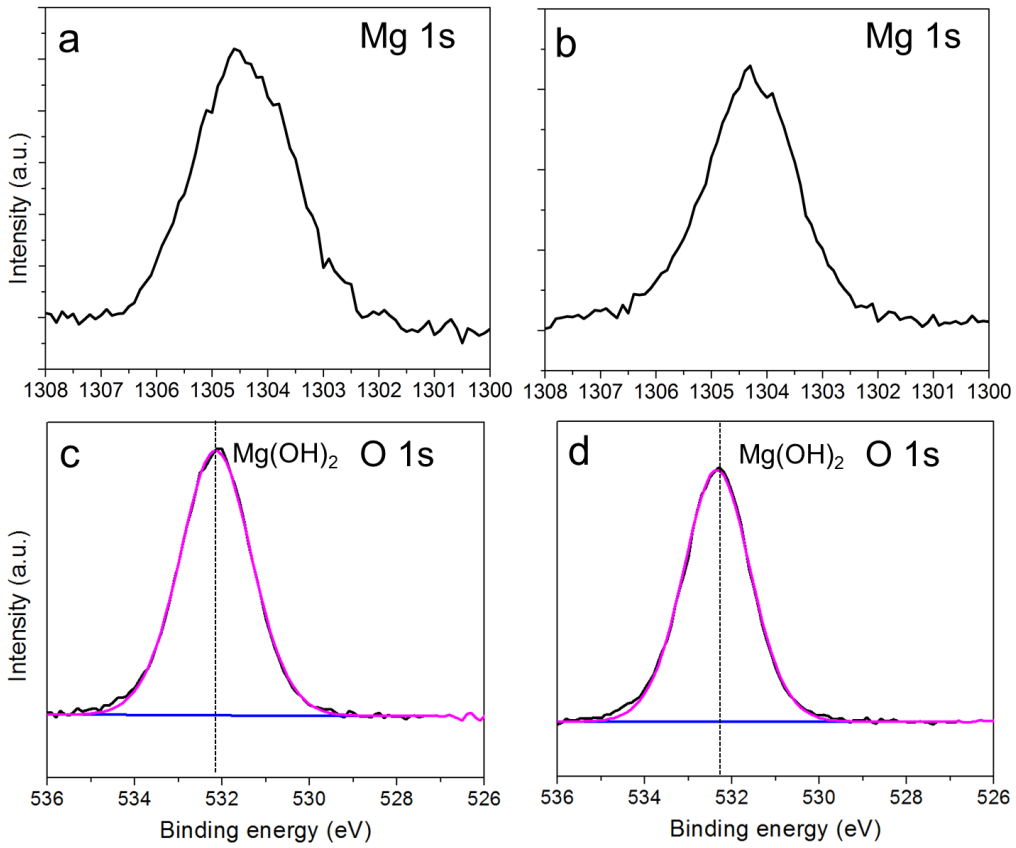

Figure 5.7 (a) Mg 1s and (c) O 1s XPS spectra of platinum surface after reductive potential and (b) Mg 1s and (d) O 1s XPS spectra of platinum surface after reductive potential followed by oxidative potential applied in $Mg(ClO_4)_2 \cdot 6H_2O$/PC.

reaction product of MnO_2 discharge process when there is water molecules present in the system and could be responsible for the observed improvement for Mg^{2+} insertion.

Based on the combined information of the XPS analysis discussed above, we propose the following conversion charge storage mechanism of MnO_2 in the presence of water molecules.

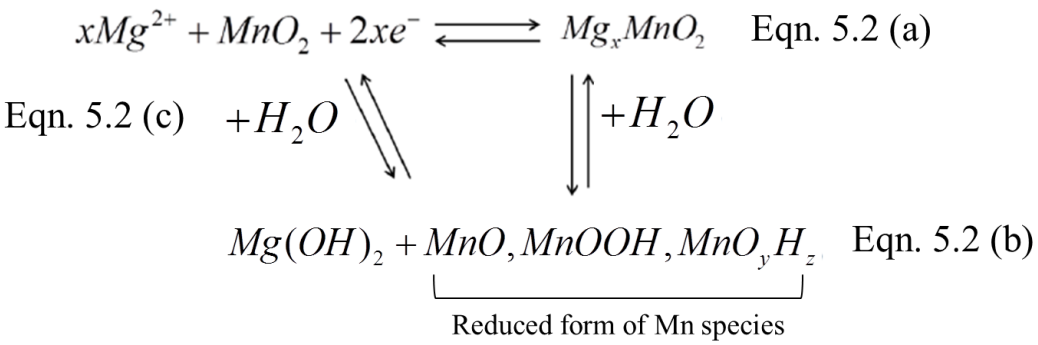

The apparent reduction and oxidation behaviors of Mn species observed both in CV and Raman spectra of MnO_2 electrodes indicate that MnO_2 does undergo a reduction reaction compensated by inserted Mg^{2+} ions, possibility in the form of Mg_xMnO_2 upon the discharge (Eqn. 5.2a). In the presence of water molecules, Mg_xMnO_2 converts to inhomogeneous composition of $Mg(OH)_2$ surface layer and possible $MnO_{(3-2x)}H_{(2-2x)}$ species underneath of $Mg(OH)_2$ (Eqn. 5.2b). Another possible discharging mechanism is direct conversion from MnO_2 to $Mg(OH)_2$ and $MnO_{(3-2x)}H_{(2-2x)}$ species (Eqn. 5.2c). Upon the charging, the oxidation of Mn species reverses the reaction that is otherwise irreversible as observed in Fig. 5.7. However, due to the surface limited nature of XPS analysis, the proposed mechanism was built largely based upon the observed $Mg(OH)_2$ surface layer formation with no direct evidence to support the possible existence of the proposed MnO_x or $Mn(OH)_2$ species. The MnO_x or $Mn(OH)_2$ species (or both) is most likely present underneath of $Mg(OH)_2$ based on the reduced Mn composition with increased hydroxide component and vice versa. However, we claim that the Raman spectroscopy results (presented in Chapter 4), which show that the bulk portion of MnO_2 electrode is reversibly reduced upon the discharge, provide clear enough evidence to conclude that there exist a

reduced form of MnO_2 under the $Mg(OH)_2$ layer, although the exact phase could not be determined. For this reason, please note that the provided reaction equations are not balanced with limited information of Mn species.

Recent study by Sun el *al*., also reported the formation of $Mg(OH)_2$ surface layer during the Mg^{2+} insertion process of MnO_2 and suggested the surface conversion mechanism of MnO_2.[141] However, in their study the authors concluded that the formation of $Mg(OH)_2$ is observed only in the dry electrolyte system whereas in aqueous system Mg^{2+} ions undergo an intercalation rather than conversion reaction. In that study, the difference in the charge storage behaviors between the dry and aqueous electrolytes was attributed to the charge screening effect of water molecules by which the intercalation of Mg^{2+} was favored over conversion mechanism in aqueous electrolyte. In organic systems, it was suggested that the conversion reaction is triggered by transformation of Mg_xMnO_2 into the thermodynamically more favorable hydroxide and oxide compounds where the structure of Mg_xMnO_2 is expected to be unstable as a result of strong electrostatic interaction between inserted Mg^{2+} ions and ionic matrix of MnO_2.

While limited evidence was provided in the Sun et *al.*'s study, the results obtained in this study lead to a different conclusion regarding the charge storage mechanism of MnO_2 with Mg^{2+} ions. We propose that in both in aqueous and organic electrolyte systems, where the water molecules are present in the system either in the electrolyte or within MnO_2 as a structural water, the charge storage process of MnO_2 with Mg^{2+} ion is governed by the conversion reaction from Mg_xMnO_2 to $Mg(OH)_2$

and $MnO_{(3-2x)}H_{(2-2x)}$. We propose that when the thermodynamically unstable Mg_xMnO_2 meets water molecules, it converts to more stable $Mg(OH)_2$ and $MnO_{(3-2x)}H_{(2-2x)}$. Also, we suggest that the formation of $Mg(OH)_2$ in conjunction with the charge screening effect could be the driving force that has generated the observed improvement in Mg^{2+} capacity in the presence of water molecules.

5.3.3 Charge Storage Mechanism of Activated MnO_2

To better understand the mechanism of the observed activation phenomenon of MnO_2 electrodes that was discussed in Chapter 4, the surface species of the activated MnO_2 electrodes were also investigated by XPS. Figure 5.8 shows CV of activated and pristine thin film MnO_2 electrodes cycled in the dry electrolyte at a scan rate of 0.5 mVs^{-1}. Please note that the two pairs of peaks during the cathodic and anodic scan that were observed in the water-containing electrolyte (Figure 5.3) become very weak in the dry electrolytes after the water activation of MnO_2; the difference in CV (i.e., reduced peak intensity and capacity) trend observed between the MnO_2 electrode cycled in the water-containing electrolyte and activated MnO_2 electrode cycled in dry electrolyte represents the contribution of water molecules that come from the water-containing electrolyte.

In general, higher capacities are observed in the activated MnO_2 electrodes compared to the pristine MnO_2. Note that depending on the charge state of activated MnO_2, a different CV trend is observed. That is, the activated MnO_2 electrode that was at the discharged state when it was transferred to dry electrolyte (AD-MnO_2) shows more distinctive redox peaks and higher capacity than that of the activated

electrode that started at the charged state (AC-MnO_2).

The activated electrode that was at the discharged state (AD-MnO_2) is expected to have $Mg(OH)_2$ layer formed on its surface when it was transferred to dry electrolyte for continued cycling. On the other hand, no or much less amount of $Mg(OH)_2$ layer is expected to exist in the activated MnO_2 whose pre-cycling (or

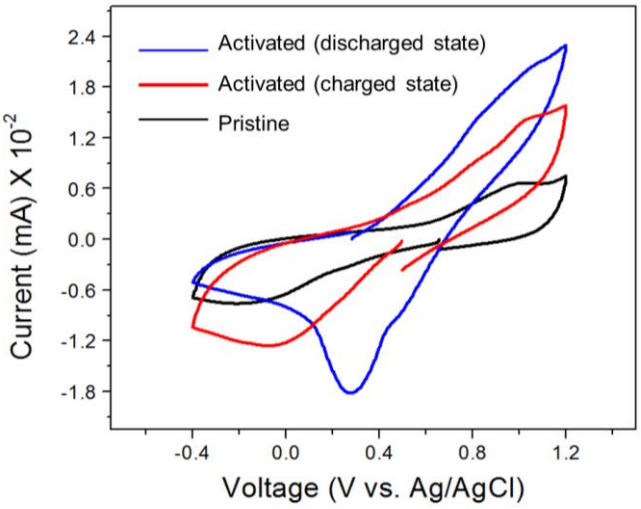

Figure 5.8 CV of pristine and activated MnO_2 electrodes measured at a scan rate of 0.5 mVs^{-1}.

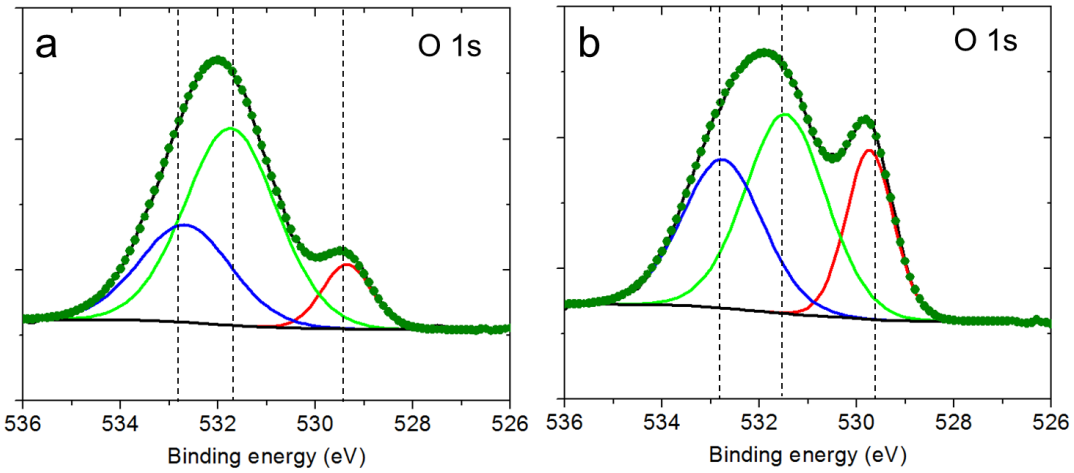

Figure 5.9 O 1s XPS spectra of (a) discharged AD-MnO_2, and (b) discharged AC-MnO_2 in dry electrolyte.

activation process) was stopped at the charged state (AC-MnO_2). Figure 5.9 shows O 1s spectra of AD-MnO_2 (Fig. 5.9a) and AC-MnO_2 (Fig. 5.9b) that were discharged in the dry electrolyte. Both types of activated electrodes show that the $Mg(OH)_2$ layer is formed after discharging, where a higher degree of $Mg(OH)_2$ formation was observed for AD-MnO_2.

The results demonstrating the significant degree of $Mg(OH)_2$ is continued to be observed when the activated electrodes were cycled in dry electrolyte condition implies that there still exists the source of water to form $Mg(OH)_2$ in both types of electrodes. There are two possible fate for the water molecules after the reverse reaction of $Mg(OH)_2$ formation (Eqn. 5.2) upon charging in the water-containing electrolyte; the water molecules may be extracted from MnO_2 lattice and go into the electrolyte system, or it could remain within the MnO_2 lattice as structural water. However, if the water molecules are extracted from MnO_2 and exist mostly only in the electrolyte in a very small amount, negligible degree of $Mg(OH)_2$ formation should have been observed when the activated electrodes were cycled in dry electrolyte. The fact that the significant amount of $Mg(OH)_2$ are continued to be observed at the activated MnO_2 electrode surface after cycling in the dry electrolyte suggests that it is probable that the water molecules remain within the MnO_2 lattice as a structural water. In addition, O 1s spectra of both activated electrodes show an increase in the peak intensity at a binding energy of ~533 eV compared to that of the inactivated electrodes (Fig. 5.5), strongly suggesting the presence of structural water in the activated electrodes. Hence, the pre-cycling or activation process in the water-containing electrolyte resulted in a gradual increase of structural water within the

MnO_2 lattice, by which the conversion reaction to $Mg(OH)_2$ and improved capacity were continued to be observed even in the absence of water molecules in the electrolyte system. Additionally, the gradual increase in the structural water molecules in MnO_2 could be one of the possible origins of the MnO_2 activation phenomenon. The schematic of the proposed activation mechanism is illustrated in Figure 5.10.

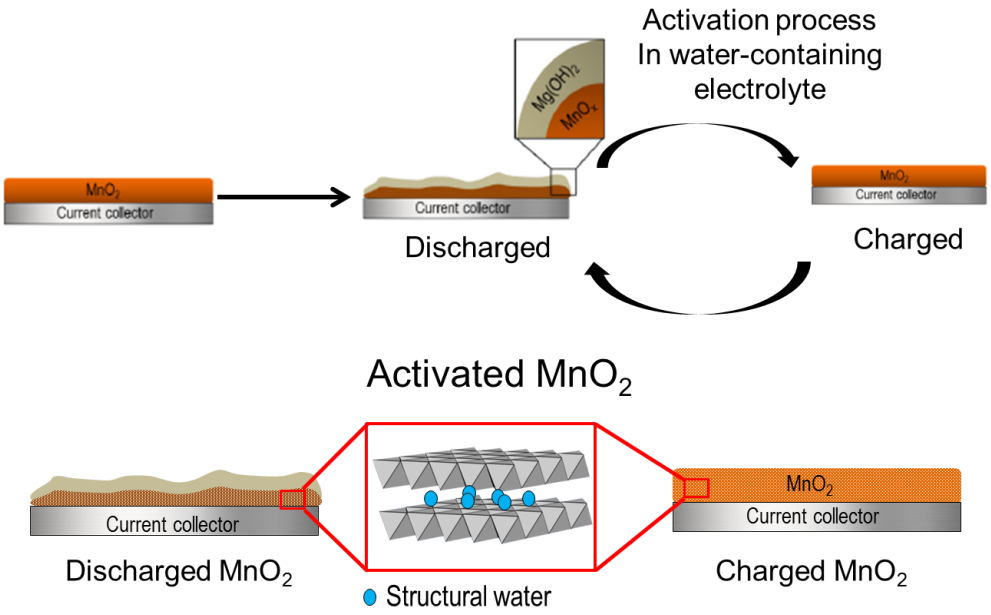

Figure 5.10 Schematic of the proposed mechanism for the activation process by water molecules.

5.4 Conclusion

The XPS analysis of the thin film MnO_2 electrodes revealed that there is significant degree of reversible formation of $Mg(OH)_2$ surface layer during the Mg^{2+} charge storage process in MnO_2 when there are water molecules present in the system. It was proposed in this study that the presence of water molecules induces a

conversion reaction involving formation of $Mg(OH)_2$, which is proposed to be one of the origins of the observed improvement for Mg^{2+} insertion.

The XPS analysis of the activated MnO_2 electrodes cycled in the dry electrolyte showed the $Mg(OH)_2$ continues to be observed even in the absence of water molecules in the electrolyte system. It was suggested that the consecutive cycling in the water-containing electrolyte generates structural water within MnO_2 that continues to be involved in the charge storage process in the dry electrolyte environment.

While the preliminary result of XPS study presented herein provide better understanding of the role of water molecules during Mg^{2+} insertion process, further study is needed to clarify and support the conclusions. For example, an investigation of the structural water content in MnO_2 electrodes after the activation process is strongly suggested to support the proposed activation mechanism as well as further depth profiling study of MnO_2 electrodes to determine the detailed composition of MnO_2 electrodes during the charge storage process. Finally, a systematic calculation-based study is suggested to elucidate the thermodynamic foundation of the conversion mechanism.

Chapter 6 Summary and Outlook

6.1 Summary

The overall goal of this dissertation was to investigate the charge storage mechanism of MnO_2, focusing on the insertion behaviors of divalent Mg^{2+} ions and exploring the origins of the limited Mg^{2+} insertion behavior in MnO_2. A systematic investigation of nanostructured MnO_2 during Mg^{2+} insertion/deinsertion process revealed that Mg^{2+} insertion is significantly improved in the presence of water molecules.

This dissertation has taken the following approaches to achieving the overall goal:

1) Introduction of water molecules in organic Mg electrolyte: utilized water-containing organic Mg electrolytes where the preferential solvation of Mg^{2+} by water molecules over the organic solvent molecule was expected to mitigate the electrostatic force between Mg^{2+} ions and surrounding ionic environment improving the limited Mg^{2+} capacity in MnO_2.

2) Utilization of nanostructured MnO_2 electrode: one-dimensional free-standing MnO_2 electrode was used which is not only beneficial in facilitating the Mg^{2+} diffusion by the increased surface area and reduced Mg^{2+} diffusion path, but also allowing precise analysis of the electrode owing to its well-defined structure.

3) Investigate the charge storage mechanism: a series of XPS analysis was done to explore the surface chemistries of MnO_2 electrodes during the charge storage process and investigated the role of water molecules during the Mg^{2+} insertion process.

These approaches overall provided better understating in the mechanism of the Mg^{2+} charge transfer process in MnO_2 and how the water molecules are involved in this process. The summary of findings includes:

Chapter 3:

i. ICP-AES analysis reveals that the charge storage mechanism of MnO_2 in aqueous Li electrolyte involves both Li^+ and proton insertion.

ii. The amorphous and nanowire structured MnO_2 allows reversible insertion of more than one Li fraction per Mn up to 1.5 mole fraction in organic Li electrolyte.

Chapter 4:

i. Limited Mg^{2+} capacity in MnO_2 can be significantly improved by introducing water molecules in the Mg electrolyte system, where the water molecules effectively mitigated the kinetic hindrance of Mg^{2+} insertion process.

ii. A nanostructured MnO_2 electrode provides further improved Mg^{2+} capacity with reduced ionic diffusion path and high surface area, both of which are beneficial for the efficient Mg^{2+} diffusion.

iii. Pre-cycling MnO_2 electrode in the water-containing electrolyte activates MnO_2 electrode by inducing a structural reorientation upon which improved Mg^{2+} capacity was continued to be observed in dry Mg electrolyte.

Chapter 5:

i. XPS analysis of thin film MnO_2 electrode at various charged state reveals that the reversible formation of $Mg(OH)_2$ is involved in the charge storage process in the water-containing electrolyte and activated electrodes.

ii. A conversion mechanism is proposed where magnesiated MnO_2 undergoes a conversion reaction to $Mg(OH)_2$ and MnO_x / $MnOH_y$ in the presence of water molecules where the conversion process is believed to be the driving force that generates the improved Mg^{2+} capacity in MnO_2 along with the water molecule's charge screening effect.

iii. Upon a consecutive cycling of MnO_2 in the water-containing Mg electrolyte, structural water is generated within the MnO_2 lattice, which is thought to be origin of the observed structural reorientation of MnO_2. These structural water molecules continues to induce the conversion mechanism in MnO_2 even when there is no water molecules present in the electrolyte.

6.2 Outlook

The results provided in this dissertation highlight that the divalency of Mg^{2+} ions result in very different electrochemical behavior than that of the well-studied monovalent Li^{+} ions towards MnO_2. It was found in this study that the water molecules enhance the poor diffusion kinetics of Mg^{2+} ions into MnO_2. However, from a practical point of view the presence of water molecules in a real Mg battery system will be fatal to Mg anode due to the high reactivity of Mg with water.

Based on the understanding gained from this dissertation regarding the charge storage behavior of Mg^{2+} in MnO_2, one could consider developing an alternative strategy that would reduce the effective interaction between Mg^{2+} and the host lattice. Additionally, leveraging from the demonstrated strategy of Li-based battery system, where a surface protection layer for metallic Li effectively prevented the parasitic reaction between Li and an aqueous electrolyte, the water-containing electrolyte system could potentially be used in a full Mg battery system upon a successful demonstration of a Mg protection layer.

Publications

Portions of Chapter 1 have been published in:

J. Phys. Chem. Lett., **2016**, *7*, 1736.

Portions of Chapter 3 have been published in:

Chem. Commun. **2014**, 50, 7352.

Portions of Chapter 4 have been published in:

Phys. Chem. Chem. Phys., **2015**,17, 5256

Portions of Appendix have been published in:

J. Nanopart. Res., **2014**, 16, 2745.

Appendix: Enhanced Electrochemical Stability of High-Voltage $LiNi_{0.5}Mn_{1.5}O_4$ Cathode by Surface Modification Using Atomic Layer Deposition

Portion of this appendix has been published in Song et al., "Enhanced Electrochemical Stability of High-Voltage $LiNi_{0.5}Mn_{1.5}O_4$ Cathode by Surface Modification Using Atomic Layer Deposition", J. Nanopart. Res. ***2014****, 16, 2745.*

Introduction

Lithium-ion batteries (LIBs) are one of the most extensively studied and developed electrical energy storage technologies. They are widely used in consumer electronics, and start to enter applications such as automotive and grid-storage.[11, 149] In order for LIBs to meet demands from the latter applications, high energy density and long-term stability are required. Since the voltage of LIB, which governs the energy density of the device, is mainly determined by the potential of its cathode material, much effort has been devoted in developing stable and high voltage cathode materials to increase the energy density of LIBs.

Spinel $LiNi_{0.5}Mn_{1.5}O_4$ (denoted as LNMO) is one of the promising high voltage cathode materials for next generation LIBs with its high and flat discharge voltage plateau around 4.7 V vs. Li^+/Li.[149] The high voltage of LNMO therefore translates into high energy density by reaching up to 658 $Wh \cdot kg^{-1}$, which is considerably higher compared to that of $LiMn_2O_4$ (440 $Wh \cdot kg^{-1}$) or $LiFePO_4$ (591 $Wh \cdot kg^{-1}$).[150] Moreover, compared to other high voltage cathode materials, such as $LiNi_xCo_yMn_zO_2$ ($0 \leq x,y,z < 1$) and $LiCoPO_4$, LNMO offers advantage of low cost and

operation safety.[151, 152] However, LNMO often suffers from poor electrochemical stability associated with its high operating voltage. Under a high voltage, solvent molecules or anions of lithium salts (i.e., PF_6^-) could undergo oxidative decomposition at the electrode/electrolyte interface, while sustaining leaching of transition metal ions (Mn^{2+} in particular) from cathode results in deterioration of interphase at anode surface.[153, 154] All those irreversible processes are responsible for capacity fading. Therefore, understanding the interfacial chemistry of electrode/electrolyte in order to come up with a plausible solution to the undesired surface reaction will be the key to the future development of LIBs with high voltage cathodes.

Generally, there are two strategies utilized to resolve these instability issues occurring at the LNMO/electrolyte interface. One is to use additives in electrolytes to improve anodic stability of the conventional electrolytes for LIBs. Recently, Cresce et al.[154] showed that the trace amount of additive species (1% tris(hexafluoro-*iso*-propyl)phosphate, HFiP) in the standard electrolyte can significantly improve the electrolyte stability (up to 5 V) where the additive species undergoes sacrificial oxidation, thereby preventing further decomposition of the bulk electrolyte component.

Another strategy for the long-term stability of LNMO is to modify the LNMO surface with metal oxides which serve as a protecting layer, or an artificial solid-electrolyte interface (SEI) layer. The oxide layers effectively prevent the decomposition of the electrolyte components and the dissolution of transition metal

ions while allowing reversible Li^+ transport.[155-157] Compared to the traditional surface modification methods, such as sol-gel[155, 156, 158], and gas-suspension spray coating [159], atomic layer deposition (ALD) technique provides elegant control over the coating thickness, thus producing ultrathin and conformal morphology.[160-163] It has been recently demonstrated that the ultrathin coatings of Al_2O_3 layer (<1 nm) on $LiCoO_2$ electrode composite by ALD technique deliver excellent durability as well as high rate in comparison to bare $LiCoO_2$ electrode.[164]

In this work, we take advantage of ultrathin layers of Al_2O_3 (~ 4 Å) by ALD to protect the high voltage LNMO cathode from undesired side reactions at its electrode/electrolyte interface (Fig. A.0.1). The Al_2O_3 coated LNMO exhibits improved electrochemical stability with over 92% capacity retention after 200 cycles, in contrast to 84% in bare LNMO. While a recent separate study has reported Al_2O_3 coating by ALD on LNMO cathode surface and its electrochemical performances[165], detailed electrode/electrolyte interfacial study for fundamental understanding regarding the role of ALD-Al_2O_3 coating was not provided. Here, we use X-ray photoelectron spectroscopy to study the surface chemistry of LNMO after cycling which shows that the undesirable reaction between LNMO surface and electrolyte is effectively suppressed by Al_2O_3 layer.

Experimental Section

Materials

Lithium acetate dihydrate, nickel acetate tetrahydrate, manganese acetate tetrahydrate, citric acid, and ammonium hydroxide used for $LiNi_{0.5}Mn_{1.5}O_4$ powder

synthesis were all purchased from Sigma-Aldrich.

Synthesis of $LiNi_{0.5}Mn_{1.5}O_4$ powders

Stoichiometric amount of lithium acetate dihydrate ($Li(CH_3COO)\cdot 2H_2O$), nickel acetate tetrahydrate ($Ni(CH_3COO)_2\cdot 4H_2O$), and manganese acetate tetrahydrate ($Mn(CH_3COO)_2\cdot 4H_2O$) was mixed in distilled water. After the mixture was heated to 50 ℃, citric acid solution with concentration equivalent to the total metal concentration, was added drop-wise to the stirred mixture solution. Ammonium hydroxide solution was added until the pH of the solution was adjusted to ~6.5. The solution was heated at 80 ℃ until a high-viscous gel was obtained. The gel was dried at 80 ℃ for 3 days and the dried gel was thoroughly grinded to obtain fine powders. The powders were heated at 450 ℃ for 10 hours under oxygen flow (heating rate: 5 ℃/min, holding time: 1 minute). The resulting powder was thoroughly grinded followed by calcination at 800 ℃ for 10 hours under oxygen flow (heating rate: 2 ℃/min).

Atomic layer deposition

The LNMO electrode composite on Al foil was placed into an atomic layer deposition system (Beneq TFS 500) for the Al_2O_3 deposition. High-purity nitrogen was used as a carrier gas. The precursor utilized for Al_2O_3 was trimethylaluminum (TMA) and H_2O. The Al_2O_3-ALD sequence includes alternating flows of TMA (4 seconds) and water (4 seconds) separated by flows of pure nitrogen gas (4 and 10 seconds for carrier and cleaning gas, respectively). The thickness of Al_2O_3 resulting

from each ALD cycle was determined to be ~ 1 Å .

Electrochemical measurements

Coin cells were assembled with Li metal as both reference and counter electrodes. The LNMO electrode composite was prepared by coating the slurry of LNMO, acetylene black, and polyvinylidene fluoride (PVDF) in 1-methyl-2-pyrrolidone (NMP) on an Al foil with 70: 20: 10 weight ratio. Electrolytes used in this work was 1 M $LiPF_6$ in EC/EMC with 1% of tris(hexafluoro-*iso*-propyl)phosphate (HFiP). Synthesis procedure for HFiP is found in literature (Cresce et al. 2011).The batteries were cycled in the voltage range of 3.5–4.9 V.

Results and Discussion

As shown in the SEM image in Fig. A.0.2a, the as-synthesized LNMO shows cubic-like shape with sizes of about 200 nm. Fig. A.0.2b shows X-ray powder diffraction (XRD) patterns of the as-synthesized LNMO. The diffraction peaks in XRD indicate the formation of well-crystallized spinel structure (JCPDS No. 80-2184). No additional peaks were observed which reveals that our as-synthesized LNMO contains no impurities.

ALD-Al_2O_3 coating was applied directly to the LNMO electrode composite in order to achieve efficient inter-particle contact and to maintain the electrical conductivity. Based on a control experiment of Si wafer, it was determined that each ALD cycle results in an Al_2O_3 layer of ~ 1 Å in thickness. Fig. A.0.2c shows a TEM image of 6 cycles of ALD-Al_2O_3 coated LNMO particles. Due to the extremely small

thickness of Al_2O_3 layer by ALD coating, the Al_2O_3 layer was not visible in the TEM image. However, the energy dispersive X-ray spectroscopy (EDS) analysis performed on the particle clearly shows the presence of Al with about 1.1 % of atomic ratio.

Fig. A.0.3a shows a cyclic voltammetry (CV) curve of the LNMO cathodes with 4 cycles of ALD-Al_2O_3 (denoted as 4-ALD-Al_2O_3/LNMO). It clearly shows reversible peaks at 4.7 V and 4.0 V regions, which are attributed to the Ni^{2+}/Ni^{4+} and Mn^{3+}/Mn^{4+} redox couple, respectively. It is well known that there are two possible crystallographic structures in LNMO, namely, ordered $P4_332$ and disordered *Fd3m* space groups. While all Mn in ordered ($P4_332$) LNMO exist in Mn^{4+}, those in disordered (*Fd3m*) LNMO are present both in Mn^{4+} and Mn^{3+} (Kim et al. 2004). Therefore, based on the Mn^{3+}/Mn^{4+} redox peak observed at 4.0 V, it can be concluded that the as-synthesized LNMO is disordered *Fd3m* space group. The charge/discharge profiles of 4-ALD-Al_2O_3/LNMO were measured between 3.5 V and 4.9 V at a rate of 0.5 C (1 C=147 mA/g). The shape of the voltage profiles for 4-ALD-Al_2O_3/LNMO is almost identical with that of bare LNMO (Fig. A.0.5), indicating that there are no significant changes in reaction mechanism after ALD-Al_2O_3 coating.

Fig. A.0.3 compares the discharge cycling performances of bare LNMO, 4-ALD-Al_2O_3/LNMO, and 6-ALD-Al_2O_3/LNMO under the same conditions. As expected, the 4-ALD-Al_2O_3/LNMO showed improved cycling performance compared to bare LNMO, retaining more than 92% of its original capacity after 200 cycles. This improvement is even more evident after 500 cycles where 4-ALD-Al_2O_3/LNMO and bare LNMO exhibited 74% and 52% of the corresponding initial capacity,

respectively (Fig. A.0.6). In fact, even the capacity retention of bare LNMO (84% after 200 cycles) is also higher than the capacity retention values for similar LNMO cathodes reported in the literature.[166] The 6-ALD-Al_2O_3/LNMO, however, delivered relatively lower specific capacity (~ 87 $mA \cdot h \cdot g^{-1}$) than 4-ALD-Al_2O_3/LNMO and bare LNMO electrodes. This decreased capacity in 6-ALD-Al_2O_3/LNMO is likely due to the restricted ionic transport through the thicker Al_2O_3 layer. Nevertheless, it is worth noting that 6-ALD-Al_2O_3/LNMO displayed the best stability with nearly 98% capacity retention after 200 cycles among these three LNMO electrodes. Therefore, it further confirms the effect of ALD-Al_2O_3 coating on cycling stability of LNMO.

In order to study the surface chemistry of the LNMO electrodes and determine the role of the surface modification in enhancing the stability of LNMO, X-ray photoelectron spectroscopy (XPS) was utilized. Due to the complication in XPS spectra from the PVDF binder and acetylene black contained in the electrodes, only significant changes upon cycling (i.e., new peaks) were taken into account for the characterization and comparative study. Fig. A.0.4 compares O 1s XPS spectrum for bare LNMO and 4-ALD-Al_2O_3/LNMO electrodes before and after 500 charge and discharge cycles. Before cycling, the O 1s spectra of both bare and ALD-Al_2O_3/LNMO are dominated by two peaks centered at ~530 eV and ~532 eV, which can be assigned for the lattice O^{2-} in LNMO and hydroxyl groups on the carbon particle, respectively.[167]

In bare LNMO, there is notable increase in the peak intensities at ~533.8 eV related to C-O and reduction in lattice O^{2-} peak at ~ 530 eV upon cycling. C 1s

spectrum (Fig. A.0.7) further support the formation of C-O, where the intensities for C-O (286.5 eV) and O-C=O (289-290 eV) are increased after cycling. These results from O 1s and C 1s spectra of bare LNMO imply that there is surface layer formation mainly composed of esters at the electrode/electrolyte interface which results in decrease in oxide signals by covering the surface of LNMO. In ALD-Al_2O_3 coated LNMO, a similar trend was observed; however, the degree of peak intensity changes in the O 1s spectrum (based on the peak ratio between C-O and M-O) is not as evident as that in bare LNMO. Thus, the improved capacity retention in ALD-Al_2O_3 coated LNMO is most likely due to the mitigated organic surface layer formation which is the product of electrolyte decomposition process. Additionally, formation of $Li_xPO_yF_z$ was observed from the P 2p spectra of both bare and ALD-Al_2O_3 coated LNMO (Fig. A.0.8) where an intense peak at ~135 eV (P-O) was observed after cycling.[157, 167]

Conclusion

In conclusion, we have demonstrated a high voltage LNMO cathode with enhanced cycling performance by modifying the electrode surface with ultrathin ALD-Al_2O_3 coating layers. The Al_2O_3 coating effectively mitigates the side reactions and keeps the LNMO surface clean from possible electrolyte decomposition products. Our XPS studies, on the surfaces of LNMO cathodes after electrochemical cyclings, fort the first time, confirm that ultra-thin Al_2O_3 can greatly reduce the decomposition of electrolytes on high-voltage Li-ion battery cathodes.

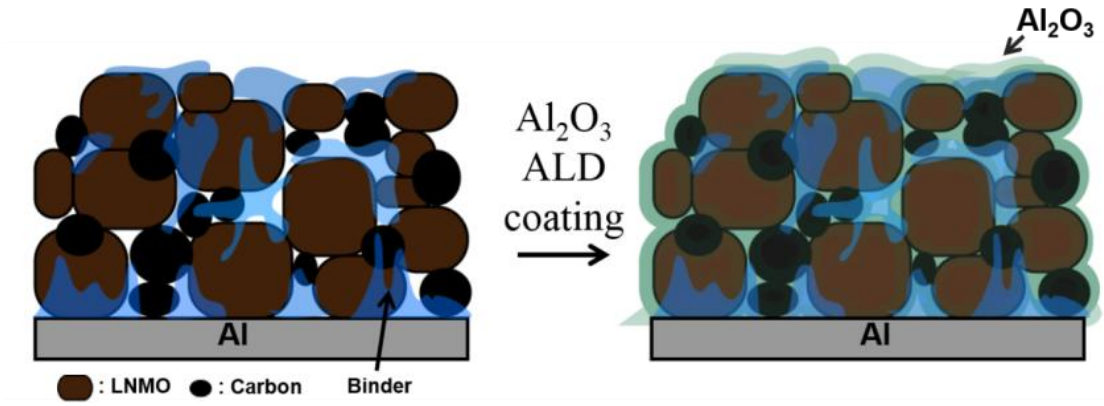

Figure A.0.1. Schematic of ALD process on LNMO electrode composite. The ALD coating was carried out on LNMO-carbon black-PVDF composites, which will not change the morphology and electrical contacts in LNMO composite cathode.

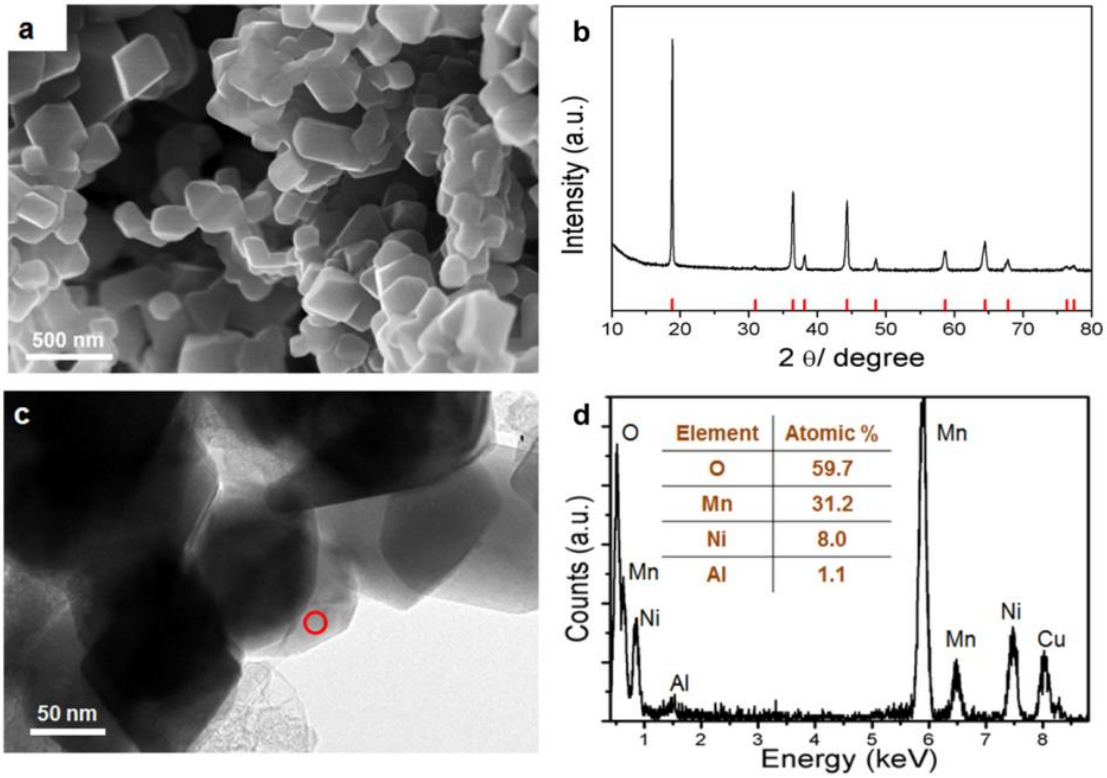

Figure A.0.2 a) SEM image of as-prepared LNMO nanoparticles b) X-ray powder diffraction pattern of the as-prepared LNMO with standard pattern (JCPDS data No. 80-2184) c) TEM image of 6 ALD-Al_2O_3 coated LNMO particles d) EDS spectrum obtained from the circled area in the TEM image. Atomic % of elements are also shown in the table.

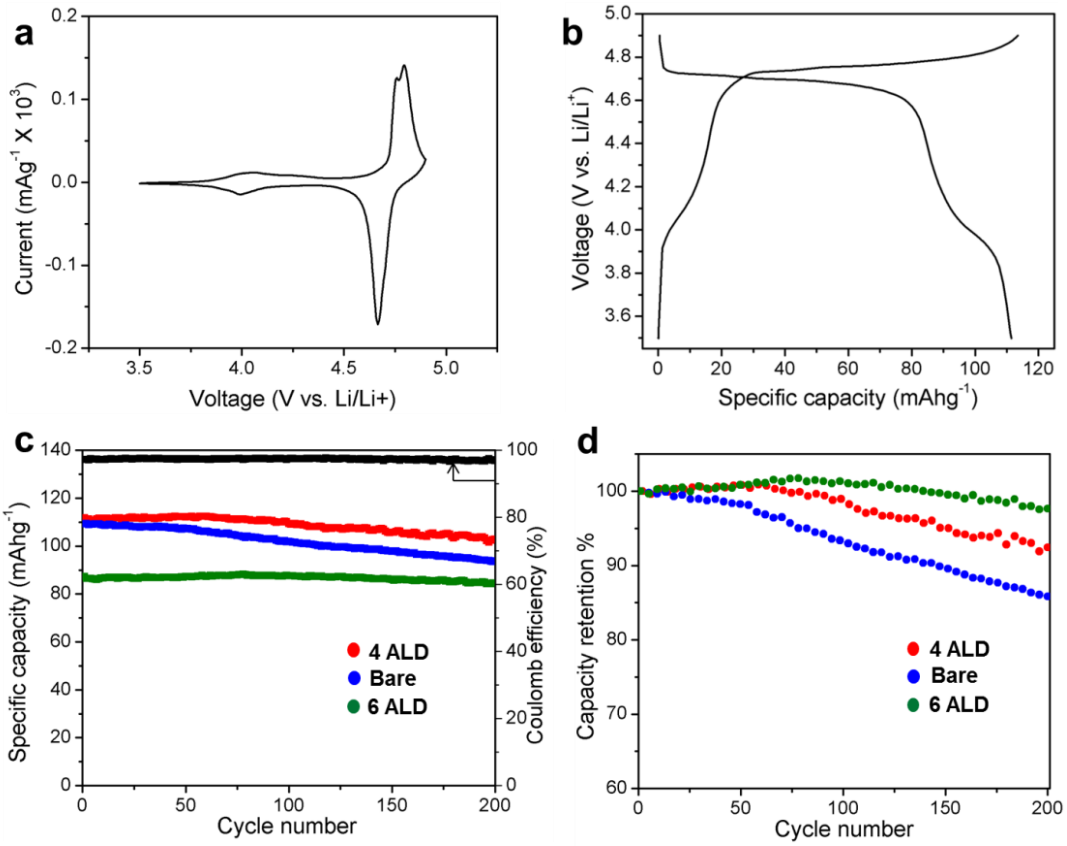

Figure A.0.3. Electrochemical characterization of Al_2O_3 coated LNMO by 4 cycles of ALD a) Cyclic voltammogram at a scan rate of 0.05 $mV \cdot s^{-1}$ b) Voltage profile measured at a rate of 0.5 C c) cycling performance of bare LNMO (blue), 4-ALD-Al_2O_3/LNMO (red) and 6-ALD-Al_2O_3/LNMO. Cells were galvanostatically charged and discharged at a rate of 0.5 C from 3.5 V to 4.9V vs. Li/Li^+. Coulomb efficiency for 4-ALD-Al_2O_3/LNMO is also shown (d) Discharge capacity retention calculated based on c).

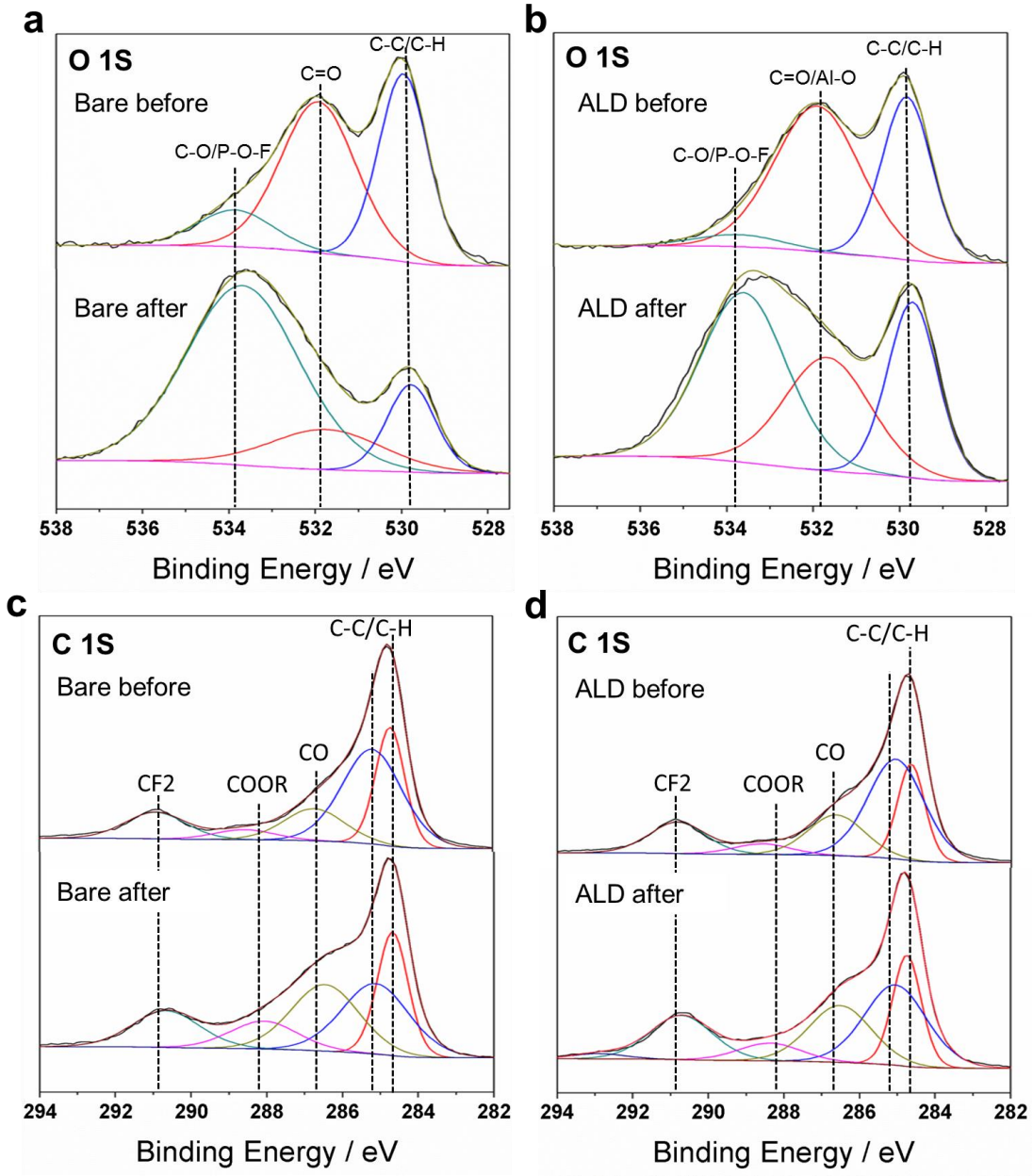

Figure A.0.4. (a) O 1s XPS spectra and (c) C 1s XPS spectra for bare LNMO before cycling (top) and after 500 charge/discharge cycles (bottom) and (b) O 1s XPS spectra and (d) C 1s XPS spectra 4 ALD-Al_2O_3/LNMO before cycling (top) and after 500 charge/discharge cycles. All peaks were calibrated to the hydrocarbon peak at 284.8 eV.

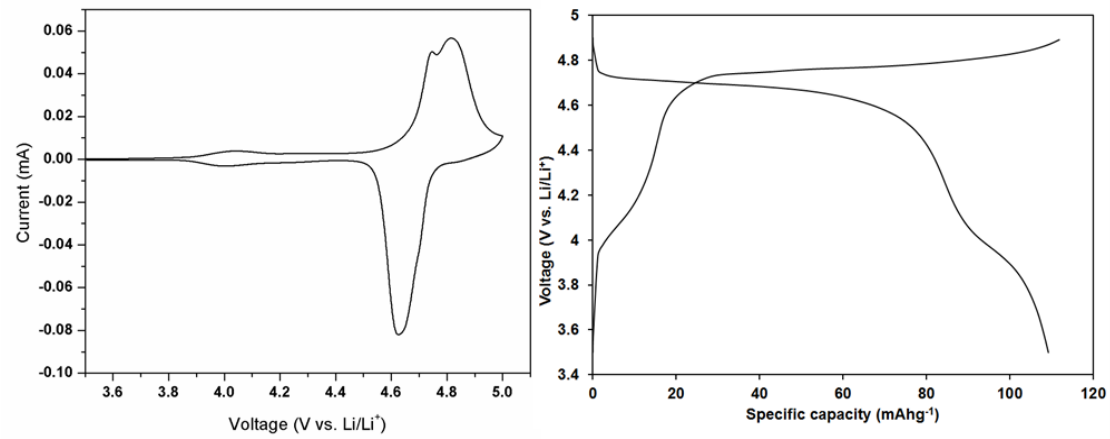

Figure A.0.5. Electrochemical characterization of bare LNMO a) Cyclic voltammogram (4th cycle) at a scan rate of 0.05 mVs^{-1}. b) Voltage profile of bare LNMO measured at a rate of 0.5 C.

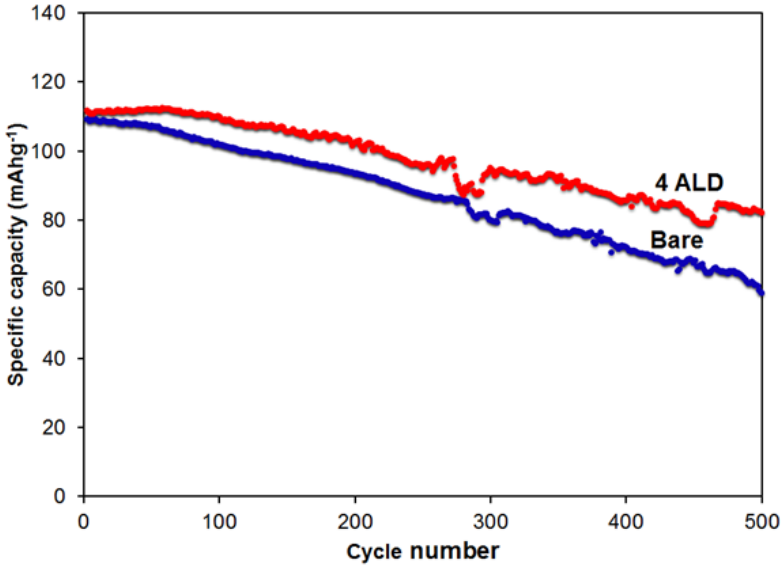

Figure A.0.6 Cycling performance of bare LNMO (blue), 4 Al_2O_3-ALD/LNMO (red) with extended cycling numbers. Cells were galvanostatically charged and discharged at a rate of 0.5 C from 3.5 V to 4.9 V vs. Li/Li$^+$.

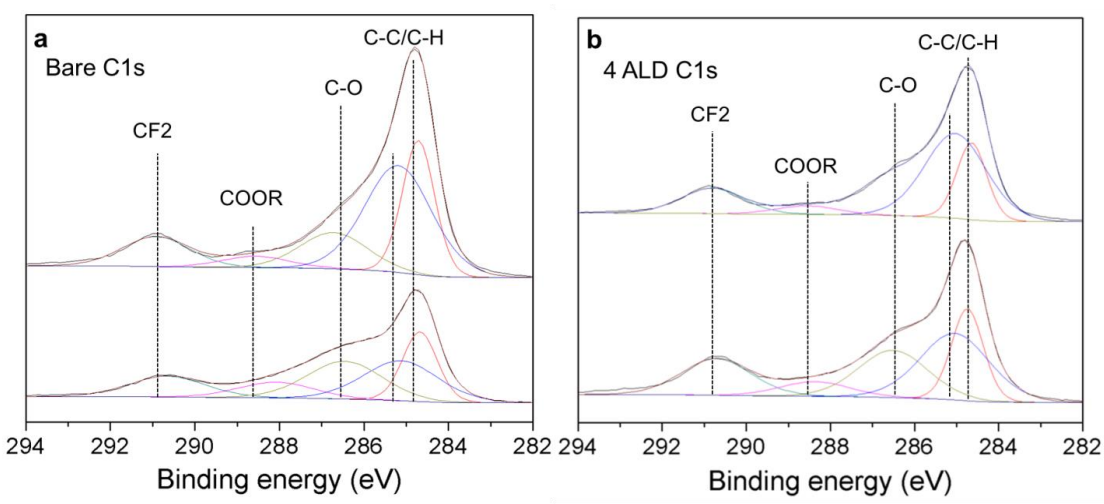

Figure A.0.7. C1s XPS spectra for (a) bare LNMO before (top) and after (bottom) 500 cycles and (b) 4 Al_2O_3-ALD coated LNMO before (top) and after (bottom) 500 charge and discharge cycles. All peaks were calibrated to the hydrocarbon peak at 284.8 eV.

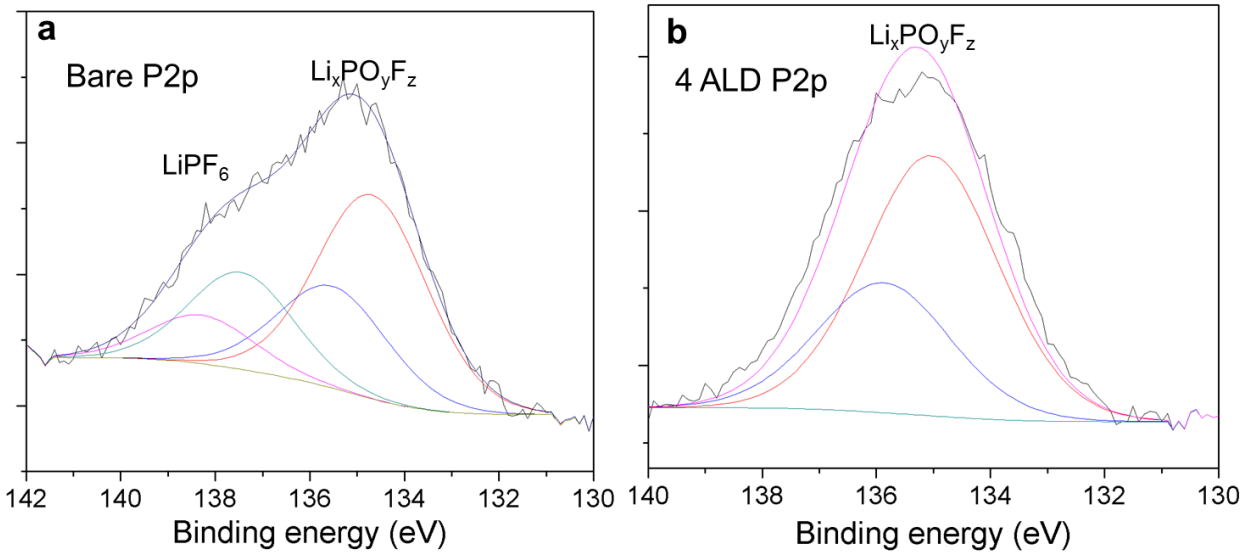

Figure A.0.8 P 2p XPS spectra for (a) bare LNMO (b) 4 Al_2O_3-ALD coated LNMO after 500 charge and discharge cycles. All peaks were calibrated to the hydrocarbon peak at 284.8 eV.

Bibliography

1. D. Aurbach, Z. Lu, A. Schechter, Y. Gofer, H. Gizbar, R. Turgeman, Y. Cohen, M. Moshkovich and E. Levi, *Nature*, 2000, **407**, 724-727.
2. A. Yoshino, K. Sanechika, T. Nakajima, *Japan Pat.*,1989293, 1985.
3. D. Aurbach, Y. Gofer, Z. Lu, A. Schechter, O. Chusid, H. Gizbar, Y. Cohen, V. Ashkenazi, M. Moshkovich, R. Turgeman and E. Levi, *Journal of Power Sources*, 2001, **97-8**, 28-32.
4. D. Aurbach, A. Schechter, M. Moshkovich and Y. Cohen, *Journal of the Electrochemical Society*, 2001, **148**, A1004-A1014.
5. D. Aurbach, Y. Gofer, A. Schechter, O. Chusid, H. Gizbar, Y. Cohen, M. Moshkovich and R. Turgeman, *Journal of Power Sources*, 2001, **97-8**, 269-273.
6. J. M. Tarascon and M. Armand, *Nature*, 2001, **414**, 359-367.
7. J. B. Goodenough and Y. Kim, *Chemistry of Materials*, 2010, **22**, 587-603.
8. D. Fauteux and R. Koksbang, *Journal of Applied Electrochemistry*, 1993, **23**, 1-10.
9. D. Aurbach, I. Weissman, Y. Gofer and E. Levi, *Chemical Record*, 2003, **3**, 61-73.
10. K. R. Kganyago, P. E. Ngoepe and C. R. A. Catlow, *Physical Review B*, 2003, **67**, 10.
11. J. B. Goodenough and K.-S. Park, *Journal of the American Chemical Society*, 2013, **135**, 1167-1176.
12. M. Nie, D. Chalasani, D. P. Abraham, Y. Chen, A. Bose and B. L. Lucht, *Journal of Physical Chemistry C*, 2013, **117**, 1257-1267.
13. C. K. Chan, R. Ruffo, S. S. Hong and Y. Cui, *Journal of Power Sources*, 2009, **189**, 1132-1140.
14. J. Xu, S. Dou, H. Liu and L. Dai, *Nano Energy*, 2013, **2**, 439-442.
15. F. A. Posey and T. Morozumi, *Journal of the Electrochemical Society*, 1966, **113**, 176-&.
16. J. Wang, *Analytical Electrochemistry*, Jon Wiley & Sons, Inc., 2006.
17. B. Dunn, H. Kamath and J.-M. Tarascon, *Science*, 2011, **334**, 928-935.
18. O. I. Malyi, T. L. Tan and S. Manzhos, *Journal of Power Sources*, 2013, **233**, 341-345.
19. N. Singh, T. S. Arthur, C. Ling, M. Matsui and F. Mizuno, *Chemical Communications*, 2013, **49**, 149-151.
20. Y. Y. Shao, M. Gu, X. L. Li, Z. M. Nie, P. J. Zuo, G. S. Li, T. B. Liu, J. Xiao, Y. W. Cheng, C. M. Wang, J. G. Zhang and J. Liu, *Nano Letters*, 2014, **14**, 255-260.
21. Y. Y. Shao, T. B. Liu, G. S. Li, M. Gu, Z. M. Nie, M. Engelhard, J. Xiao, D. P. Lv, C. M. Wang, J. G. Zhang and J. Liu, *Scientific Reports*, 2013, **3**, 7.
22. J. Muldoon, C. B. Bucur, A. G. Oliver, T. Sugimoto, M. Matsui, H. S. Kim, G. D. Allred, J. Zajicek and Y. Kotani, *Energy & Environmental Science*, 2012, **5**, 5941-5950.

23. H. D. Yoo, I. Shterenberg, Y. Gofer, G. Gershinsky, N. Pour and D. Aurbach, *Energy & Environmental Science*, 2013, **6**, 2265-2279.
24. T. D. Gregory, R. J. Hoffman and R. C. Winterton, *Journal of the Electrochemical Society*, 1990, **137**, 775-780.
25. L. W. Gaddum and H. E. French, *Journal of the American Chemical Society*, 1927, **49**, 1295-1299.
26. D. Aurbach, H. Gizbar, A. Schechter, O. Chusid, H. E. Gottlieb, Y. Gofer and I. Goldberg, *Journal of the Electrochemical Society*, 2002, **149**, A115-A121.
27. C. J. Barile, E. C. Barile, K. R. Zavadil, R. G. Nuzzo and A. A. Gewirth, *Journal of Physical Chemistry C*, 2014, **118**, 27623-27630.
28. Y. Gofer, O. Chusid, H. Gizbar, Y. Viestfrid, H. E. Gottlieb, V. Marks and D. Aurbach, *Electrochemical and Solid State Letters*, 2006, **9**, A257-A260.
29. J. Muldoon, C. B. Bucur, A. G. Oliver, J. Zajicek, G. D. Allred and W. C. Boggess, *Energy & Environmental Science*, 2013, **6**, 482-487.
30. J. Shen, B. Peng, Z. Tao and J. Chen, *Progress in Chemistry*, 2010, **22**, 515-521.
31. E. Levi, Y. Gofer and D. Aurbach, *Chemistry of Materials*, 2010, **22**, 860-868.
32. D. Aurbach, G. S. Suresh, E. Levi, A. Mitelman, O. Mizrahi, O. Chusid and M. Brunelli, *Advanced Materials*, 2007, **19**, 4260-+.
33. E. Levi, M. D. Levi, O. Chasid and D. Aurbach, *Journal of Electroceramics*, 2009, **22**, 13-19.
34. E. Levi, Y. Gofer, Y. Vestfreed, E. Lancry and D. Aurbach, *Chemistry of Materials*, 2002, **14**, 2767-2773.
35. E. Lancry, E. Levi, Y. Gofer, M. Levi, G. Salitra and D. Aurbach, *Chemistry of Materials*, 2004, **16**, 2832-2838.
36. M. D. Levi, H. Gizbar, E. Lancry, Y. Gofer, E. Levi and D. Aurbach, *Journal of Electroanalytical Chemistry*, 2004, **569**, 211-223.
37. P. Novak and J. Desilvestro, *Journal of the Electrochemical Society*, 1993, **140**, 140-144.
38. J. O. Besenhard and M. Winter, *Chemphyschem*, 2002, **3**, 155-+.
39. O. Mizrahi, N. Amir, E. Pollak, O. Chusid, V. Marks, H. Gottlieb, L. Larush, E. Zinigrad and D. Aurbach, *Journal of the Electrochemical Society*, 2008, **155**, A103-A109.
40. N. Pour, Y. Gofer, D. T. Major and D. Aurbach, *Journal of the American Chemical Society*, 2011, **133**, 6270-6278.
41. R. Zhang, T. S. Arthur, C. Ling and F. Mizuno, *Journal of Power Sources*, 2015, **282**, 630-638.
42. H. S. Kim, T. S. Arthur, G. D. Allred, J. Zajicek, J. G. Newman, A. E. Rodnyansky, A. G. Oliver, W. C. Boggess and J. Muldoon, *Nature Communications*, 2011, **2**, 6.
43. C. Wall, Z. Zhao-Karger and M. Fichtner, *ECS Electrochemistry Letters*, 2015, **4**, C8-C10.
44. Z. Zhao-Karger, X. Zhao, D. Wang, T. Diemant, R. J. Behm and M. Fichtner, *Advanced Energy Materials*, 2015, **5**.
45. T. Gao, M. Noked, A. J. Pearse, E. Gillette, X. Fan, Y. Zhu, C. Luo, L. Suo, M. A. Schroeder, K. Xu, S. B. Lee, G. W. Rubloff and C. Wang, *Journal of*

the American Chemical Society, 2015.
46. Z. Zhao-Karger, X. Zhao, O. Fuhr and M. Fichtner, *Rsc Advances*, 2013, **3**, 16330-16335.
47. Y. Guo, F. Zhang, J. Yang and F. Wang, *Electrochemistry Communications*, 2012, **18**, 24-27.
48. Y.-s. Guo, F. Zhang, J. Yang, F.-f. Wang, Y. NuLi and S.-i. Hirano, *Energy & Environmental Science*, 2012, **5**, 9100-9106.
49. K. A. See, K. W. Chapman, L. Zhu, K. M. Wiaderek, O. J. Borkiewicz, C. J. Barile, P. J. Chupas and A. A. Gewirth, *Journal of the American Chemical Society*, 2016, **138**, 328-337.
50. R. E. Doe, R. Han, J. Hwang, A. J. Gmitter, I. Shterenberg, H. D. Yoo, N. Pour and D. Aurbach, *Chemical Communications*, 2014, **50**, 243-245.
51. T. Liu, Y. Shao, G. Li, M. Gu, J. Hu, S. Xu, Z. Nie, X. Chen, C. Wang and J. Liu, *Journal of Materials Chemistry A*, 2014, **2**, 3430-3438.
52. T. J. Carter, R. Mohtadi, T. S. Arthur, F. Mizuno, R. Zhang, S. Shirai and J. W. Kampf, *Angewandte Chemie-International Edition*, 2014, **53**, 3173-3177.
53. O. Tutusaus, R. Mohtadi, T. S. Arthur, F. Mizuno, E. G. Nelson and Y. V. Sevryugina, *Angewandte Chemie (International ed. in English)*, 2015, **54**, 7900-7904.
54. S.-Y. Ha, Y.-W. Lee, S. W. Woo, B. Koo, J.-S. Kim, J. Cho, K. T. Lee and N.-S. Choi, *Acs Applied Materials & Interfaces*, 2014, **6**, 4063-4073.
55. I. Shterenberg, M. Salama, H. D. Yoo, Y. Gofer, J.-B. Park, Y.-K. Sun and D. Aurbach, *Journal of the Electrochemical Society*, 2015, **162**, A7118-A7128.
56. A. L. M. Reddy, M. M. Shaijumon, S. R. Gowda and P. M. Ajayan, *Nano Letters*, 2009, **9**, 1002-1006.
57. R. Liu, J. Duay and S. B. Lee, *Acs Nano*, 2010, **4**, 4299-4307.
58. Y.-K. Hsu, Y.-C. Chen, Y.-G. Lin, L.-C. Chen and K.-H. Chen, *Chemical Communications*, 2011, **47**, 1252-1254.
59. J. Duay, S. A. Sherrill, Z. Gui, E. Gillette and S. B. Lee, *Acs Nano*, 2013, **7**, 1200-1214.
60. D. Liu and G. Cao, *Energy & Environmental Science*, 2010, **3**, 1218-1237.
61. A. Manthiram, A. V. Murugan, A. Sarkar and T. Muraliganth, *Energy & Environmental Science*, 2008, **1**, 621-638.
62. A. S. Arico, P. Bruce, B. Scrosati, J. M. Tarascon and W. Van Schalkwijk, *Nature Materials*, 2005, **4**, 366-377.
63. G. Wang, L. Zhang and J. Zhang, *Chemical Society Reviews*, 2012, **41**, 797-828.
64. R. Liu, J. Duay and S. B. Lee, *Chemical Communications*, 2011, **47**, 1384-1404.
65. F. Y. Cheng, J. Z. Zhao, W. Song, C. S. Li, H. Ma, J. Chen and P. W. Shen, *Inorganic Chemistry*, 2006, **45**, 2038-2044.
66. D. Su, H.-J. Ahn and G. Wang, *Journal of Materials Chemistry A*, 2013, **1**, 4845-4850.
67. X. Wang and Y. D. Li, *Journal of the American Chemical Society*, 2002, **124**, 2880-2881.
68. S. Bach, M. Henry, N. Baffier and J. Livage, *Journal of Solid State Chemistry*,

1990, **88**, 325-333.
69. J. W. Long, R. M. Stroud and D. R. Rolison, *Journal of Non-Crystalline Solids*, 2001, **285**, 288-294.
70. S. Franger, S. Bach, J. Farcy, J. P. Pereira-Ramos and N. Baffier, *Journal of Power Sources*, 2002, **109**, 262-275.
71. H. Y. Lee and J. B. Goodenough, *Journal of Solid State Chemistry*, 1999, **144**, 220-223.
72. S. Chen, J. Zhu, Q. Han, Z. Zheng, Y. Yang and X. Wang, *Crystal Growth & Design*, 2009, **9**, 4356-4361.
73. D. Portehault, S. Cassaignon, E. Baudrin and J.-P. Jolivet, *Chemistry of Materials*, 2007, **19**, 5410-5417.
74. S. C. Pang, M. A. Anderson and T. W. Chapman, *Journal of the Electrochemical Society*, 2000, **147**, 444-450.
75. X. Y. Wang, W. G. Huang, P. J. Sebastian and S. Gamboa, *Journal of Power Sources*, 2005, **140**, 211-215.
76. K. W. Nam and K. B. Kim, *Journal of the Electrochemical Society*, 2006, **153**, A81-A88.
77. M. Paunovic and M. Schlesinger, *Fundamentals of Electrochemical Deposition*, 2006.
78. H. Gao, F. Xiao, C. B. Ching and H. Duan, *ACS Applied Materials & Interfaces*, 2012, **4**, 2801-2810.
79. I. Zhitomirsky, M. Cheong and J. Wei, *Jom*, 2007, **59**, 66-69.
80. D. Liu, Q. Zhang, P. Xiao, B. B. Garcia, Q. Guo, R. Champion and G. Cao, *Chemistry of Materials*, 2008, **20**, 1376-1380.
81. W. Wei, X. Cui, W. Chen and D. G. Ivey, *Journal of Physical Chemistry C*, 2008, **112**, 15075-15083.
82. C. C. Hu and C. C. Wang, *Journal of the Electrochemical Society*, 2003, **150**, A1079-A1084.
83. D. Tench and L. F. Warren, *Journal of the Electrochemical Society*, 1983, **130**, 869-872.
84. W. Yan, T. Ayvazian, J. Kim, Y. Liu, K. C. Donavan, W. Xing, Y. Yang, J. C. Hemminger and R. M. Penner, *ACS Nano*, 2011, **5**, 8275-8287.
85. W. Yan, J. Y. Kim, W. Xing, K. C. Donavan, T. Ayvazian and R. M. Penner, *Chemistry of Materials*, 2012, **24**, 2382-2390.
86. J. W. Long, B. Dunn, D. R. Rolison and H. S. White, *Chemical Reviews*, 2004, **104**, 4463-4492.
87. G. E. J. Poinern, N. Ali and D. Fawcett, *Materials*, 2011, **4**, 487-526.
88. A. M. M. Jani, D. Losic and N. H. Voelcker, *Progress in Materials Science*, 2013, **58**, 636-704.
89. H. Masuda and M. Satoh, *Japanese Journal of Applied Physics Part 2-Letters*, 1996, **35**, L126-L129.
90. S. A. Sherrill, J. Duay, Z. Gui, P. Banerjee, G. W. Rubloff and S. B. Lee, *Physical Chemistry Chemical Physics*, 2011, **13**, 15221-15226.
91. C. Liu, E. I. Gillette, X. Chen, A. J. Pearse, A. C. Kozen, M. A. Schroeder, K. E. Gregorczyk, S. B. Lee and G. W. Rubloff, *Nature Nanotechnology*, 2014, **9**, 1031-1039.

92. C. Mu, Y. X. Yu, W. Liao, X. S. Zhao, D. S. Xu, X. H. Chen and D. P. Yu, *Applied Physics Letters*, 2005, **87**.
93. D. Routkevitch, A. A. Tager, J. Haruyama, D. Almawlawi, M. Moskovits and J. M. Xu, *Ieee Transactions on Electron Devices*, 1996, **43**, 1646-1658.
94. J. B. Yi, H. Pan, J. Y. Lin, J. Ding, Y. P. Feng, S. Thongmee, T. Liu, H. Gong and L. Wang, *Advanced Materials*, 2008, **20**, 1170-+.
95. L. Taberna, S. Mitra, P. Poizot, P. Simon and J. M. Tarascon, *Nature Materials*, 2006, **5**, 567-573.
96. D. B. Williams and C. B. Carter, in *Transmission Electron Microscopy: A Textbook for Materials Science*, eds. D. B. Williams and C. B. Carter, Springer US, Boston, MA, 1996, pp. 3-17.
97. D. A. Skoog, F. J. Holler and S. R. Crouch, *Principles of instrumental analysis*, Brooks/Cole :, Australia :, 6th ed. edn., 2007.
98. N. Fairley and L. Casa Software, *CasaXPS manual 2.3.15 : spectroscopy*, Casa Software Ltd., Great Britain :, Rev. 1.2 ed.. edn., 2009.
99. M. C. Biesinger, B. P. Payne, A. P. Grosvenor, L. W. M. Lau, A. R. Gerson and R. S. C. Smart, *Applied Surface Science*, 2011, **257**, 2717-2730.
100. D. Briggs and G. Beamson, *Analytical Chemistry*, 1993, **65**, 1517-1523.
101. C. Julien, M. Massot, R. Baddour-Hadjean, S. Franger, S. Bach and J. P. Pereira-Ramos, *Solid State Ionics*, 2003, **159**, 345-356.
102. J. Duay, Doctoral Thesis, University of Maryland, 2013.
103. M. M. Thackeray, *Progress in Solid State Chemistry*, 1997, **25**, 1-71.
104. D. Wang, L.-M. Liu, S.-J. Zhao, B.-H. Li, H. Liu and X.-F. Lang, *Physical Chemistry Chemical Physics*, 2013, **15**, 9075-9083.
105. B. Ammundsen and J. Paulsen, *Advanced Materials*, 2001, **13**, 943-+.
106. M. M. Thackeray, C. S. Johnson, J. T. Vaughey, N. Li and S. A. Hackney, *Journal of Materials Chemistry*, 2005, **15**, 2257-2267.
107. W. Wei, X. Cui, W. Chen and D. G. Ivey, *Chemical Society Reviews*, 2011, **40**, 1697-1721.
108. Q. Feng, H. Kanoh and K. Ooi, *Journal of Materials Chemistry*, 1999, **9**, 319-333.
109. T. Brousse, M. Toupin, R. Dugas, L. Athouel, O. Crosnier and D. Belanger, *Journal of the Electrochemical Society*, 2006, **153**, A2171-A2180.
110. S. Devaraj and N. Munichandraiah, *Journal of Physical Chemistry C*, 2008, **112**, 4406-4417.
111. J. J. Xu, A. J. Kinser, B. B. Owens and W. H. Smyrl, *Electrochemical and Solid State Letters*, 1998, **1**, 1-3.
112. W. C. West, N. V. Myung, J. F. Whitacre and B. V. Ratnakumar, *Journal of Power Sources*, 2004, **126**, 203-206.
113. M. Toupin, T. Brousse and D. Belanger, *Chemistry of Materials*, 2004, **16**, 3184-3190.
114. C. Xu, C. Wei, B. Li, F. Kang and Z. Guan, *Journal of Power Sources*, 2011, **196**, 7854-7859.
115. S.-L. Kuo and N.-L. Wu, *Journal of the Electrochemical Society*, 2006, **153**, A1317-A1324.
116. E. Wernersson, R. Kjellander and J. Lyklema, *Journal of Physical Chemistry*

C, 2010, **114**, 1849-1866.
117. Z. L. Tao, L. N. Xu, X. L. Gou, J. Chen and H. T. Yuan, *Chemical Communications*, 2004, 2080-2081.
118. Y. N. Nuli, J. Yang, Y. P. Zheng and J. L. Wang, *Journal of Inorganic Materials*, 2011, **26**, 129-133.
119. B. Liu, T. Luo, G. Y. Mu, X. F. Wang, D. Chen and G. Z. Shen, *Acs Nano*, 2013, **7**, 8051-8058.
120. P. Novak, W. Scheifele, F. Joho and O. Haas, *Journal of the Electrochemical Society*, 1995, **142**, 2544-2550.
121. A. Ryu, M. S. Park, W. Cho, J. S. Kim and Y. J. Kim, *Bulletin of the Korean Chemical Society*, 2013, **34**, 3033-3038.
122. A. Mitelman, M. D. Levi, E. Lancry, E. Levi and D. Aurbach, *Chemical Communications*, 2007, 4212-4214.
123. E. Levi, G. Gershinsky, D. Aurbach and O. Isnard, *Inorganic Chemistry*, 2009, **48**, 8751-8758.
124. L. Yu and X. G. Zhang, *Journal of Colloid and Interface Science*, 2004, **278**, 160-165.
125. Z. G. Wang, Q. L. Su and H. Q. Deng, *Physical Chemistry Chemical Physics*, 2013, **15**, 8705-8709.
126. P. E. Tang, J. S. Sakamoto, E. Baudrin and B. Dunn, *Journal of Non-Crystalline Solids*, 2004, **350**, 67-72.
127. G. Gershinsky, H. D. Yoo, Y. Gofer and D. Aurbach, *Langmuir*, 2013, **29**, 10964-10972.
128. R. G. Zhang, X. Q. Yu, K. W. Nam, C. Ling, T. S. Arthur, W. Song, A. M. Knapp, S. N. Ehrlich, X. Q. Yang and M. Matsui, *Electrochemistry Communications*, 2012, **23**, 110-113.
129. C. Yuan, Y. Zhang, Y. Pan, X. Liu, G. Wang and D. Cao, *Electrochimica Acta*, 2014, **116**, 404-412.
130. S. Rasul, S. Suzuki, S. Yamaguchi and M. Miyayama, *Electrochimica Acta*, 2013, **110**, 247-252.
131. S. Rasul, S. Suzuki, S. Yamaguchi and M. Miyayama, *Solid State Ionics*, 2012, **225**, 542-546.
132. S. Rasul, S. Suzuki, S. Yamaguchi and M. Miyayama, *Electrochimica Acta*, 2012, **82**, 243-249.
133. N. Kumagai, S. Komaba and H. Sakai, *Journal of Power Sources*, 2001, **97-8**, 515-517.
134. D. Sharon, M. Afri, M. Noked, A. Garsuch, A. A. Frimer and D. Aurbach, *Journal of Physical Chemistry Letters*, 2013, **4**, 3115-3119.
135. J. Song, J. Duay, E. Gillette and S. B. Lee, *Chemical Communications*, 2014, **50**, 7352-7355.
136. W. R. Fawcett and G. J. Liu, *Journal of Physical Chemistry*, 1992, **96**, 4231-4236.
137. P. He, X. Zhang, Y.-G. Wang, L. Cheng and Y.-Y. Xia, *Journal of the Electrochemical Society*, 2008, **155**, A144-A150.
138. C. J. Patrissi and C. R. Martin, *Journal of the Electrochemical Society*, 2001, **148**, A1247-A1253.

139. M. Rodahl and B. Kasemo, *Sensors and Actuators a-Physical*, 1996, **54**, 448-456.
140. K. W. Nam, S. Kim, S. Lee, M. Salama, I. Shterenberg, Y. Gofer, J.-S. Kim, E. Yang, C. S. Park, J.-S. Kim, S.-S. Lee, W.-S. Chang, S.-G. Doo, Y. N. Jo, Y. Jung, D. Aurbach and J. W. Choi, *Nano Letters*, 2015, **15**, 4071-4079.
141. X. Sun, V. Duffort, B. L. Mehdi, N. D. Browning and L. F. Nazar, *Chemistry of Materials*, 2015.
142. T. Arthur, R. Zhang, C. Ling, P.-A. Glans, X. Fan, J. Guo and F. Mizuno, *ACS Applied Materials & Interfaces*, 2014.
143. C. Ling, R. Zhang, T. S. Arthur and F. Mizuno, *Chemistry of Materials*, 2015, **27**, 5799-5807.
144. Y.-T. Weng, H.-A. Pan, R.-C. Lee, T.-Y. Huang, Y. Chu, J.-F. Lee, H.-S. Sheu and N.-L. Wu, *Advanced Energy Materials*, 2015, **5**.
145. M. C. Militello and S. W. Gaarenstroom, *Surface Science Spectra*, 2001, **8**, 207-213.
146. M. C. Militello and S. W. Gaarenstroom, *Surface Science Spectra*, 2001, **8**, 200-206.
147. A. A. Audi and P. M. A. Sherwood, *Surface and Interface Analysis*, 2002, **33**, 274-282.
148. J. M. Cerrato, M. F. Hochella, Jr., W. R. Knocke, A. M. Dietrich and T. F. Cromer, *Environmental Science & Technology*, 2010, **44**, 5881-5886.
149. M. Hu, X. Pang and Z. Zhou, *Journal of Power Sources*, 2013, **237**, 229-242.
150. Z. Chen, S. Qiu, Y. Cao, X. Ai, K. Xie, X. Hong and H. Yang, *Journal of Materials Chemistry*, 2012, **22**, 17768-17772.
151. X. Zhang, F. Cheng, J. Yang and J. Chen, *Nano Letters*, 2013, **13**, 2822-2825.
152. R. Santhanam and B. Rambabu, *Journal of Power Sources*, 2010, **195**, 5442-5451.
153. J. Liu and A. Manthiram, *Chemistry of Materials*, 2009, **21**, 1695-1707.
154. K. Xu and A. von Cresce, *Journal of Materials Chemistry*, 2011, **21**, 9849-9864.
155. Y. K. Sun, K. J. Hong, J. Prakash and K. Amine, *Electrochemistry Communications*, 2002, **4**, 344-348.
156. S. Verdier, L. El Ouatani, R. Dedryvere, F. Bonhomme, P. Biensan and D. Gonbeau, *Journal of the Electrochemical Society*, 2007, **154**, A1088-A1099.
157. L. Baggetto, N. J. Dudney and G. M. Veith, *Electrochimica Acta*, 2013, **90**, 135-147.
158. Y. K. Sun, Y. S. Lee, M. Yoshio and K. Amine, *Journal of the Electrochemical Society*, 2003, **150**, L11-L11.
159. S. Oh, J. K. Lee, D. Byun, W. I. Cho and B. W. Cho, *Journal of Power Sources*, 2004, **132**, 249-255.
160. I. D. Scott, Y. S. Jung, A. S. Cavanagh, Y. An, A. C. Dillon, S. M. George and S.-H. Lee, *Nano Letters*, 2011, **11**, 414-418.
161. Y. S. Jung, A. S. Cavanagh, L. A. Riley, S.-H. Kang, A. C. Dillon, M. D. Groner, S. M. George and S.-H. Lee, *Advanced Materials*, 2010, **22**, 2172-+.
162. X. Han, Y. Liu, Z. Jia, Y.-C. Chen, J. Wan, N. Weadock, K. J. Gaskell, T. Li and L. Hu, *Nano Letters*, 2014, **14**, 139-147.

163. J. Zhao and Y. Wang, *Journal of Physical Chemistry C*, 2012, **116**, 11867-11876.
164. Y. S. Jung, A. S. Cavanagh, Y. Yan, S. M. George and A. Manthiram, *Journal of the Electrochemical Society*, 2011, **158**, A1298-A1302.
165. X. Fang, M. Ge, J. Rong, Y. Che, N. Aroonyadet, X. Wang, Y. Liu, A. Zhang and C. Zhou, *Energy Technology*, 2014, **2**, 159-165.
166. B. J. Hwang, Y. W. Wu, M. Venkateswarlu, M. Y. Cheng and R. Santhanam, *Journal of Power Sources*, 2009, **193**, 828-833.
167. M. Bettge, Y. Li, B. Sankaran, N. D. Rago, T. Spila, R. T. Haasch, I. Petrov and D. P. Abraham, *Journal of Power Sources*, 2013, **233**, 346-357.